Engineering Ultrasound Contrast Agents for Increased Stability and Nonlinearity

by

Mehrdad Azmin

A dissertation submitted for the degree of

Doctor of Philosophy

at

University College London

2016

Department of Mechanical Engineering

University College London

Torrington Place

London WC1E 7JE

Declaration

I, Mehrdad Azmin, confirm that the work presented in this thesis is my own. Where information has been derived from other sources, I confirm that this has been indicated in the thesis.

.....……

.....……

Abstract

There has been increasing interest in the use of microbubbles as contrast agents in various diagnostic and therapeutic applications of biomedical ultrasound. New techniques have been developed which rely upon nonlinear scattering of acoustic waves by contrast agents undergoing volumetric oscillations upon exposure to ultrasound. The degree of nonlinearity can be improved by increasing the amplitude of the insonation pressure. This may, however, increase the risk of destroying the contrast agent and produce undesirable side effects either through inducing shear stress around them, or by undergoing inertial cavitation. The latter phenomenon is associated with high temperature and extreme pressures and can potentially damage the tissue surrounding the bubble. A further problem is the change in contrast agent size due to dissolution which is an important factor in determining their response to ultrasound.

A proposed solution to these issues is to deposit solid nanoparticles on the outer surface of the microbubbles to form a semi-solid shell upon reaching a certain surface density. As the bubbles undergo volumetric oscillations, the particles offer resistance when bubbles contract but not during expansion. The asymmetry of oscillations is thus increased and the nonlinear character of the acoustic response is improved. In addition, the particles stabilize the microbubbles by inhibiting the transfer of gas to surrounding liquid as well as resisting the capillary pressure due to interfacial tension.

This thesis commences with a review of the current literature followed by a review of theoretical models for the dynamics and dissolution of free and coated microbubbles. A new dissolution model accounting for the effect of nanoparticles and a surfactant coating is then proposed and simulations compared with experimental results obtained from collaborators. A current dynamic model describing a coated microbubble is evaluated. This is then expanded to provide a new dynamic model for a contrast agent with a finite thickness shell with variable surface tension and viscosity. Finally the microfluidic method for producing contrast agents is studied through a computational fluid dynamic model followed by recommendations for future directions of study.

Acknowledgements

I am immensely thankful to Prof. Eleanor Stride for her advice, encouragement, and support throughout my PhD. This work would not be possible without her and I shall forever remain in her debt. I am also thankful Prof. Mohan Edirisinghe first for suggesting me for this project and later for ensuring the smooth running of it throughout its duration. I would like to thank EPSRC for their funding of this PhD.

This project was mainly conducted on paper and computer screen. I am therefore much obliged to my friends and collaborators who have provided me with their experimental data and have always been generous with their time in answering my questions. My thanks go to Graciela Mohamedi for the stability studies; Paul Rademeyer who investigated the bubble responses; and Maryam Parhizkar for the microfluidic studies.

I am also grateful to Reza Haqshenas and Ki Joo Pahk who unquestioningly surrendered their computers when I needed extra processing power. I am further thankful to Reza for the very many useful conversations and his immense generosity with his time. I hope that one day I will be able to reciprocate. I am indebted to Caroline Harfield and Joshua Owen for their friendship, support, and lending their living room in Oxford in the final weeks of writing this thesis.

I am grateful to Ms. Golkou Parhizgar for her patience, love, and encouragement throughout this process. I would finally like to thank my parents, Mitra and Behzad, whose support and encouragement, despite the three thousand miles between us, have helped me in every step of the way.

Contents

List of Figures

List of Tables

Nomenclature

$a_{1\text{and }2}$	surfactant specific constants for diffusion
B	universal gas constant
Bo	Bond number
c	speed of sound
C	concentration of gas dissolved in the liquid
Ca	capillary number
C_B	circumference of bubble at packing
C_i	initial concentration of gas in liquid
C_{sat}	saturation concentration of gas in liquid
D	coefficient of diffusion
D_0	initial coefficient of diffusion
d_{s0}	initial coating thickness
f	insonation frequency
$\mathbf{f}$	stress tensor
f_I	inertial function
f_p	pressure function
f_{peak}	peak frequency
f_{res}	resonance frequency
G_s	shear modulus of coating
H	enthalpy
I_{inc}	intensity of incident field
J	mass flux
K	surfactant dependant surface tension parameter
L	distance between particles and bubble centre
m	mass
M	molecular weight
n	number of moles
n_p	number of nanoparticles
p_0	hydrostatic pressure
p_∞	pressure at large distance from the bubble
p_A	peak acoustic pressure

p_g	gas pressure inside the bubble
p_l	liquid pressure
$p_{Laplace}$	Laplace's pressure
p_{rad}	radiated pressure
p_v	vapour pressure
R	instantaneous bubble radius
r	radial distance from the bubble centre
R_0	initial bubble radius
$R_{01 \text{ and } 02}$	initial inner and outer radii of the bubble
$R_{1 \text{ and } 2}$	instantaneous inner and outer radii of the bubble
r_c	radius of curvature
$\dot{R}$	bubble wall velocity
$\ddot{R}$	bubble wall acceleration
R_{e1}	equilibrium radius
R_p	bubble radius at packing
r_p	nanoparticle radius
R_x	radius of bubble at buckling
S_D	uncovered surface area available for diffusion
S_{ext}	extinction cross-section
S_f	shell friction parameter
S_p	shell elasticity parameter
S_{scat}	scattering cross-section
T	absolute temperature / time period
t	time
$\mathbf{T}$	deviatoric component of stress tensor
$\mathbf{u}$	velocity vector
U	flow velocity
W	2D distance between centres of particles at packing
We	Webber number
$w_{in \text{ and } out}$	channel widths for input and output conduits
x	
x_s	surfactant dependant surface tension parameter
Y	effective diffusion function

Z	surfactant dependant viscosity parameter
Γ	instantaneous surfactant concentration
Γ_0	initial surfactant concentration
Γ_{max}	maximum surfactant concentration
δ	effective minimum 2D distance between nanoparticle at packing
δ_{rad}	radiation damping coefficient
δ_t	total damping coefficient
δ_{th}	thermal damping coefficient
δ_{vis}	viscous damping coefficient
ε_{rr}	radial displacement from equilibrium
θ	angle between two adjacent particles
κ	polytropic constant
κ_s	dilatational viscosity
κ_{s0}	initial dilatational viscosity
Λ	channel width ratio
λ	ratio of viscosities
λ_s	Lamé constant
λ_w	wavelength
μ_0	initial shear viscosity of the particle free coating
μ_{eff}	effective shear viscosity
μ_l	liquid Viscosity
ρ_l	liquid density
ρ_g	gas density
ρ_s	shell density
σ	surface tension
σ_0	surface tension of the clean surface
Φ	volume fraction of the particles in the coating
ϕ	nanoparticle surface concentration
ϕ_c	nanoparticle circumferential concentration
χ	shell elasticity
ω	angular frequency

1. Introduction

1.1. Overview

Ultrasonic imaging possesses several advantages over other modalities such as X-ray Computed Tomography (CT) or Magnetic Resonance Imaging (MRI). Ultrasound is a real-time modality that commonly allows imaging up to 30 frames per second. Since it does not use any form of ionizing radiation, it is much safer than many other imaging methods particularly CT and nuclear imaging techniques. It is less expensive both in terms of equipment and scanning costs and scanners are easily installed in hospitals, clinics and General Practice surgeries. Portability is another factor in favour of ultrasonic imaging devices. They range from larger units that can be wheeled to patients' bedside to handheld devices that have recently been introduced to the market [1].

Ultrasound imaging is based on reflection and/or scattering of the propagating wave from interfaces/structures with different acoustic properties. The frequency of this mechanical wave is higher than 20kHz which corresponds to the upper limit of human hearing. When an ultrasound wave reaches an interface where there is an acoustic impedance mismatch (i.e. the product of the materials' densities and speed of sound is different) some of it will be reflected. The larger the difference in impedance the greater the amount of energy reflected/scattered from the interface. By measuring the time it has taken for a transmitted signal to return to the ultrasound transducer, and knowing the speed of sound in the medium in which it has travelled, the position of the interface can be determined and displayed accordingly on the imaging device. Ultrasound is widely used for imaging soft tissue (e.g. in cardiac or abdominal scanning) but certain features, in particular small blood vessels, present a significant challenge. Blood cells are relatively poor scatterers of ultrasound and hence the contrast to noise ratio is often low. Ultrasonic Contrast Agents are used to overcome these problems.

Ultrasonic Contrast Agents (UCAs) are bubbles with diameters ranging between 1 and 10μm, and consisting of a gas encapsulated in a lipid/surfactant or polymeric

shell. Their interactions with ultrasound are of great interest in a variety of applications within medical diagnostic imaging and therapy.

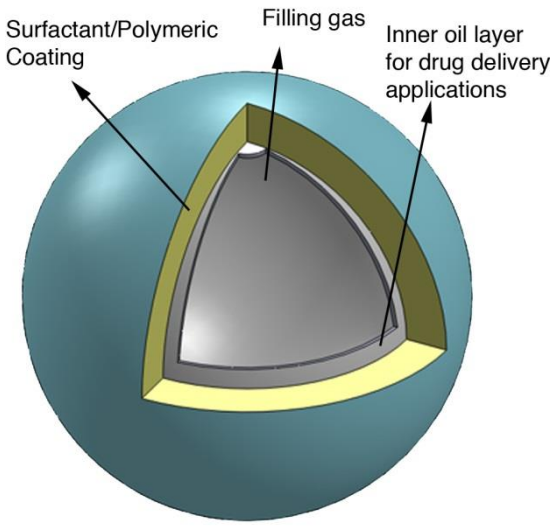

Figure 1.1 - Schematic of a coated microbubble including an inner oil layer for drug delivery applications.

The high echogenicity of UCAs is due to them being filled with gas. This produces a large difference in acoustic impedance between them and their surroundings *in vivo* which have similar densities. More importantly it makes them highly compressible so that they undergo volumetric oscillations in response to ultrasound excitation. For bubbles of a few micrometres in diameter, the resonance frequency is in the order of MHz, which conveniently lies within the frequency range of modern medical ultrasonic imaging apparatus. As a result of these oscillations, the bubbles act as an "acoustic monopole", emitting a secondary sound wave. Thus the reflections will contain contributions from both microbubbles and their surrounding tissue. The signal reflected from tissue is in most part linear, whereas those emitted by the microbubbles, due to their nonlinear response, tend to contain both the excitation frequency and its harmonics. The signal from microbubbles can therefore be distinguished by separating the harmonic content from the signal. The simplest method of achieving this would be to employ a filter and remove the principal frequency. There are, however, some drawbacks to this method. In order to achieve good separation, the bandwidth of the fundamental frequency must not overlap with that of the second harmonic. Consequently a narrower transmit bandwidth has to be used which limits the image resolution. In addition, it has been observed that above certain acoustic pressures, the tissue exhibits noticeable nonlinear response [2] which

interferes with signal from microbubbles and therefore perfect separation cannot be achieved. A number of imaging techniques, such as pulse inversion [3,4] and power modulation [5], have been developed to overcome this issue. In pulse inversion imaging, two identical but out of phase pulses are transmitted one after each other with a suitable delay between them. Linear reflectors respond equally to positive and negative pressures and will reflect equal but out of phase signals. Addition of these two echoes will therefore be zero. Microbubbles, however, respond differently to positive and negative pressures and the summation of their echoes do not cancel out completely. A graphical illustration of this technique along with an example of an image of a liver lesion using this method is given in Figure 1.2. Pulse inversion imaging allows for wider bandwidth incident signal to be transmitted, thereby increasing the resolution of the image.

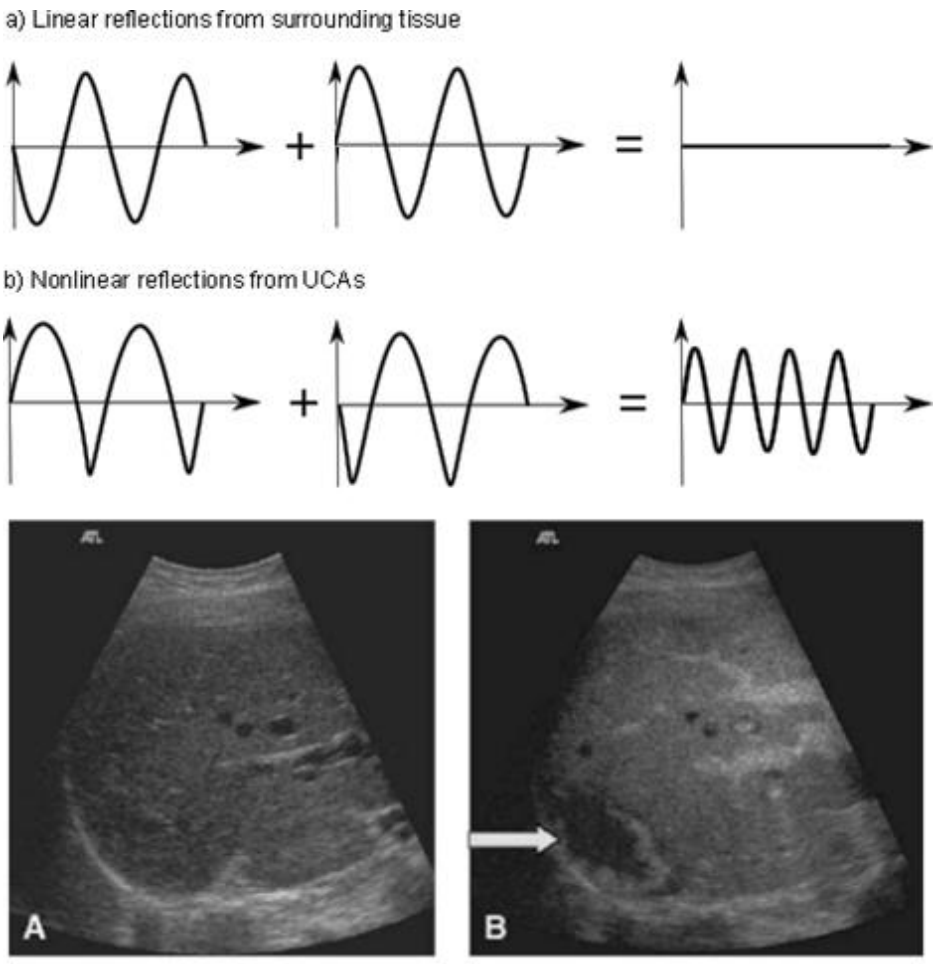

Figure 1.2 – Top: a) Summation of reflections from consecutive, out of phase transmitted pulses. Tissue responds linearly to both and therefore summation results in them cancelling out. b) Microbubble responds differently to the inverted transmitted pulses. A residual is left after their summation; Bottom: Comparison of an ultrasound image of a hemangioma using: A) Conventional ultrasound imaging. B) Pulse inversion imaging [6]. The visibility of the lesion, indicated with the arrow, is improved.

Another technique exploiting the nonlinear echoes from microbubbles is Power Modulation Imaging in which the two consecutive, identical pulses with different intensities are transmitted in the same direction. After applying a correction factor to the echo from the first transmitted pulse to normalise it with respect to that from the second one, the signals are subtracted from one another. Once again, the signal from the linear echoes from the tissue cancels out after the application of correction factor. The nonlinear response of the microbubbles to the two pulses will differ in shape and therefore will not cancel out completely after subtraction.

1.2. Motivation

The nonlinear response of microbubbles in general increases with elevation of excitation pressure. The rise in acoustic pressure, however, can shorten the life of UCAs by irreversibly altering their composition and/or destroying them. It can, furthermore, bring about adverse effects in the tissue. In the absence of contrast agents, exposure to high intensity ultrasound may produce high temperatures damaging to sensitive organs [7]. Tissue damage can also be inflicted through mechanical effects where gas bubbles, including gas filled contrast agents, are present in the field. The damage can come from the shear stress induced around a bubble whilst in oscillation or by producing extreme pressure and temperatures due to inertial cavitation [8].

Microbubbles are constantly subject to mechanisms that promote instability. Changes in their radius may happen during insonation through rectified diffusion [9], variation of the core temperature, and alteration in shell composition. In addition, a microbubble is constantly being squeezed by the surface tension acting on its gas-liquid interface. This causes the gas to diffuse from microbubble core into the surrounding liquid whilst at rest [10]. Such alteration to physical characteristics of a microbubble changes its response to a given sound field which may cause a reduction in its efficacy and consequently require further administration of UCA to maintain enhancement. Microbubble stability becomes more vital in applications such as imaging low blood flow areas, where it might take up to several minutes for contrast to build up [6], or targeted imaging, where only a small portion of contrast agents are retained at the site of interest [11].

It is therefore highly desirable to design a UCA which exhibits highly nonlinear response to a low amplitude sound wave while maintaining a high degree of stability whether in oscillation or at rest. This also allows for same degree of contrast enhancement at a lower dosage, improving overall safety of UCAs. Eliciting the optimum performance from a contrast agent requires a theoretical understanding of its behaviour. This requires an ideal UCA to exhibit consistent and repeatable response. Developing controllable means of fabrication is therefore another essential step towards engineering UCAs. These are the areas addressed in this thesis.

1.3. Objectives

It has been demonstrated that embedding nanoparticles in the microbubble coating can greatly enhance their nonlinearity and stability [12,13]. New fabrication methods have also been investigated to produce highly monodispersed populations of these UCAs. The main aim of this thesis is to investigate each of these areas through the development of appropriate theoretical models. The specific objectives are:

- To derive new theoretical models describing the effect of nanoparticles upon the dynamic behaviour of a surfactant coated microbubble under ultrasound excitation.
- To formulate a model describing the dissolution of a nanoparticle coated microbubble.
- To investigate the microfluidic method of producing microbubbles using computational fluid dynamics modelling.
- To compare the results with experiments, make recommendations for further development and identify areas for future research.

1.4. Outline

The aims set out in the previous section are to be implemented in the next five chapters. Chapter 2 begins with an overview of contrast agents, their application, and principles, followed by a comprehensive presentation of available models describing their dynamic behaviour and stability. It provides an overview of the research and available mathematical models developed hitherto which are expanded upon in the latter chapters.

Chapter 3 is focused on accounting for the effect of a nanoparticle coating on the dynamic behaviour of microbubbles. To begin with, the basis of dynamic models for a thick-shelled and monolayer coated microbubble and the assumptions on which they rely on are presented. This is then followed by the introduction of the effect of nanoparticles on the shell behaviour and the dynamic equations are modified to reflect this. The modifications are tested using numerical simulations and their results are finally analysed.

The static stability of the nanoparticle coated microbubbles is investigated in Chapter 4, where a new diffusion model is derived using an existing approach with modifications to include the effect of nanoparticles. The results are then compared those in the experiments and their validity is discussed.

Chapter 5 begins with a brief overview of microfluidic method of microbubble production. The feasibility of this technique for fabrication of UCAs is then investigated using computer simulations. Included in the list of considered options is the analysis of a novel, low cost, microfluidic device which employs capillary tubing as opposed to etching processes to create micro channels. Simulation results are then analysed and recommendations are given.

The investigation in the previous chapter will inevitably lead to questions which warrant further consideration. These research avenues and final conclusions of the work done will be presented in Chapter 6.

2. Background

2.1. Overview

This chapter provides an overview of the applications and theoretical characterisation of microbubble contrast agents. A brief section on the clinical use of microbubbles and the different types available is presented first; followed by an overview of the methods used in production of microbubbles. A review of the theoretical models available describing the oscillations of both free and coated microbubbles is then made. Finally, the mechanisms affecting the stability of a microbubble and how these are described theoretically are considered.

Some of the models described in this section will later be used to form the basis of the theoretical approach used in this thesis. These will therefore be discussed in further detail in relevant chapters.

2.2. Ultrasound for Biomedical Applications

2.2.1. Basic Definition

Ultrasound is a propagating mechanical wave whose frequency is higher than 20 kHz. In solid materials, ultrasound may propagate as both longitudinal and transverse waves but in fluids and hence in the majority of soft tissues, propagation is primarily longitudinal. The simplest mathematical description of ultrasound is a pure sine wave characterised by a single frequency, f, and hence a single period, T, in the time domain, corresponding to a single wavelength, λ_w, in space. Figure 2.1 depicts a snapshot of an example of such a wave in time domain. T, f and λ_w, are related through the wave velocity $c = \lambda_w \times f = \lambda_w / T$.

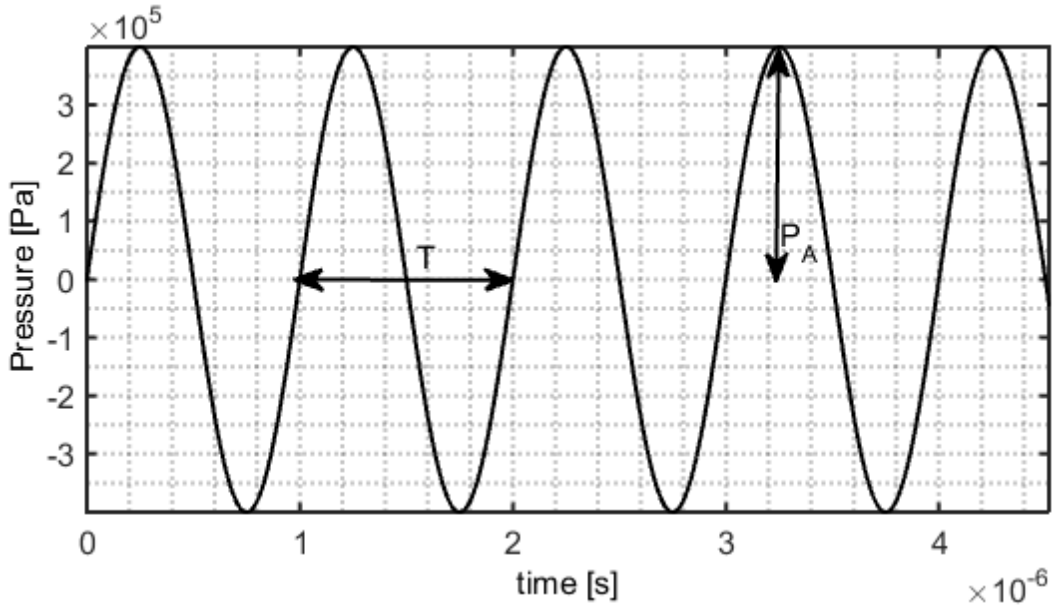

Figure 2.1 An example of a 5 Cycle, 1.0 MHz sinusoidal wave with peak amplitude of 400kPa. The time period and amplitude are denoted respectively by symbols T and P_A.

The wave amplitude is typically expressed in terms of pressure, p_A, although it can be equivalently represented in terms of particle displacement, velocity or acceleration. The equation describing an idealised plane wave propagating linearly in space, x, and time, t, can thus be written as

$$p(x,t) = p_a e^{i2\pi(ft - x/\lambda)} e^{-\alpha x}, \tag{2.1}$$

where p_a is the wave pressure amplitude and the last term, $e^{-\alpha x}$, describes the attenuation of the wave as it propagates due to viscous absorption and scattering. These effects are characterised by the attenuation coefficient, α.

In most practical applications, ultrasound is generated as a series of pulses rather than a continuous wave (Figure 2.2). A pulse consists of a number of cycles at a given frequency, known as the pulse centre frequency. Due to its finite length, however, the pulse will contain a range of other frequencies corresponding to a finite bandwidth in the frequency domain.

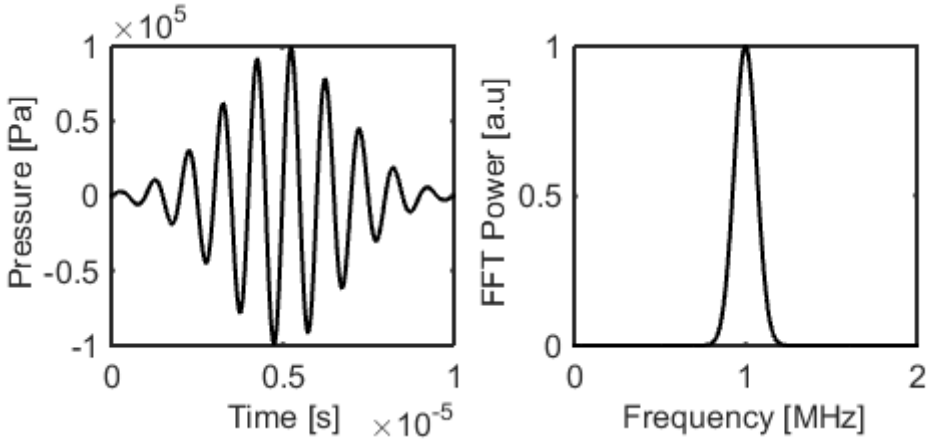

Figure 2.2 An example of a 10 Cycle, 1.0 MHz Gaussian windowed pulse (Right) and its frequency content (Left).

The bandwidth is normally measured as the range of frequencies for which the pulse amplitude or power is greater than half its maximum value. The shorter the pulse the wider the range of frequencies it contains. In biomedical ultrasound pulse lengths may vary from 2-3 cycles for diagnostic imaging to several thousand or more cycles in therapeutic applications. The rate at which pulses are generated is known as the pulse repetition frequency (PRF) and the length of the pulse, t_p, relative to the interval between pulses (1/PRF) is known as the duty cycle. Similarly, the amplitude of the pulse will vary over its length and is therefore normally quoted in terms of the peak negative or peak positive pressure.

2.2.2. Diagnostic Ultrasound Imaging

Microbubble contrast agents are employed in a range of diagnostic applications. Their most frequent use is in cardiology for improving visualisation of cardiac structures [14,15]. Other cardiovascular applications include detection and assessment of atherosclerosis [16] and stroke [17]. They are also becoming widely used in the characterisation of tumour vascularity [18] with nonlinear imaging techniques enabling mapping of the microcirculation with excellent spatial resolution including in 3D. Administration of microbubbles is normally intravenous but contrast agents are increasingly being used for non-vascular applications such as

assessment of fallopian tube patency [19] and detection of ureteric reflux [20]. Regulatory bodies such as the European Federation of Societies for Ultrasound in Medicine and Biology (EFSUMB) regularly publish best practice guidelines for use of medical ultrasound in which the main clinical areas where contrast agents are effective are highlighted [21].

2.2.3. Quantitative Imaging

Ultrasound Doppler studies have long been used for quantifying blood flow velocity and microbubbles can also be used to amplify the Doppler signal [22]. Their highly non-linear response can, however, affect measurement accuracy and this has limited their application; although new signal processing techniques have recently been developed which may revive interest in this area [23]. It is frequently desirable to evaluate other quantities such as relative vascular volume, flow velocity and perfusion rate and microbubbles have shown considerable potential in this regard [24-27]. All of these methods rely on the analysis of changes in image intensity which is related to microbubble concentration. Reliable quantitative imaging protocols, however, require the relationship between microbubble concentration and the ultrasound signal to be fully characterised and the complexity of this relationship currently poses a significant barrier to the development of clinically useful techniques, although these are under active research [28].

2.2.4. Targeted Imaging

Whilst the inherent spatial resolution of contrast enhanced ultrasound imaging is still limited, the ability to synthesise molecules targeted to specific cellular receptors which can be incorporated into microbubble coatings has provided opportunities for what is termed as “molecular” imaging [29]. Targeting can be done in a number of different ways. One example is to use microbubbles carrying a net electrical charge, which have been shown to migrate towards inflamed tissue [27]. A more effective alternative is to use ligands (e.g. antibodies, peptides and vitamins) since ligand-receptor interactions are highly specific. Conditions currently under investigation included inflammation, angiogenesis, and atherosclerosis [30,31] the main limiting factors are the biocompatibility and binding rate of targeted microbubbles [32].

2.2.5. Therapeutic Applications

Microbubbles have also been investigated as agents for use in a range of therapeutic applications. Several studies have demonstrated considerable improvements in the efficacy of thrombolytic drugs during exposure to ultrasound in the presence of microbubbles [33,34]. This is thought to be due to a combination of mechanical erosion and more efficient mixing. In high intensity focused ultrasound (HIFU) surgery, microbubbles have been used as a means of promoting cavitation in the target region [35]. Depending on the exposure conditions, this can increase the rate of tissue ablation through a combination of mechanical effects, also known as histotripsy [36], and increased heat deposition which lead to tissue denaturation [37].

At lower ultrasound intensities, microbubbles have been shown to induce temporary and reversible enhancement in the permeability of both individual cells as well as the endothelium [38,39] including the blood-brain barrier [40]. This effect, variously referred to as “sonoporation” and “sonophoresis,” has been shown to significantly increase the uptake of a wide range of different molecules [41,42]. The underlying mechanisms have yet to be fully understood but there is evidence to suggest that both stimulation of normal membrane transport processes and mechanical pore formation [43,44] may both be contributing factors depending on the ultrasound exposure conditions.

In addition to promoting therapeutic uptake, microbubbles can also be used as vehicles for localised drug delivery and gene therapy [45-47]. They can be loaded with a range of different types of therapeutic material during manufacture. They can easily be detected under conventional ultrasound imaging enabling them to be traced to a target site where they can then be destroyed by increasing the ultrasound intensity to release the encapsulated material locally. This can greatly reduce the risk of harmful side effects associated with systemic administration, of toxic chemotherapy drugs for example [48], and specifically can be increased by employing targeting strategies as discussed above.

2.3. Ultrasonic Contrast Agents

2.3.1. Free Gas Microbubbles

The development of ultrasound contrast agents can be traced to the serendipitous discovery in the late 1960s that the presence of gas bubbles in the blood stream produces a strong ultrasound echo. Free gas bubbles may be introduced into tissue during injection as a result of the change in pressure which leads to cavitation at the tip of the needle or catheter. In 1968, Gramiak and Shah [49] were able to confirm that they could repeatedly obtain echoes from the aortic root by injecting saline solution with a catheter in the supravalvular position. Subsequently, other studies demonstrated similar effects with other liquids including Renografin (an X-ray contrast agent), tap water, sucrose solution and indocyanine green [50,51]. The observed contrast enhancement was, however, very short lived, since free gas bubbles of a few micrometres in diameter will dissolve very rapidly whilst larger bubbles will be rapidly removed by filtration in the lungs [52].

2.3.2. Encapsulated Gas Microbubbles

2.3.2.1. Coating Materials

To be useful clinically, gas bubbles must persist for sufficient time to enable the region of interest to be examined. They must also be sufficiently small to traverse the capillary bed of the lung without being destroyed and without posing any risk of causing embolism. Many of the limitations involved in the use of free gas microbubbles as contrast agents can be overcome by the introduction of an encapsulating shell [53]. All current commercially available contrast agents use some sort of encapsulation to increase their persistence [54]. The development of microbubble contrast agents can be separated into first and second generations and is discussed further below. First generation contrast agents, among others, include agitated saline, indocyanine green, sonicated solutions of dextrose, and Renografin. These agents were later superseded by more stable and clinically useful second generation contrast agents which consist of smaller microbubbles and employed a variety of more effective stabilising mechanisms.

Long before the development of ultrasound contrast agents, it was known from studies of bubbles in the ocean that amphiphilic molecules will tend to adsorb on the

surface of a gas bubble reducing the interfacial tension and providing a barrier to gas diffusion [55]. Just as in the ocean, there are a variety of such molecules naturally present in blood and the first encapsulated agent was actually produced by agitating a sample of a patient's blood to produce bubbles which were then re-injected [51,56]. It was determined that the bubble coating in this case consisted primarily of serum albumin and this led to the development of the commercial agent Albunex® (Mallinckrodt Inc.). It was prepared by sonicating a suspension of serum albumin both to produce microbubbles and to crosslink the protein on the bubble surface to improve the stability of the shell [57,58]. Albunex® demonstrated a significant improvement in contrast persistence and the current clinical agent Optison™ (GE Healthcare) is prepared in a similar fashion [59].

Slightly before the introduction of Albunex®, another contrast agent, Echovist® (Bayer Schering) was released. This consisted of galactose microcrystals that would produce free air bubbles upon dissolution [60,61]. As would be expected, Echovist® produced only transient contrast enhancement [62,63] but it was succeeded by another agent Levovist® (Bayer Schering) which employed a surfactant, palmitic acid, to produce more stable bubbles [64].

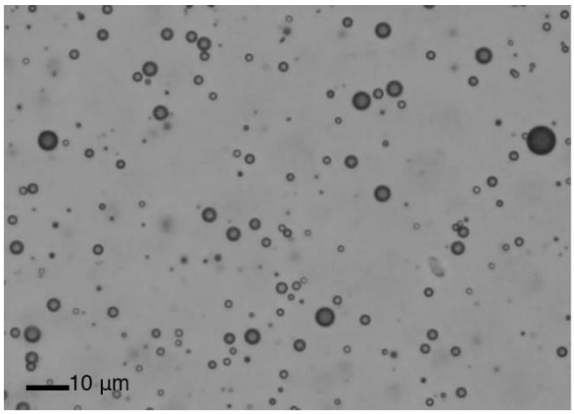

Figure 2.3 – A suspension of SonoVue® microbubbles (Image courtesy of Prof. Eleanor Stride, IBME, Oxford University)

Levovist® microbubbles were still relatively unstable [65-67], but it was subsequently determined that alternative surfactants, most specifically phospholipids, could provide both highly effective stabilization and greater resistance to destruction following ultrasound exposure [68,69]. The latter is thought to be due to the more fluid nature of surfactant coatings compared with those consisting of cross-linked protein which will rupture irreparably beyond a certain

strain [70]. Phospholipid coatings are also less likely to produce adverse immune reactions *in vivo*, particularly if conjugated with e.g. polyethyleneglycol (PEG) [71]. Examples of phospholipid coated microbubble agents include SonoVue® (Bracco Diagnostics) and Definity® (Lantheus Imaging).

A third type of microbubble agent employs a rigid, polymeric shell which is almost entirely "gas-tight" and results in these contrast agents exhibiting much longer life span. One of the first examples of this type of agent was SonaVist® (Bayer Schering) which consisted of air bubbles encapsulated in bio-degradable polymeric shells (cyanoacrylate) [72,73]. However, polymeric shells are both stiffer and usually thicker than their protein or surfactant counterparts which results in this type of bubble being less responsive to ultrasound and thus less efficient as a contrast agent [74]. On the other hand, using a polymeric shell provides a much higher degree of control over the bubble characteristics, in particular determination of the destruction threshold [75] which may be the most desirable feature for some therapeutic applications. Further discussion of the preparation of microbubbles for different applications and new types of microbubble coating are discussed in a later section.

2.3.2.2. Encapsulated Gas

The first generation of encapsulated contrast agent microbubbles (e.g. Albunex®, Levovist®) all contained air [73]. Whilst these showed much better contrast persistence than uncoated microbubbles, their stability was still less than ideal. The second generation of microbubbles therefore employed gases with lower solubility and lower diffusivity in blood in order to prolong contrast enhancement. There are two main groups in this category. First are microbubbles which are filled with perfluorocarbon gases. These are inert gases, immiscible with water which can be injected intravenously if emulsified. Examples of this type are Definity®, Imagent® (IMCOR Pharmaceuticals, Inc.) and Optison® [76-79]. Definity® and Imagent® bubbles have a phospholipid shell, whereas Optison® has an Albumin shell [67,73]. The second group are those filled with Sulphur Hexafluoride. A primary example of this type is SonoVue® which is also phospholipid coated [67,69,80]. It should be noted that whilst second generation contrast agents do show improved stability, they are very sensitive to their environment, especially the temperature and gas saturation and preparation protocol [81].

2.4. Preparation of Ultrasound Contrast Agents

As above, the first encapsulated microbubbles were prepared by agitating a sample of a patient's blood and agitation is still the most straightforward and commonly used method for bubble preparation. Either mechanical shaking or low frequency high intensity sound waves are used to disperse a gas in a suspension of the desired coating material [51]. The rate, time and energy input to the shaking process will all determine the characteristics of the resulting bubble population, specifically the concentration and size distribution [82]. Sonication may also affect the properties of the coating [83].

The most widely clinically approved contrast agents (Optison®, SonoVue®, Definity® and Sonazoid®) are supplied as preformed microbubbles or liposomes which are simply re-suspended before injection (Figure 2.3) [54,67]. A variety of other methods for bubble preparation have also been explored however [84]. EchoVist® and Levovist® microbubbles are formed by the dissolution of crystalline galactose which releases trapped air from crevices within the crystals [67]. The agent EchoGen® relied on the phase change of a volatile liquid at 37^{o}C to produce microbubbles following injection into the blood stream [85]. Whilst EchoGen® was not successful commercially, a similar strategy is now being actively investigated for use in diagnostic and therapeutic applications in which it is desirable for bubbles to exist outside the circulation [86]. Bubbles of a few micrometres in diameter are too large to leave the blood pool which makes them ideal for vascular imaging. Liquid droplets of a few hundred nanometres in size can, however, extravasate and will do so preferentially in regions where the endothelium is more permeable which is frequently the case in cancerous tumours. Once extravasated, the droplets can be "activated" by exposing them to ultrasound and then used for imaging and/or therapeutic delivery [48,87,88].

Both liquid droplets and gas bubbles can also be prepared by high shear emulsification [89] and membrane emulsification, which involves forcing a liquid through a finely meshed membrane into the suspension of the coating material [90]. Neither of these methods, nor agitation/sonication, however, provides a high degree of control over the uniformity of the microbubbles. The bubble size distribution can of course be manipulated by filtration and/or centrifugation [91] but this increases

the processing time and only improves uniformity in terms of bubble size. As will be discussed later, the properties of the coating can also significantly influence the response of microbubbles to ultrasound. Thus for more advanced applications such as quantitative imaging and drug delivery preparation techniques providing better control over microbubble characteristics are desirable.

Ink jet printing has been investigated as a means of preparing drug loaded microbubbles [75] offering excellent control over bubble size. Only liquid components can be processed using this method, however, so subsequent processing to evaporate volatile components is required to produce bubbles. A second method which has been demonstrated for preparing both gas bubbles and capsules containing a volatile liquid is coaxial electrohydrodynamic atomisation (CEHDA) [92]. This method evolved from conventional electrohydrodynamic atomisation, in which a stream of liquid is focused into a jet under the influence of an electric field and then breaks up to form droplets. In CEHDA, a coaxial jet of two fluids is formed and provided the fluids are immiscible then it is possible to encapsulate one fluid inside another. Phospholipid coated microbubbles having a mean diameter of 6.6µm ± 2.5µm, that are stable for over to 2.5 hours at room temperature (~22^{o}C) have been prepared using this technique [93]. The preparation of liquid filled capsules and polymer coated air microbubbles has also been successfully demonstrated [94].

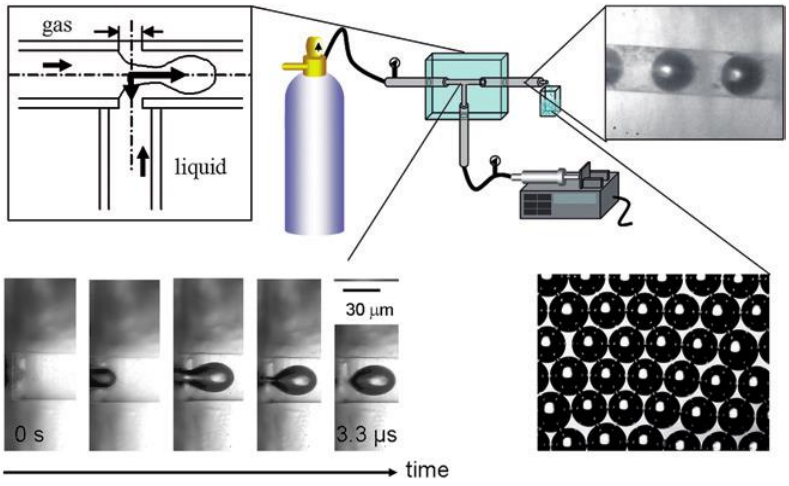

Figure 2.4 - Microbubble preparation using microfluidic device (Capillary T-Junction) along with high-speed images of bubble formation and the resulting monodispersed suspension [95].

The highest degree of uniformity (<1% variation in bubble diameter) reported to date has been achieved using microfluidic devices [96,97]. These have become well established for liquid processing and a wide variety of different designs are

available. An example of setup and microbubbles produced using such a device has been demonstrated in Figure 2.4. Producing microbubbles of uniform size is an important step towards engineering UCAs. The physical principals and feasibility of microfluidic devices for bubble fabrication is considered in greater detail in chapter 5. The relative advantages and disadvantages of bubble preparation techniques are further discussed in [95].

Therapeutic components can be incorporated into microbubbles via a range of different means. A thin layer of oil containing a lipophilic drug [98] can be included between the gas core and the outer shell. Aqueous solutions can be incorporated in the centre of a lipid bilayer, the intermediate layer of which contains gas to provide ultrasound responsiveness. This type of vehicle is sometimes known as an echogenic liposome [99]. Charged therapeutics such as DNA and RNA can be coupled electrostatically onto the shell when cationic lipids or denatured proteins are present, which can be used for gene transfection experiments [100]. Multi-lamellar shells have been used to improve loading efficiency [101]. Similarly, nanoparticles have been successively loaded into the shell [102] and attached through biotin-avidin linkages [71,103].

2.5. Equations of Motion for Nonlinear Oscillations

The ability of microbubbles to scatter ultrasound so effectively is largely due to their compressibility. This can best be understood by considering the pressure balance at the surface of a spherical gas bubble suspended in an infinite volume of liquid which may be expressed as:

$$p_g = p_l + \frac{2\sigma}{R} \tag{2.2}$$

Where p_g is the pressure of the gas inside the bubble, p_l is the pressure in the liquid at the bubble wall, σ is the interfacial tension and R is the bubble radius. Any change in the liquid pressure, e.g. due to the application of an external sound field, will therefore result in a change in the gas pressure inside the bubble.

Assuming the gas inside the bubble to be ideal, p_g can be written as:

$$p_g\left(\frac{4}{3}\pi R^3\right) = nBT \tag{2.3}$$

where B is the universal gas constant, n is the number of moles of gas contained within the bubble and T is the absolute temperature. Any variation in p_g will require a corresponding variation in n, and/or T and/or R, i.e. the mass, temperature or volume of the bubble. The timescales associated with mass and heat transfer are very slow compared with the length of a typical ultrasound pulse (~1-2 μs). The bubble volume on the other hand can easily change due to the high compressibility of the gas inside. Thus, when exposed to an ultrasound field, a gas bubble will undergo volumetric oscillations in response to the varying pressure [104,105].

In all dynamic equations presented in the next section, the expansion and compression of the filling gas is assumed to be polytropic. This means that the relation between gas pressure and volume can be written as,

$$p_g \left(\frac{4}{3} \pi R^3 \right)^k = \text{constant} \tag{2.4}$$

where k is the polytropic index. This relation can characterise a wide range of thermodynamic processes and is applicable to the gases used in UCA's manufacture and typical compression rates and ratios. For example, k=1 for an isothermal process or γ for an adiabatic process where γ is the ratio of specific heats [106].

2.5.1. Free Gas Bubbles

Once the bubble begins to oscillate, the liquid next to the bubble wall will also be set into motion and so influence the bubble dynamics. Thus, to fully describe the response of a microbubble to ultrasound excitation it is necessary to consider the inertia of the surrounding liquid. A number of different models have been developed to describe mathematically the motion of the bubble wall. The earliest published attempt to model the liquid pressure as the result of the collapse of a spherical cavity, in an infinite, inviscid and incompressible liquid, inside which is a vacuum, was carried out by **Besant** [107]. It equates the acceleration of the bubble wall to the pressure balance across it:

$$R\ddot{R} + \frac{3}{2}\dot{R}^2 = \frac{p_l - p_\infty}{\rho_l} \tag{2.5}$$

In this equation, $\dot{R}$ and $\ddot{R}$ denote the velocity and acceleration of the cavity wall respectively, ρ_l is the density of the liquid surrounding the cavity, p_l is the pressure in the liquid at the cavity wall and p_∞ is the pressure at a large distance from the cavity.

Lord Rayleigh extended Besant's equation to account for the pressure in the interior of the fluid [108]. This was then progressed by an important paper by **Plesset** [109] which described the dynamics of vapour filled bubbles. These attempts, however, were concerned with hydrodynamically generated cavities. Subsequent work by **Blake** [110], **Noltingk** and **Neppiras** [111] and **Poritsky** [112] concerned themselves specifically with acoustically generated gas microbubbles and included the effects of viscosity and surface tension.

The resulting equation, commonly called Rayleigh-Plesset-Noltingk-Neppiras-Poritsky (RPNNP) following the suggestion from Lauterborn [113], forms the basis of the various nonlinear equations of motion for gas microbubbles available today:

$$R\ddot{R} + \frac{3}{2}\dot{R}^2 = \frac{1}{\rho_l}\left(\left(p_0 + \frac{2\sigma}{R} - p_v\right)\left(\frac{R_o}{R}\right)^{3\kappa} + p_v - \frac{2\sigma}{R} - \frac{4\mu_l\dot{R}}{R} - p_0 + p_A(t)\right) \qquad (2.6)$$

where p_v is the vapour pressure, κ is the polytropic constant, μ_l is the viscosity of the surrounding liquid, $p_A(t)$ is an imposed pressure field, and R_o is the initial bubble radius.

It is assumed in deriving (2.6) that the bubble is suspended in an infinite body of liquid; that the ultrasound wavelength is much larger than the bubble radius as $p_A(t)$ must be constant on the bubble surface; that there is no heat or mass transfer during the bubble oscillation; that the filling gas obeys the polytropic law; that the density of the liquid is very large compared with that of the gas; and that the speed of the bubble wall never approaches the speed of sound in the liquid so the liquid can be treated as incompressible and its density as constant.

Indeed it has been shown that (2.6) agrees well when compared with the Navier-Stokes equation solved numerically [114]. These assumptions are acceptable for microbubbles under typical diagnostic exposure conditions. At the higher ultrasound intensities that may be encountered in therapeutic applications, however, it may require modification. The assumption of liquid incompressibility, in particular, becomes unreliable as the wall velocity approaches the speed of sound. To fully

describe the microbubble dynamics requires simultaneous solution of the equations for conservation of mass, momentum and energy. This is computationally intractable for most cases. Several equations of motion have been presented in the literature which include approximations for the effects of liquid compressibility and the resulting energy dissipation due to acoustic re-radiation; most notably by Herring [115], Trilling [116], Gilmore [117], Tomita and Shima [118,119], and Keller and Miksis [120].

The assumption of incompressibility results in the liquid density being treated as a constant. Consequently the speed of sound in the liquid becomes infinite, a fact which limits the applicability of (2.6). Assuming that the speed of sound in the liquid is a finite constant ($c = c_\infty = \text{const}$), **Herring** [115,121] derived an approximation which considered the compressibility of the liquid. This was later improved by **Trilling** [116] who obtained the results as Herring's using a simpler method and derived expressions for the velocity and pressure throughout the liquid. Both of these formulations were of first order and can describe the collapse of bubbles with low expansion ratios. Second order modelling was conducted by **Gilmore** [117] using the Kirkwood and Bethe approximation [122] which assumes that the speed of sound is a function of pressure. Gilmore's equation can be written as:

$$\ddot{R}R\left(1-\frac{\dot{R}}{c}\right)+\frac{3}{2}\dot{R}^2\left(1-\frac{\dot{R}}{3c}\right)=H\left(1+\frac{\dot{R}}{c}\right)+\frac{R}{c}\left(1-\frac{\dot{R}}{c}\right)\frac{dH}{dt} \qquad (2.7)$$

where H is the difference in the liquid enthalpy between the bubble wall and infinity, and c is the speed of sound in the liquid at the bubble wall. Both c and H are functions of liquid pressure $p_l(t)$. It was thought that the Kirkwood-Bethe hypothesis would only be accurate when all the liquid velocities were small compared to the velocity of the sound in the liquid. Gilmore observed, however, that the results agreed well with other solutions up to a bubble wall velocity of 2.2 times the sonic velocity and was suitable for very large amplitudes of oscillation [117]. Using the Poincaré-Lighthill-Kuo (PLK) method [123], **Tomita and Shima** developed an equation of motion for a spherical bubble in compressible and viscous liquid that is valid for the second order approximation [118,119]. Their results agreed very well with the experimental data obtained by Lauterborn and Bolle [124], and Shima and Tomita [119]. **Keller and Miksis** [120] derived an equation for free

and forced bubbles which took into account the effect of acoustic re-radiation, the incident sound wave, and the liquid viscosity and surface tension.

$$\ddot{R}\left(\frac{4\mu_l}{\rho_l}-R\left(\dot{R}-c\right)\right)=\frac{\dot{R}^3}{2}+\dot{R}\Delta\left(R\right)-c\left(\frac{3}{2}\dot{R}^2+\frac{4\mu_l\dot{R}}{\rho_l R}+\frac{2\sigma}{\rho_l R}-\Delta\left(R\right)\right)$$
$$+R\dot{R}\Delta'\left(R\right)+\left(1+\frac{\dot{R}}{c}\right)\frac{\left|p_A\left(t\right)\right|c}{\rho_l}\sin\omega\left(t+\frac{R}{c}\right) \tag{2.8}$$

Here $\Delta\left(R\right)$ is the pressure difference divided by the liquid density: $\rho_l^{-1}\left(p_{gc}R^{-3\kappa}+p_v-p_\infty\right)$, and p_{gc} is a constant determined by the quantity and the type of gas inside the bubble. Various studies have reviewed the validity of some or all of these models, most notably by Vokurka [125] and Prosperetti and Lezzi [126]. Prosperetti and Lezzi [126] solved the complete partial differential formulation of a bubble radial motion and compared the results with those from other available models. They found that all of these treatments had a similar degree of accuracy to the first order of Mach number, with Keller's equation offering a slight advantage in predicting the minimum radius and velocity in a collapsing bubble as well as the maximum velocity during the rebound which occurs shortly after the minimum radius. More recently Fuster [127] presented a complete solution for the motion of a bubble in a compressible liquid which solved the continuity and momentum equations for both inside and outside of the bubble. Other attempts at including the effect of compressibility in the form of an analytical model include Flynn [128], Lastman and Wentzell [129], and Moshaii *et al.* [130].

For larger bubbles at lower frequencies, heat transfer may no longer be negligible and this can be addressed by removing the polytropic approximation for the gas pressure in (2.6) and instead coupling this to an appropriate equation of state for the gas [131]. Similarly, over many cycles, diffusion of gas across the bubble wall may become significant and this is discussed further later on.

2.5.2. Coated Gas bubbles

As mentioned previously, microbubbles used for biomedical applications are normally encapsulated and the effect of the coating must also be taken into account in any model describing their behaviour.

Models for the dynamics of coated bubbles in the ocean have been available since the 1950s [55] but **de Jong *et al.*** [132] were the first to describe the vibrations of an ultrasound contrast agent microbubble. The model was based on (2.6) and was developed to describe the oscillations of albumin coated bubbles such as Albunex®. The theory was accompanied by substantial experimental results [133] and demonstrated that the shell surrounding Albunex® behaved as layers of elastic solids. The incorporation of the shell effect, however, was carried out as an *ad hoc* addition to the RPNNP equation, resulting in:

$$\rho_l\left(R\ddot{R}+\frac{3}{2}\dot{R}^2\right)=\left(p_\infty+\frac{2\sigma}{R_0}-p_v\right)\left(\frac{R_0}{R}\right)^{3\kappa}+p_v-\frac{2\sigma}{R}-2S_p\left(\frac{1}{R_0}-\frac{1}{R}\right) \\ -\delta_t\omega\rho_l R\dot{R}-p_\infty-p_A. \tag{2.9}$$

In this equation, the effect of the encapsulation was described in terms of a shell elasticity, S_p, and shell friction parameter, S_f. The former was included in an additional elastic resistance term and the latter was included in the effective total damping coefficient δ_t. The total damping coefficient also incorporated the effects of liquid viscosity, δ_{vis}, thermal damping, δ_{th}, and radiation damping δ_{rad} given by Medwin [134] as

$$\delta_t=\delta_{rad}+\delta_{vis}+\delta_{th}+\frac{S_f}{\left(4\pi R^3\rho_l\omega\right)} \quad . \tag{2.10}$$

Subsequently, **Church** [135] derived a model from first principles for a microbubble coated with a viscoelastic solid shell of finite thickness. Through a more rigorous theoretical treatment, Church applied the Kelvin-Voigt constitutive law, which linearly relates the viscoelastic stresses to the strain and rate of strain tensors, to the microbubble shell. It is effectively Hooke's law with an added viscous term. Church's equation is thus written as

$$\rho_s R_1\ddot{R}_1\left[1+\left(\frac{\rho_l-\rho_s}{\rho_s}\right)\frac{R_1}{R_2}\right]+\rho_s\dot{R}_1^{\,2}\left[\frac{3}{2}+\left(\frac{\rho_l-\rho_s}{\rho_s}\right)\left(\frac{4R_2^{\,3}-R_1^{\,3}}{2R_2^{\,3}}\right)\frac{R_1}{R_2}\right]= \\ p_0\left(\frac{R_{01}}{R_1}\right)^{3\kappa}-\frac{2\sigma_1}{R_1}-\frac{2\sigma_2}{R_2}-p_\infty-p_A-\frac{4\dot{R}_1}{R_1}\left(\frac{V_s\mu_s+R_1^{\,3}\mu_l}{R_2^{\,3}}\right)-\frac{4V_sG_s}{R_2^{\,3}}\left(1-\frac{R_{e1}}{R_1}\right). \tag{2.11}$$

The subscripts *1* and *2* refer to the inner and outer radius of the shell and subscripts *s* and *l* refer to shell and liquid respectively. G_s and μ_s are the shear modulus and shear viscosity of the shell respectively. V_s and R_{e1} are given by:

$$V_s = R_{02}^{\ 3} - R_{01}^{\ 3} \tag{2.12}$$

$$R_{e1} = R_{01}\left[1+\left[\frac{2\sigma_1}{R_{01}}+\frac{2\sigma_2}{R_{02}}\right]\left[\frac{R_{02}^{\ 3}}{V_s}\right]\left(4G_s\right)^{-1}\right] \tag{2.13}$$

The effect of thermal and radiation damping may be included by the *ad hoc* addition of expressions given by Prosperetti [136]. Several important observations regarding the dynamics of single microbubbles were made in this study. The resonance frequency of the microbubble increases with the increase in the rigidity of its shell. For bubbles whose radii are less than ~10μm, the effect of thermal damping is negligible compared to viscous damping. In contrast to free bubbles, the inclusion of the encapsulation results in a reduction of internal gas pressure which in turn decreases the effect of thermal damping. Finally it was shown that the scattering cross section decrease as the viscosity of the surface layer increases with the effect having a larger impact on the second harmonic.

Later on, **Hoff *et al.*** [137] simplified Church's model by applying it in the limit of small shell thickness in comparison with microbubble radius:

$$\rho_l\left(R\ddot{R}+\frac{3}{2}\dot{R}^2\right) = p_0\left[\left(\frac{R_0}{R}\right)^{3\kappa}-1\right]-p_A-4\mu_l\frac{\dot{R}}{R}-12\mu_s\frac{d_{s0}R_0^{\ 2}}{R^3}\frac{\dot{R}}{R}-12G_s\frac{d_{S0}R_0^{\ 2}}{R^3}\left(1-\frac{R_0}{R}\right). \tag{2.14}$$

Here d_{s0} is the initial thickness of the shell. The implementation of shell thickness in the shell viscosity and elastic modulus is in terms of constant relative shell thickness (d_{s0}/R=const). It was indeed found that assuming a constant shell thickness in the model as opposed to a constant relative shell thickness resulted in poor agreement between the measurements and calculations for any combination of G_s and μ_s. The elastic modulus and shear viscosity of the shell were established by inserting values to fit the acoustic measurements. These terms were treated as constant in the insonation frequency range of 1-8 MHz, although they are known to be frequency dependant [138]. The contributions of radiation and thermal damping were considered in the linearized version of (2.14). It was found that for microbubbles of diameters of 4-8μm and insonation frequencies below 10 MHz, these damping

mechanisms were insignificant and the shell viscosity was the dominant damping mechanism. Other conclusions were similar to those obtained by Church [135].

The dynamic models mentioned above all considered microbubbles with relatively hard shells. Microbubbles with more flexible coatings such as phospholipids, however, exhibit much larger amplitudes of oscillation compared to their hard shelled counterparts. It can be argued that the coatings of such bubbles should be treated as adsorbed interfacial layers rather than discrete shells. Early attempts at explaining the effect which an organic coating imposes on the dynamics of microbubbles was investigated by Fox and Herzfeld [139] and later in more detail by Glazman [140].

Building on earlier work for oceanic bubbles [141], **Morgan *et al.*** [142] developed a model for vibrations of a surfactant coated microbubble using a modified Herring-Trilling equation [143]. The influence of the coating was however, still characterised through an effective elasticity parameter, χ, given by Glazman [140] and a viscosity, μ_s making it essentially equivalent to Hoff's treatment, albeit through slightly different functional relationships:

$$\begin{aligned}\rho_l\left(R\ddot{R}+\frac{3}{2}\dot{R}^2\right)&=\left(p_0+\frac{2\sigma}{R_0}+\frac{2\chi}{R_0}\right)\left(\frac{R_0}{R}\right)^{3\kappa}\left(1-\frac{3\kappa}{c}\dot{R}\right)\\&-\frac{4\mu_L\dot{R}}{R}-\frac{2\sigma}{R}\left(1-\frac{1}{c}\dot{R}\right)-\frac{2\chi}{R}\left(\frac{R_0}{R}\right)^2\left(1-\frac{3}{c}\dot{R}\right)-12\mu_s d_s\frac{\dot{R}}{R\left(R-d_s\right)}-p_0-p_A\end{aligned} \tag{2.15}$$

The properties of the microbubble were determined by the use of high speed streak imaging, which was a departure from the studies by the other authors previously mentioned. The elasticity parameter χ was found to have little to no effect in comparison to the shell viscosity. It was also observed that the elasticity parameter had no dependence on the equilibrium bubble radius unlike the shell viscosity, μ_s, which seemed to relate to R_0 in a linear fashion.

The derivation of the effective surface tension in Glazman's paper contained an error which was also propagated in the Morgan's model. This was commented on by **Marmottant *et al.*** [144] who observed that Glazman's formulation predicts a reduction in effective surface tension on the inflation of the microbubble. This directly contradicts the physical behaviour of lipid monolayers or polymeric

coatings. Referring to Langmuir-Blodgett measurements for dynamic surface tension of flat monolayers, Marmottant *et al.* [144] formulated a new surface concentration dependant surface tension. This was implemented via an *ad hoc* law in which the behaviour of the coating was partitioned in three regimes. Within the "linear" regime the lipid coating is assumed to provide a linear elastic resistance. Beyond the two extremes of this range, the surface is either assumed to be buckled or ruptured. Buckling is deemed to occur when the bubble is compressed beyond a limiting radius at which point the interfacial tension will be zero. Rupture occurs when the bubble exceeds an upper limiting radius at which point the surface concentration will be so low that the interfacial tension will be equal to that of an uncoated bubble. Marmottant's equation is given as

$$\rho_l\left(R\ddot{R}+\frac{3}{2}\dot{R}^2\right)=\left(p_0+\frac{2\sigma_0}{R_0}\right)\left(\frac{R_0}{R}\right)^{3\kappa}\left(1-\frac{3\kappa}{c}\dot{R}\right)-\frac{4\mu_l\dot{R}}{R}-\frac{2\sigma(R)}{R}-\frac{4\kappa_s\dot{R}}{R} \qquad (2.16)$$
$$-p_0-p_A,$$

where κ_s is the surface dilatational viscosity, and σ_0 is the initial interfacial tension at the bubble surface. Although κ_s is not treated as surface area dependent in the above equation, Van der Meer *et al.* later suggested a relation clearly showing a decrease in shell viscosity with dilation rate [145]. Morgan *et al.*[142] derived a formulation for a layer of finite and constant thickness, relating κ_s to the bulk shear viscosity of a lipid suspension. Equation (2.16) is capable of predicting experimentally observed phenomena such as 'compression only behaviour', in which the compression amplitude is greater than the expansion amplitude [146], subharmonic response, and 'thresholding' in which a microbubble responds only above a certain excitation pressure.

Whereas Marmottant *et al.*[144] used an *ad hoc* law to describe the dynamic surface tension, **Stride** [147] independently developed a model in which both interfacial tension and viscosity are functions of the surface molecular concentration Γ. In this treatment, the effects of initial surface concentration Γ_o and the characteristics of the given surfactant, represented by a constant *K*, are separated to allow for variations in bubble behaviour due to different levels of adsorption. Both interfacial tension and viscosity are also treated as continuous functions obeying a power law and

exponential relationship in accordance with reported experimental observations [148]:

$$\begin{aligned}&\rho_l\left(R\ddot{R}+\frac{3}{2}\dot{R}^2\right)+p_o-p_A-p_g\left(R\right)+\frac{4\dot{R}}{R}\mu_l\\&=-\frac{4\dot{R}}{R^2}\kappa_{so}e^{\frac{ZR_x^2}{\left(R^2-R_x^2\right)}}-\frac{2}{R}\left(\sigma_o+\frac{K\Gamma_o^{x_s+1}}{\left(x_s+1\right)}\left(1-\left(\frac{R_o}{R}\right)^{2\left(x_s+1\right)}\right)\right).\end{aligned}\tag{2.17}$$

Here Γ_o is the initial surface molecular concentration, κ_{so}, K, x and Z are constants for a given surfactant and R_x is the limiting bubble radius beneath which the surface buckles [149] and the interfacial tension will be reduced to zero. It should be noted that accurate methods for performing independent measurements of the coating properties have yet to be developed. Thus all the values used in published studies are derived indirectly by fitting experimental results to a given model. The effects of liquid compressibility can be included in equations of this type either through correction factors such as those discussed above or following the approach of e.g. Keller and Miksis [120] discussed previously. It should be noted however that other assumptions, such as the integrity of the microbubble coating and spherical symmetry are likely to become invalid before liquid compressibility becomes significant. The effect of surfactant shedding during multiple insonation cycles was considered by O'Brien *et al.* [150] where surfactant film was ejected after its concentration exceeded a maximum value. Surfactant adsorption through convective diffusion was also considered. The time scale associated with this mechanism was found, however, to be much longer than pulse lengths typically used in medical ultrasound.

2.5.3. Scattered signal

The echoes produced by contrast agent microbubbles can be predicted by considering each microbubble as a spherical source of sound. Potential flow theory can then be implemented to predict the pressure scattered or reradiated from the bubble at a distance r from its centre [151]:

$$p_{scat}\left(r,t\right)=\rho_l\left(\frac{1}{r}\left(R^2\ddot{R}+2R\dot{R}^2\right)-\frac{R^4\dot{R}^2}{2r^4}\right)\tag{2.18}$$

where R, $\dot{R}$ and $\ddot{R}$ are determined by solving (2.6) or indeed any of the equations of motion detailed previously in section 2.5.2. Strictly, (2.18) should be solved simultaneously with a dynamic equation that contains the appropriate treatment of re-radiation damping to ensure conservation of energy is satisfied. The effect of radiation damping upon the radial dynamics is usually small, therefore (2.18) can be used independently with acceptable accuracy. Note that (2.18) does not describe the attenuation of the reradiated field in the surrounding liquid but this is negligible compared with the attenuation due to the bubbles themselves.

2.6. Oscillation of Ultrasound Contrast Agents

2.6.1. Linear Oscillations

At very low excitation pressures both coated and uncoated bubbles undergo oscillations that are primarily linear (Figure **2.5**a). For this regime, it is useful to linearize the nonlinear equation of motion. For example, assuming very small variations in radius such that $R = R_0(1+z)$, where $z << 1$, equation (2.6) can be reduced to a generic second order ODE of the familiar form of:

$$m\ddot{z} + b\dot{z} + kz + = p_A(t) \tag{2.19}$$

where $m = \rho_l R_o^2, b = (4\mu_l), k = \rho_l R_o^2 f_{res}{}^2$ and f_{res} is the resonance frequency given by equation (2.20).

$$f_{res}{}^2 = \frac{1}{\rho_l R_0{}^2}\left(3\gamma\left(p_0 + \frac{2\sigma}{R_0}\right) - \frac{2\sigma}{R_0}\right) \tag{2.20}$$

This analytical solution provides a useful approximation for determining the excitation parameters under which the microbubbles will respond most efficiently.

2.6.2. Non-linear oscillations

With increasing excitation pressure, the amplitude of the bubble oscillations increases and becomes nonlinear, with the bubble contracting more than it expands over each cycle (Figure **2.5**b). Equation (2.20) is then no longer strictly valid and the frequency at which the amplitude of oscillation is maximized becomes dependent on pressure [152,153]. Under these conditions the bubble will still undergo repetitive

oscillations, but periodicity may only be observed over several cycles [154]. This is sometimes referred to as non-inertial or stable cavitation. In diagnostic imaging, this behaviour is desirable because the non-linear oscillations produce echoes which contain not only the frequency of the incident ultrasound field but also multiples (harmonics) of this frequency which can be used to distinguish the bubble echoes from those produced by the surroundings. A variety of signal processing techniques have been developed to exploit these and produce images with high contrast to tissue ratios [3,155,156]. The harmonic components, which may be whole or fractional, can also be used in the monitoring of therapeutic applications although the relationship between frequency content and bubble dynamics is often complex [157].

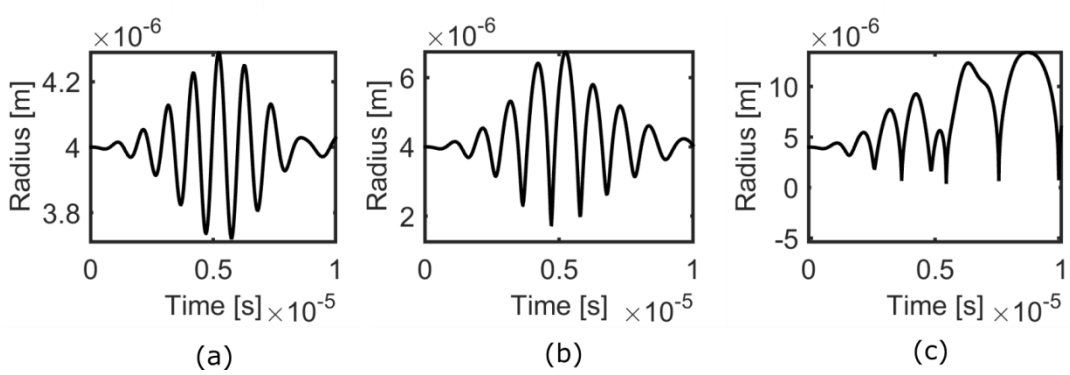

Figure 2.5 - Examples of various oscillation modes for an uncoated bubble of radius 4μm in water (ρ_l = 1000 kgm^{-3}, σ = 0.072 Nm^{-1}, μ = 1.002 Pa.s). The R-t plots are calculated using the RPNNP equation which was numerically integrated using the 4th and 5th order Runge-Kutta routine (ODE45) in MATLAB® 2012b (Mathworks Inc.) . The incident acoustic wave in all cases is a 10 cycle Gaussian pulse of f = 1.0MHz and the peak acoustic pressure is changed for each case; a) Linear Oscillations @ P_A=15kPa; b) Nonlinear Oscillations @ P_A=150kPa; c) Inertial collapse Oscillations @ P_A=500kPa.

The nonlinear radiation from the microbubbles should not be confused with the nonlinear components introduced by nonlinear propagation of an ultrasound wave which will also be scattered by the microbubbles and contribute to the overall nonlinear content of the ultrasound echo. In diagnostic ultrasound, however, the effect of these components is usually small.

2.6.3. Inertial Collapse

Eventually with increasing pressure the periodic nature of the oscillations is lost (Figure **2.5**c). These oscillations may become chaotic and the bubbles undergo violent collapse, releasing a shock wave and often fragmenting into smaller bubbles [158]. This process is variously referred to as inertial, unstable, or transient cavitation. Transient and unstable are both slightly misleading terms since a bubble

can collapse repeatedly [159] without fragmenting. “Inertial” refers to the analysis by Flynn [160] in which he demonstrated that an approximate criterion for predicting when a bubble will undergo violent collapse can be derived by comparing the magnitude of two terms in (2.6) given by:

$$f_I = \frac{3\dot{R}^2}{2R}$$
$$f_p = \frac{1}{\rho_L R}\left(\left(p_o + \frac{2\sigma}{R} - p_v\right)\left(\frac{R_o}{R}\right)^{3\kappa} + p_v - \frac{2\sigma}{R} - \frac{4\mu_L \dot{R}}{R} - p_o + p_A(t)\right). \quad (2.21)$$

f_I describes the influence of the inertia of the surrounding liquid on the bubble oscillation. f_p describes the influence of the internal pressure of the bubble. Inertial cavitation is said to occur if the liquid inertia dominates the collapse process, so that at the point when f_p reaches a minimum, the magnitude of f_I is greater than the magnitude of f_p.

2.7. Stability of Ultrasound Contrast Agents

2.7.1. Static Diffusion

A microbubble will never be completely stable due to the pressure acting on its surface from the interfacial tension (2.2) and the gas concentration gradient between the bubble core and the surrounding liquid. Fick’s first law states that the concentration gradient will result in a net flux of gas from the area of high concentration to the area of lower concentration. Assuming Henry’s law applies at the gas/liquid interface and the gas concentration throughout the liquid is initially constant, for a single bubble in a liquid of infinite volume at constant temperature and pressure, Epstein and Plesset [10] derived an equation for the rate of change of bubble size:

$$\dot{R} = \frac{D(C_i - C_{sat})}{\left(\rho_{g\infty} + \frac{4M\sigma_o}{3RBT}\right)}\left\{\frac{1}{R} + \frac{1}{\sqrt{\pi D t}}\right\}, \quad (2.22)$$

where D is the coefficient of diffusion, C_i is the initial concentration of gas in the liquid, C_sat is the saturation concentration of gas in the liquid, $\rho_{g\infty}$ is the density of the gas (for zero interfacial curvature), M is the molecular weight of the gas, σ_0 is the

interfacial tension, *R* is the bubble radius, *B* is the universal gas constant, T is the absolute temperature and *t* is time.

In deriving (2.22), convective effects were neglected. The fully coupled mass transport problem has been solved by Ready and Cooper [161] and Weinberg [162] but they showed that the effects of convection, particularly for bubbles with diameter of less than 1.0 mm, were very small. In addition, controlled experiments on single microbubbles (5-50 μm range) by Brent and Needham [163] using a micropipette technique showed good agreement with (2.22), particularly for microbubbles smaller than 15 μm.

2.7.2. Rectified Diffusion

Whilst a stationary bubble will tend to dissolve, under ultrasound exposure bubbles have been observed to increase in size through a process known as rectified diffusion; a phenomena first proposed by Blake in 1949 [164]. There are two main mechanisms underlying this process [9]:

The Area Effect – gas diffusion will occur in both directions across the bubble surface owing to the varying pressure gradient. The surface area of the bubble however will be smaller during compression than during expansion. Thus the degree to which gas diffuses into the bubble may exceed that to which it diffuses outwards into the liquid.

The Shell Effect – in addition, the local concentration of gas in the liquid close to the bubble surface will be higher during bubble expansion than during compression, and this again encourages inwards diffusion.

Whether or not a bubble experiences rectified diffusion depends on its initial size, the frequency and pressure of the incident field, and the solubility and concentration of the gas in the surrounding liquid [165]. To fully describe the dissolution or growth of a bubble requires coupling of Fick's equation with one of the available dynamic equations [166]. Approximate thresholds for rectified diffusion can however be determined and have been reported for uncoated bubbles [9,167]. Contrast agent microbubbles will tend to dissolve, especially under diagnostic conditions which involve short pulses and low pulse repetition frequencies [168]. Bubble growth has been observed [169] but this is thought to have been due to either an increase in

temperature which will increase the size of the bubble according to the equation of state or absorption of oxygen into the perfluorocarbon core rather than rectified diffusion. It has been suggested that rectified diffusion is essential for the generation of cavitation bubbles in therapeutic applications but this is still an area of some controversy [168].

2.7.3. Stability from Surface Coating

Addition of an encapsulating shell can significantly alter the longevity of a microbubble. Both the interfacial tension and diffusivity may be substantially modified and in the case of polymers and some surfactants effectively reduced to zero [170]. Modified versions of (2.22) for coated bubbles have been derived by Sarkar *et al.* and Borden *et al.* [171,172].

The effect of an adsorbed surfactant layer upon gas diffusion for oscillating bubbles has been investigated by Fyrillas and Szeri [173] who found that a soluble surfactant could either enhance or inhibit bubble growth by rectified diffusion, depending on the exposure conditions. This corresponded to the experimental findings reported by Crum [165]. An equivalent treatment to that described above for gas diffusion may also be applied to the concentration of molecules adsorbed on the bubble surface. As above, this concentration can have a significant effect upon bubble oscillations so this is likely to be a cause of changes in bubble behaviour over time which have been observed in experiments [174].

Some changes (in bubble size and amplitude of oscillation) have however, been observed over the course of a single ultrasound pulse which is too rapid to be explained by conventional diffusion processes. Experimental observations [175] suggest that in addition to adsorbing/desorbing surfactant molecules may be rapidly ejected or “shed” from the bubble surface during oscillation. Theoretical models describing this phenomena and its influence upon microbubble size and oscillations have been developed by O’Brien *et al.* [176]. Based on the description of lung surfactant by Morris *et al.* [177] they defined three regions of adsorption/desorption, insolubility, and film collapse where surfactant ejection occurs. The maximum concentration limit is regularly exceeded at large amplitudes of oscillation and lipid shedding then occurs.. After a number of pulses, microbubbles tend to reach a stable radius. This may be attributed to either a change in coating structure or reduction in

amplitude of oscillation because the bubble is no longer of resonant size. Their findings also confirmed that the effect of diffusion (gas or surfactant) over the duration of a typical pulse length used in ultrasound diagnostics is insignificant.

2.8. Summary

The aim of this chapter was to provide an overview of the existing research on microbubble contrast agents. It was shown that microbubbles are employed successfully in a variety of diagnostic and therapeutic applications. A brief history of their development was followed by a review of fabrication methods that have been applied to ultrasound contrast agents. There will be a more detailed discussion of microfluidic method of fabricating microbubble contrast agents in chapter 5 where computer simulations of the process are developed and presented.

Microbubbles have been the subject of theoretical treatments since the early 20^{th} century. In this chapter, a detailed account of the theoretical treatments applied to microbubble contrast agents was given. It is important to appreciate the multitude of available theoretical treatments and their development timeline. The findings in this section will be used in the next chapter where a new description of the microbubble shell behaviour is presented to account for the effect of nanoparticles upon microbubble oscillations.

A number of mechanisms affecting the stability of ultrasound contrast agents were also discussed. When not in oscillation, the diffusion of gas from the microbubble to the surrounding liquid is the main source of its instability with the gas concentration gradient and interfacial tension being the main drivers. In this work, it is proposed that inclusion of nanoparticles in the coating will resist this mechanism of dissolution. This will be investigated through a modification to equation (2.22). The results will then be compared to experimental results obtained by collaborators.

3. Armoured Microbubble Dynamics

3.1. Overview

Increasing the detectability of UCAs was highlighted in Chapter 1 as one of three important aspects in their development. An effective method of achieving this is to subject the UCA to high insonation pressures. Whilst this increases the fundamental signal from the UCA, it also causes it to behave in a nonlinear fashion. The presence of harmonic components in the scattered pressure signal enables it to be distinguished from its surroundings. Major improvements in this area have been achieved through signal processing with a proliferation of harmonic imaging techniques [178]. Further amplification of insonation pressure should theoretically increase the amplitude of harmonic content within the signal. There is, however, a point after which increasing the insonation pressure ceases to be beneficial. First, the likelihood of UCA destruction increases with pressure and, second, so does the risk of harmful bio-effects through inertial cavitation or rise in tissue temperature [179]. In addition, nonlinear acoustic wave propagation through tissue becomes noticeable at high acoustic pressures and consequently may make it difficult to distinguish signals coming from the tissue from those from UCAs. It is therefore desirable to fabricate UCAs which exhibit enhanced nonlinearity at low insonation pressures.

The presence of harmonic content in the UCA signal is due to its asymmetric oscillations in response to a symmetric acoustic pressure wave. Asymmetry here is defined as an inequality in the amplitude of expansion and contraction of the UCA rather than a departure from spherical symmetry. The harmonic content could therefore be enhanced if the expansion to contraction ratio was increased. This requires engineering microbubbles that exhibit nonlinear resistance to deformation. One method of achieving this is to embed nanoparticles within the microbubble coating. The particles are able to move freely during expansion, but would resist further motion upon reaching a certain surface density at which point they press together, or “jam”. Bubbles with particulate coatings are often described as “armoured” in the literature [180,181].

This chapter is mainly concerned with investigating the extent to which embedding nanoparticles in a microbubble shell will affect the nonlinearity of its oscillations. First, equations of motion for nanoparticle coated microbubbles with both finite thickness and infinitely thin coatings are derived. The effect of nanoparticles on UCA dynamics is then modelled by defining effective properties for the shear viscosity and modulus of its coating. Using the model, results are obtained for a range of microbubble characteristics and excitation conditions and compared to experimental findings where possible. The chapter concludes with a discussion of the validity of the model and implications of the results for applications of nanoparticle coated microbubbles.

3.2. General Dynamic Equations

The aim of this section is to derive equations to describe the response of a coated contrast agent microbubble to a time-varying pressure. The geometry and environment of a bubble with a finite thickness coating is shown in Figure 3.1. The bubble is modelled as a spherical volume of gas enclosed by a homogenous outer layer of an incompressible linear viscoelastic solid and surrounded by an incompressible fluid. The bubble is assumed to be far from any boundary, and thus maintains spherical symmetry during oscillation.

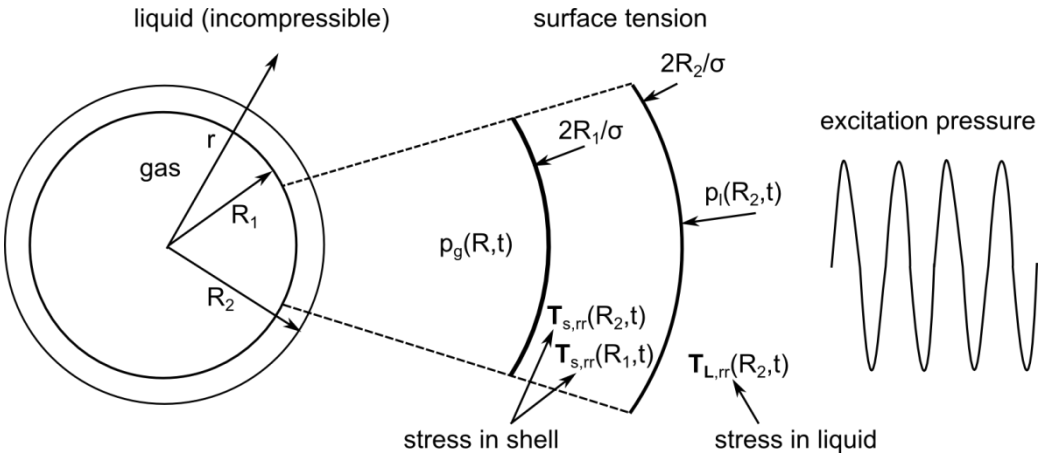

Figure 3.1 – Schematic of bubble geometry and environment

The models presented here are modified in the next section to account for the inclusion of a nanoparticle loaded shell. Three treatments of the coating are considered:

- Finite thickness viscoelastic solid shell, based on the treatment by Church [182].
- Thin shell approximation, based on the simplification of Church's model by Hoff [137].
- Surfactant monolayer coating, based on the treatment by Glazman [183].

3.2.1. Momentum and Continuity Equations

The momentum of a fluid element is described by the Navier-Stokes equation, written in its general form as:

$$\rho\left(\frac{\partial \mathbf{u}}{\partial t}+\mathbf{u}.\nabla\mathbf{u}\right)=-\nabla p+\nabla.\mathbf{T}+\mathbf{f} \tag{3.1}$$

where **u** is the flow velocity, ρ is the fluid density, p is the pressure, **T** is the deviatoric component of the stress tensor and **f**, assumed to be 0 here, represents body forces (e.g. gravity) acting on the fluid. Assuming the wavelength of the excitation pressure to be much larger than the diameter of a microbubble and thus the radial pressure exerted on it to be uniform, its spherical deformation can be assumed to be radially symmetric. Equation (3.1) will then take the form

$$\begin{aligned}\rho\left(\frac{\partial u_r}{\partial t}+u_r\frac{\partial u_r}{\partial r}\right)&=-\frac{\partial p}{\partial r}+\frac{1}{r^2}\frac{\partial}{\partial r}\left(r^2T_{rr}\right)-\frac{T_{\theta\theta}+T_{\phi\phi}}{r}\\&=-\frac{\partial p}{\partial r}+\frac{\partial T_{rr}}{\partial r}+\frac{2T_{rr}-T_{\theta\theta}-T_{\phi\phi}}{r},\end{aligned} \tag{3.2}$$

where r is the radial distance from the centre of the microbubble, t is time, and subscripts r, θ, and ϕ denote the radial, polar and the azimuthal coordinates in the spherical system respectively. The equation of continuity in spherical coordinates can be written as:

$$\frac{1}{r^2}\frac{\partial r^2u_r}{\partial r}+\frac{1}{r\sin\theta}\frac{\partial\left(u_\theta\right)}{\partial\theta}+\frac{1}{r\sin\theta}\frac{\partial u_\phi}{\partial\phi}=0 \tag{3.3}$$

Due to the assumption of spherical symmetry and the fact that that the bubble is in an infinite domain of incompressible liquid, (3.3) becomes:

$$\frac{1}{r^2}\frac{\partial}{\partial r}\left(r^2u_r\left(r,t\right)\right)=0 \tag{3.4}$$

$$\Rightarrow u_r\left(r,t\right)=\frac{1}{r^2}F\left(t\right) \tag{3.5}$$

where $F(t)$ is a function of time. If there is no mass transport across the boundary at R, the wall velocity will equal to the rate of change in radius and is given by,

$$u_r(R,t) = \frac{dR}{dt} = \frac{1}{R^2} F(t) \Rightarrow F(t) = R^2 \frac{dR}{dt}$$

$$\Rightarrow u_r(r,t) = \left(\frac{R^2 \dot{R}}{r^2} \right), \tag{3.6}$$

Equations (3.2) and (3.6) will form the basis for the subsequent derivation of the equations of motion for microbubbles.

3.2.2. Finite Thickness Coating

In order to describe the motion of a microbubble encapsulated in a coating of finite thickness, equation (3.2) must be integrated across the three domains of the gas core, coating and the surrounding liquid. The density, elasticity and viscosity of the filling gas, however, are assumed to be much smaller than those of the shell and surrounding liquid. The integral term arising from the filling gas (from 0 to R_1) can therefore be eliminated from the derivation. Assuming the shell to be linear elastic, and both it and the surrounding fluid to be isotropic, linear viscous, and incompressible, the deviatoric stress tensor, **T**, is traceless [184,185]. The radial stress tensor component in (3.2) can, therefore, be related to others through $T_{rr} = -\left(T_{\theta\theta} + T_{\phi\phi}\right)$. Substituting (3.6) for u and integrating gives,

$$\begin{aligned} &\rho_s R_1 \ddot{R}_1 \left[1 + \left(\frac{\rho_l - \rho_s}{\rho_s} \right) \frac{R_1}{R_2} \right] + \rho_s \dot{R}_1^2 \left[\frac{3}{2} + \left(\frac{\rho_l - \rho_s}{\rho_s} \right) \left(\frac{4R_2^3 - R_1^3}{2R_2^3} \right) \frac{R_1}{R_2} \right] \\ &= P_s(R_1,t) - P_s(R_2,t) + P_l(R_2,t) - P_\infty(t) \\ &+ T_{s.rr}(R_2,t) - T_{s.rr}(R_1,t) - T_{l.rr}(R_2,t) + 3\int_{R_1}^{R_2} \frac{T_{s,rr}}{r} dr + 3\int_{R_2}^{\infty} \frac{T_{l,rr}}{r} dr, \end{aligned} \tag{3.7}$$

where P_∞, P_S, and P_L are respectively pressures at infinity, the shell, and the surrounding liquid. $P_\infty(t)$ can be described as the sum of the static pressure in the liquid and a time dependent pressure term such as the one generated by an ultrasonic field:

$$P_\infty(t) = P_0 + P_A(t) \tag{3.8}$$

The pressure at the inner and outer bubble surfaces can be derived by considering the stresses acting upon them. The inner surface experiences an outward pressure from

the gas trapped inside and the stresses inside the shell which are counter balanced by the Laplace pressure at that boundary.

$$P_s\left(R_1,t\right)=P_g\left(R\right)+T_{s,rr}\left(R_1,t\right)-\frac{2\sigma_1}{R_1} \tag{3.9}$$

The pressure at the outer surface is made up of the pressure in the liquid and stress within the shell which are counterbalanced by the stresses in the liquid and the Laplace pressure at that boundary.

$$P_s\left(R_2,t\right)=P_l\left(R_2,t\right)+T_{s,rr}\left(R_2,t\right)-T_{l,rr}\left(R_2,t\right)-\frac{2\sigma_2}{R_2} \tag{3.10}$$

For an incompressible and Newtonian fluid, the radial viscous stress, $T_{l,\mathrm{rr}}$, can be written as:

$$T_{l,rr}=2\mu_l\frac{\partial u_{rr}}{\partial r}\Rightarrow 3\int_{R_2}^{\infty}\frac{T_{l,rr}}{r}dr=-4\frac{\mu_l\dot{R}_1^{\,2}}{R_2}. \tag{3.11}$$

Substituting (3.8), (3.9), (3.10) and (3.11) in (3.7) gives:

$$\begin{aligned}&\rho_s R_1\ddot{R}_1\left[1+\left(\frac{\rho_l}{\rho_s}-1\right)\frac{R_1}{R_2}\right]+\rho_s\dot{R}_1^{\,2}\left[\frac{3}{2}+\left(\frac{\rho_l}{\rho_s}-1\right)\left(\frac{4R_2^{\,3}-R_1^{\,3}}{2R_2^{\,3}}\right)\frac{R_1}{R_2}\right]\\&=P_g\left(R\right)-\frac{2\sigma_1}{R_1}-\frac{2\sigma_2}{R_2}-P_0-P_A-4\frac{\mu_l\dot{R}_1^{\,2}}{R_2}+3\int_{R_1}^{R_2}\frac{T_{s,rr}}{r}dr\end{aligned} \tag{3.12}$$

Equation (3.12) forms a general nonlinear dynamic model for a microbubble with finite thickness coating suspended in an incompressible, Newtonian fluid. The radial stress tensor for the shell can be defined according to its characteristics. The elastic stress tensor for a linear elastic solid is given in [184] as

$$T_{s,rr,elastic}=2G_s\varepsilon_{rr}+\lambda_s\left(\varepsilon_{rr}+\varepsilon_{\theta\theta}+\varepsilon_{\phi\phi}\right), \tag{3.13}$$

where λ_s and G_s are Lamé constants [186] and ε_{rr}, $\varepsilon_{\theta\theta}$, and $\varepsilon_{\phi\phi}$ are the principal strain components in the spherical polar coordinate system. The assumption of spherical symmetry reduces the displacement-strain relations [184] to

$$\varepsilon_{rr}=\frac{\partial\varepsilon}{\partial r}\text{ and }\varepsilon_{\theta\theta}=\varepsilon_{\phi\phi}=\frac{\varepsilon}{r}, \tag{3.14}$$

where ε is the displacement in the radial direction and, for small displacements from equilibrium, is given by

$$\varepsilon = \left(\frac{R_1}{r}\right)^2 \left(R_1 - R_{e1}\right). \tag{3.15}$$

R_{e1} is the unstrained equilibrium position of interface 1, which is not necessarily equal to R_{01}. Note that the value of λ_s in (3.13) for an incompressible material is infinity but the second term of (3.13) cancels out with the evaluation of the stress components using (3.14) and (3.15). For small velocity gradients, the viscous stress can be written as [187]

$$T_{s,rr,\text{viscous}} = 2\mu_s \left(\frac{\partial u_r}{\partial r}\right). \tag{3.16}$$

The sum of elastic and viscous stresses in the shell can therefore be written as

$$T_{s,rr} = -4\left(\frac{{R_1}^2}{r^3}\right)\left[G_s\left(R_1 - R_{e1}\right) + \mu_s \dot{R}\right], \tag{3.17}$$

which effectively represents the Kelvin-Voigt constitutive equation given by

$$T_{rr} = 2G_s \varepsilon_{rr} + 2\mu_s \frac{\partial u}{\partial r}. \tag{3.18}$$

The last term on the LHS of (3.12) can be evaluated by integrating (3.17):

$$3\int_{R_1}^{R_2} \frac{T_{rr}}{r}\, dr = -4\left[\frac{{R_2}^3 - {R_1}^3}{{R_2}^3 R_1}\right]\left[G_s\left(R_1 - R_{e1}\right) + \mu_s \dot{R}_1\right]. \tag{3.19}$$

Substitution of (3.19) into (3.12) yields

$$\begin{aligned} &\rho_s R_1 \ddot{R}_1 \left[1 + \left(\frac{\rho_l}{\rho_s} - 1\right)\frac{R_1}{R_2}\right] + \rho_s {\dot{R}_1}^2 \left[\frac{3}{2} + \left(\frac{\rho_l}{\rho_s} - 1\right)\left(\frac{4{R_2}^3 - {R_1}^3}{2{R_2}^3}\right)\frac{R_1}{R_2}\right] \\ &= P_g\left(R\right) - \frac{2\sigma_1}{R_1} - \frac{2\sigma_2}{R_2} - P_0 - P_A - 4\mu_l \frac{\dot{R}_1 {R_1}^2}{{R_2}^3} - 4V_s \mu_s \frac{\dot{R}_1}{R_1 {R_2}^3} - 4\frac{V_s G_s}{{R_2}^3}\left(1 - \frac{R_{e1}}{R_1}\right), \end{aligned} \tag{3.20}$$

where $V_s = {R_{02}}^3 - {R_{01}}^3$. The equilibrium radius R_{e1} can is obtained by applying equilibrium conditions at $t = 0$ to (3.12). Assuming that $p_g = p_0$, $R_1 = R_{01}$, and $\dot{R} = 0$, leads to:

$$-\frac{2\sigma_1}{R_{01}}-\frac{2\sigma_2}{R_{02}}-4G_s\left(R_{01}-R_{e1}\right)\left(\frac{{R_{01}}^3-{R_{02}}^3}{{R_{02}}^3R_{01}}\right)=0$$

$$\Rightarrow R_{e1}=R_{01}+R_{01}\left(\frac{2\sigma_1}{R_{01}}+\frac{2\sigma_2}{R_{02}}\right)\frac{{R_{02}}^3}{{R_{02}}^3-{R_{01}}^3}\frac{1}{4G_S}. \tag{3.21}$$

Equation (3.20) describes the dynamics of a microbubble with a viscoelastic shell, characterised by a shear modulus G_s and viscosity μ_s. Though derived using a consistent theoretical approach, it is appropriate to include a few brief comments on the limitations associated with the dynamic equation as given by (3.20). The present formulation is only valid for small radial oscillations and does not take acoustic and thermal damping into account. In his original paper, Church [182] included *ad hoc* terms for these additional damping mechanisms modified from those given by Prosperetti [136] for free gas bubbles to address this issue. It is worth noting, however, that the contribution from these additional damping mechanisms is negligible for the bubble sizes and insonification regimes studied here. Moreover, the assumption of linear elasticity becomes invalid at large oscillations. This is something that, to the best of author's knowledge, has not been addressed in the literature to date. Alternative models for larger oscillations of encapsulated microbubbles, such as that proposed by Doinikov and Dayton [188], are available, but these are still are only valid for moderate acoustic pressures. The dynamic equation presented in this section will be modified to form the equation of motion for armoured bubbles of finite thickness where the nanoparticles "float" in the shell. That is that their volume fraction in the shell will not change during bubble oscillations.

3.2.3. Thin Shell Approximation

Equation (3.12) is applicable to microbubbles with a finite thickness coating. Most lipid coated contrast agents, however, are considered to have thin shells whose thicknesses are very small compared to the microbubble radius. Assumption of a thin shell, such that its instantaneous thickness, given by

$$d_s = R_2 - R_1, \tag{3.22}$$

is much smaller than the bubble radius, allows Equation (3.12) to be simplified. Using (3.22) to substitute for R_2 in each of the terms in (3.12), then expanding and keeping only linear terms in d_s/R_1 gives:

$$\rho_s R_1 \ddot{R}_1 \left[1+\left(\frac{\rho_l}{\rho_s}-1\right)\frac{R_1}{R_2}\right] \longrightarrow \rho_s R_1 \ddot{R}_1 \left[\frac{\rho_l}{\rho_S} - \frac{d_s}{R_1}\left(\frac{\rho_l}{\rho_s}-1\right)\right] = \rho_l R_1 \ddot{R}_1$$

$$\rho_s \dot{R}_1^{\,2} \left[\frac{3}{2}+\left(\frac{\rho_l}{\rho_s}-1\right)\left(\frac{4R_2^{\,3}-R_1^{\,3}}{2R_2^{\,3}}\right)\frac{R_1}{R_2}\right] \longrightarrow \rho_s \dot{R}_1^{\,2}\left[\frac{3}{2}+\left(\frac{3\rho_l}{2\rho_s}-\frac{3}{2}\right)\right] = \frac{3}{2}\rho_l \dot{R}^2$$

$$\frac{4\mu_L \dot{R}_1 R_1^{\,2}}{R_2^{\,3}} \longrightarrow \frac{4\mu_L \dot{R}_1}{R_1}$$

The inertial term $\ddot{R}_1\delta\left(\rho_l/\rho_s - 1\right)$ can be ignored as it is much smaller than $R_1\ddot{R}_1$ since $d_s \ll R_1$ and the shell density is usually within the same order of magnitude as that of the liquid. Indeed for this term to have any significance, ρ_s must be four or five orders of magnitude larger than ρ_l. Assuming σ_2 to be small compared to σ_1, the surface tension terms become:

$$\frac{2\sigma_1}{R_1}+\frac{2\sigma_2}{R_2} \longrightarrow \frac{2\sigma_1}{R_1}+\frac{2\sigma_2}{R_1}\left(\frac{1}{1+\dfrac{d_s}{R_1}}\right) \approx \frac{2\left(\sigma_1+\sigma_2\right)}{R_1} = \frac{2\sigma}{R_1}.$$

Approximating $V_s = \left(R_{e1}-d_{s0}\right)^3 - R_{e1}^{\,3} \approx 3R_{e1}^{\,2}d_{s0}$, where d_{s0} is the shell thickness at rest, the shell viscosity and elasticity terms in (3.12) can be written as:

$$4V_s\mu_s\frac{\dot{R}_1}{R_1R_2^{\,3}} \approx 12\mu_s\frac{R_{e1}^{\,2}d_{s0}}{R_2^{\,3}}\frac{\dot{R}_1}{R_1} \qquad \text{and} \qquad 4\frac{V_sG_s}{R_2^{\,3}}\left(1-\frac{R_{e1}}{R_1}\right) \approx 12G_s\frac{R_{e1}^{\,2}d_{s0}}{R_2^{\,3}}\left(1-\frac{R_{e1}}{R_1}\right)$$

Applying these to (3.12) and setting $R_1 = R$ gives:

$$R\ddot{R} + \frac{3}{2}\dot{R}^2 = \frac{1}{\rho_l}\left[P_G(R) - \frac{2\sigma}{R} - \frac{4\mu_L \dot{R}}{R} \right] - P_0 - P_A \\ -12\mu_s \frac{{R_0}^2 d_{s0}}{R^3}\frac{\dot{R}}{R} - 12G_s \frac{{R_0}^2 d_{s0}}{R^3}\left(1 - \frac{R_0}{R}\right) \tag{3.23}$$

It is important to note that the last two terms in (3.23) have not been neglected, although they contain the relative shell thickness term d_{s0}/R. A simple way of justifying this is by performing an order of magnitude approximation. Shell thickness and bubble radius are, respectively, in the orders of 10^{-9} and 10^{-6} m. Shell shear modulus and viscosity are considered here to be in the orders of 10^6 Pa and 10^{-1} Pa.s and the acoustic pressures considered here are in the order of 10^5 Pa. It is therefore easy to see that although d_{s0}<<R, the shell viscosity and stiffness terms in (3.23) may become large compared to the other pressures and thus cannot be ignored.

3.2.4. Shell Inclusion via Boundary Conditions

The derivation for the equation of motion of a microbubble coated with a surfactant monolayer (e.g phospholipid) follows the same initial considerations as set out in the previous sections. The main difference here is that the coating is treated as a 2D surface at the outset and its influence up on the bubble dynamics only included via the boundary conditions. Therefore the momentum equation is only integrated from R to ∞:

$$\int_R^\infty \left(r_l \left(\frac{\partial u}{\partial t} + u\frac{\partial u}{\partial r} \right) + \frac{\partial p}{\partial r} - \frac{1}{r^2}\frac{\partial}{\partial r}\left(r^2 T_{rr}\right) + \frac{T_{qq} + T_{ff}}{r} \right) dr = 0 \tag{3.24}$$

Using the same relationship for u given in (3.6):

$$\rho_l \left(R\ddot{R} + \frac{3}{2}\dot{R} \right) + P(\infty) - P_l(R,t) + T_{l,rr}(R,t) + \frac{4\mu_l \dot{R}}{R} = 0 \tag{3.25}$$

Assuming continuity of stress at the microbubble surface gives the boundary condition,

$$P_l(r = R,t) = P_g(R) - \frac{4\kappa_s \dot{R}}{R^2} - \frac{2\sigma}{R} - T_{l,rr}(R,t), \tag{3.26}$$

where κ_S is the dilatational viscosity [189] of the shell. Substituting (3.26) into (3.25) gives a general equation of motion for a coated microbubble:

$$\rho_l\left(R\ddot{R}+\frac{3}{2}\dot{R}\right)=P_g\left(R\right)-P\left(\infty\right)-\frac{2\sigma}{R}-\frac{4\mu_l\dot{R}}{R}-\frac{4\kappa_s\dot{R}}{R^2}. \tag{3.27}$$

The elastic and viscous properties of monolayer and bulk solutions of lipids and surfactants are highly dependent on the surface molecular concentration and shear rate. This has been demonstrated experimentally using Langmuir isotherm and captive bubble methods [190] and theoretically through molecular dynamic simulations [191]. The surface properties of a bubble with such an encapsulation will thus vary as it oscillates.

The effect of a radius dependent interfacial tension in contrast agents has been considered by various authors. Marmottant *et al.* [144] formulated a surface area dependant dynamic surface tension model. It was implemented via an *ad hoc* law in which the behaviour of the coating was partitioned in three regimes, given by

$$\sigma\left(R\right)=\begin{cases}0, R\le R_{\mathrm{x}}\\ \chi\left(\dfrac{R^2}{{R_x}^2}-1\right), R_{\mathrm{x}}\le R\le R_{\mathrm{rupt}}\\ \sigma_{0,}\ R\ge R_{\mathrm{rupt}}\end{cases}, \tag{3.28}$$

where R_{x} and R_{rupt} respectively denote the buckling and rupture radius, and χ is the elastic compression modulus.

A model in which both interfacial tension and viscosity are functions of the surface molecular concentration, Γ, was proposed by Stride [147]. In this treatment, the effects of initial surface concentration Γ_0 and the characteristics of the given surfactant, represented by a constant K, are separated to allow for variations in bubble behaviour due to different levels of adsorption. Both interfacial tension and viscosity are also treated as continuous functions obeying a power law and exponential relationship in accordance with reported experimental observations:

$$\sigma\left(R\right)=\int -2\Gamma_0\frac{\partial\sigma}{\partial\Gamma}\frac{{R_0}^2}{R^3}dR=\sigma_0+\frac{K{\Gamma_0}^{x+1}}{\left(x+1\right)}\left(1-\left(\frac{R_0}{R}\right)^{2\left(x+1\right)}\right) \tag{3.29}$$

$$\kappa_S = \kappa_{S0} \exp\left(\frac{ZR_x{}^2}{\left(R^2 - R_x{}^2\right)} \right) \tag{3.30}$$

In (3.29) Γ_0 is the initial surfactant concentration, K and x are surfactant dependant constants. In (3.30) κ_{S0} is the initial dilatational viscosity of the shell, R_x is the buckling radius and Z is a parameter whose value depends on the surfactant used. Equations (3.29) and (3.30) are then substituted into (3.12) and (3.26) for their respective parameters. More information about these and related models can be found in Section 2.5.2.

This approach was included here to provide some context to the work previously done on armoured microbubble dynamics, presented in sections 3.3.2. and 3.3.3. The equations of motion presented in sections 3.2.2 and 3.2.3 are, however, capable of presenting a wider variety of shell configurations. In fact, given appropriate parameter values, equation (3.23) can be made to closely resemble the behaviour of (3.27). Thus the approach presented here was not adopted for final results.

3.3. Effective Properties of Nanoparticle Laden Shell

3.3.1. Effective Viscosity

It has been known for some time now that the rheological properties exhibited by colloidal suspensions differ from those of a pure liquid. This is due to disruption of flow caused by the dispersed nanoparticles through convective and/or hydrodynamic effects. The problem was first considered by Einstein [192] for isotropic suspensions of rigid spherical particles in Newtonian fluids, so dilute that each particle could be treated as suspended in an infinite liquid. The effect was described through an effective viscosity, μ_{eff}, given by

$$\mu_{eff} = \mu_0 \left(1 + 2.5\Phi\right), \tag{3.31}$$

where Φ is the volume fraction of particles and μ_0 is the dynamic viscosity of the bulk liquid. Outside the small range of $\Phi<0.02$ the effect of hydrodynamic interactions and Brownian motion becomes important and the first order relation described (3.31) does not suffice. Several authors have considered hydrodynamic interactions between particle pairs by evaluating μ_{eff} to second order [193-195]. Beenakker [196] extended the formulation for many-body hydrodynamic interactions suitable for higher concentrations. The model used here to describe the effective viscosity of the particulate shell comes from the work of Cohen *et al.* [197]. They derived models for effective Newtonian viscosity as a function of concentration, and full viscoelastic behaviour as a function of concentration and frequency for neutral, mono-disperse colloidal suspensions with moderate concentrations. They found that contributions due to particle diffusion take place on a much longer timescale in comparison to those as the result of particle-particle interactions, and found good agreements between their results and experiments of van der Werff *et al.* [198]. Bulk effective viscosity for high frequency perturbations is therefore given by

$$\mu_{eff} = \mu_0 \left(1 + 2.5\Phi + 4.59\Phi^2 + O(\Phi^3)\right). \tag{3.32}$$

Cohen *et al.* did not put an upper frequency limit on their model andthe accuracy of this claim is subject to further investigation. In the absence of conclusive experimental results and for sake of simplicity, this factor is not taken into account in the current study. In addition, the viscosity of the coating material, μ_s, is likely to be

frequency dependant [137]. Again, and for the sake of simplicity, it is assumed to be constant within the range of frequencies commonly employed in ultrasound diagnostic imaging (1-8MHz) following Hoff [137].

Defining an effective viscosity for a nanoparticle laden thin shell presents a number of challenges. First order models for both the shear and dilatational viscosities of particle laden interfaces have been developed by Lishchuk & Halliday [199]. These are strictly valid for low particle concentrations (≤ 0.15) and small Reynolds numbers. In the absence of suitable experimental data, and for sake of simplicity, however it is assumed that a model for the effective viscosity for a thin shell to take the same form as (3.32), with Φ replaced by a radius dependant nanoparticle concentration as defined by (3.37).

3.3.2. Effective Resistance to Compression

The influence of surface deposited nanoparticles upon microbubble oscillation was examined theoretically and experimentally by Stride *et al.* [12]. In this treatment, the shell's compressive resistance is increased when the bubble is compressed beyond a threshold, where jamming is expected to occur. The dynamic behaviour was described through a modified version of equation (3.27) with radius dependant terms described by equations (3.29) and (3.30) resulting in,

$$\begin{aligned}\rho_L\left(R\ddot{R}+\frac{3}{2}\dot{R}\right)&=\left(P_0+\frac{2\sigma_0}{R_0}\right)\left(\frac{R_0}{R}\right)^3-P_0+P_A-\frac{4\mu_l\dot{R}}{R}\\&-\frac{2}{R}\left(\sigma_0+\frac{KX(R)\Gamma_0{}^{x_s+1}}{(x_s+1)}\left(1-\left(\frac{R_0}{R}\right)^{2(x_s+1)}\right)\right)-\frac{4\dot{R}}{R^2}\left(\kappa_{S0}\exp\left(\frac{ZR_x{}^2}{\left(R^2-R_x{}^2\right)}\right)\right),\end{aligned} \tag{3.33}$$

where $X(R)$ is a multiplier term which accounts for the enhancement of compressive resistance as is defined as

$$\mathrm{X}(R)=\begin{cases}1, R>R_{lim}=2R_0\sqrt{f_p/\pi}\\ X_{\max}, R\leq R_{lim}\end{cases}, \tag{3.34}$$

where R_{lim} is the limiting radius below which microbubble resistance to further compression is multiplied by a factor $X_{\max}$, and f_{p} is the maximum fractional area covered by the particles relative to their square packing density. Square packing

here, as illustrated in **Figure 3.2**, refers to a formation of spheres (or circles in 2D) in a square grid on a rectangular surface.

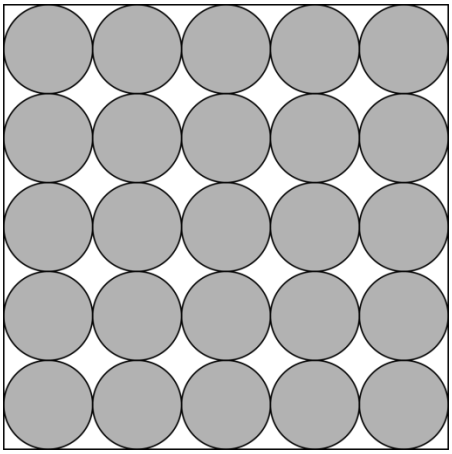

Figure 3.2 – Square packing arrangement of complete circles in a square. The total fractional area covered by the circles in this arrangement is 0.7854.

The surface coverage for this arrangement can be calculated by dividing the total area of the circles by the area of the rectangle. Assuming that the circles are uniform and arranged as in **Figure 3.2**, the maximum fractional area covered is $\pi/4$ (0.7854). The value of X_{max} depends on the behaviour of the nanoparticles upon packing, with larger values representing higher resistance. This model, as shown in [12], is effective in predicting expansion dominant bubble oscillations. Upon further scrutiny, however, a number of limitations arise which are addressed in the next section.

3.3.3. Improving Compressive Resistance Model

A model for the enhancement of the shell's compressive resistance due to the presence of nanoparticles was presented Section 3.3.2. Although Equation (3.33) can be used to illustrate the ability of an armoured coating to increase the asymmetry of bubble oscillations, the formulation of the multiplier term $X(R)$ as defined in (3.34) has some limitations. These are discussed in greater detail in this section, followed by formulating and evaluating an improved expression for $X(R)$. For simplicity, it is assumed that the particles remain attached to the surface regardless of the magnitude of the driving forces and $R_{lim}<R_0$. This means, for a given bubble, that the total surface area covered by the particles and thus the value of R_{lim} remain constant throughout the oscillations.

The expression for R_{lim} is derived for the square packing arrangement and the maximum value of f_p in (3.34) is therefore limited to $\pi/4$. Higher values of f_p result in the physically inaccurate condition $R_{lim}>R_0$. Explicit specification of the initial fractional surface coverage is also not possible. In order to further study its effectiveness in terms of expected trends, Equation (3.33), with $X(R)$ defined by (3.34), was solved numerically using the procedure outlined in 3.4.1. The change in expansion to contraction (asymmetry) ratio with the effective stiffness was of interest here which is given by,

$$\frac{+\Delta R}{-\Delta R} = \frac{R_{max} - R_0}{R_0 - R_{min}}, \tag{3.35}$$

where R_{max} and R_{min} denote maximum and minimum radius values; ΔR is the change in a microbubble's radius from its initial value, and the symbols '+' and '−' respectively indicate expansion and contraction.

Simulations were carried out for bubbles with X_{max} values ranging from 8 to 100. The sound field was modelled as a 10 cycle, 1.0 MHz sinusoidal wave of with peak pressures of 100, 250, and 500 kPa. The other parameters were set as follows: ρ_L = 1000 kgm^{-3}; R_0 = 4.0 μm, p_0 = 1×10^5 Pa, σ_0 = 0.05 Nm^{-1}, Γ_0 = 2.25×10^7 m^{-2}, x_s = 0, K = 1.5×10^{-14} Nm; μ_L = 0.15 mPa.s; κ_{s0} = 1.5×10^{-4} Nsm^{-1}; $R_x = 0.8R_0$; B = 0; f_p = 0.7853; $R_{lim} = 2R_0(f_p/\pi)^{0.5} = 0.99R_0$.

Figure 3.3 depicts the overall asymmetry ratios as well as the maximum and minimum radii reached at each excitation pressure against the variation in X_{max}. An increase in asymmetry with increasing X_{max} is clearly observed in Figure 3.3a. There are, however, some discrepancies in these results which warrant further investigation.

The inconsistency in the results shown in Figure 3.3a is most visible at the highest excitation pressure where asymmetry tends to be lower compared to the other cases. The reason for this is illustrated in Figure 3.3b, in which the expansion and contraction components of each case are separately considered. Coatings with higher values of X_{max} represent greater resistance to compression. For a given incident wave, therefore, increase in X_{max} must result in lower compression. This is, however, not evident for the 500 kPa case in Figure 3.3b where the results seem to show a sudden increase in compression at higher values of X_{max} >25. This is a result of the

discontinuous formulation in (3.34), where the influence of the nanoparticles only comes into effect once $R<R_{lim}$. The formulation of the elasticity term in (3.33) is such that its sign changes once $R<R_0$ and thus acts against compressive forces until the condition $R>R_0$ is restored. The value $X(R)$ also remains equal to X_{max} while $R<R_{lim}$ even as the bubble is expanding. This means that, for a short period of time, the particles are contributing positively to bubble wall acceleration.

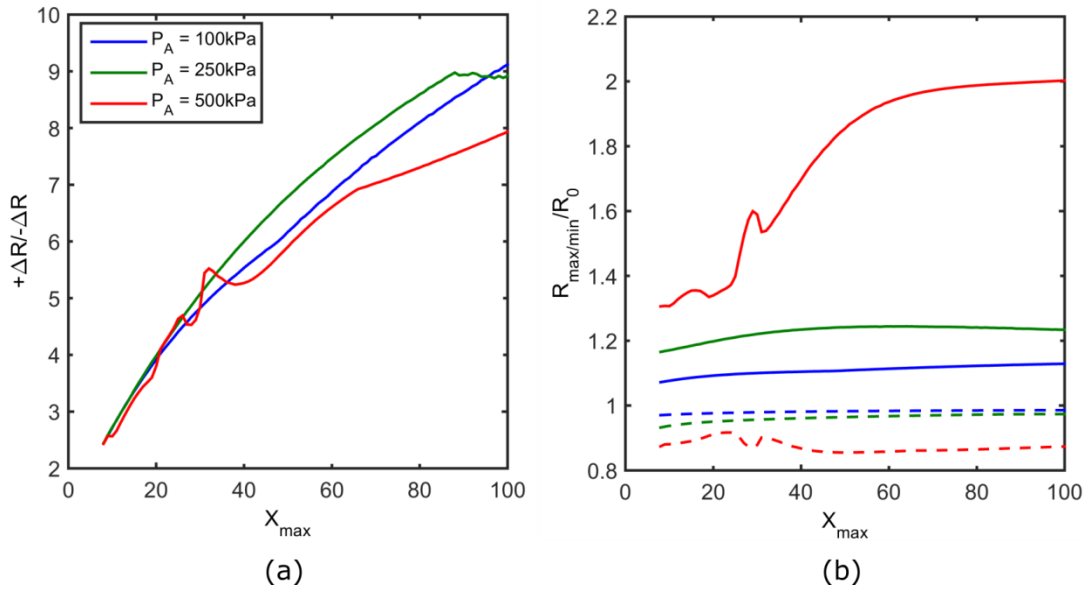

Figure 3.3 – a) Predicted asymmetry against particle resistance, X_{max}, for a microbubble calculated using **(3.33)**, with $X(R)$ defined by **(3.34)**, at various excitation pressures. b) R_{max}/R_0 (solid) and R_{min}/R_0 (dashed) components of asymmetry corresponding to the results shown in (a) against increased particle resistance. In all cases: f_p=0.7853 Red = 500kPa; Green 250 kPa, Blue= 100 kPa.

To address the issues discussed above, compressional resistance can be modelled as an exponential function of instantaneous to maximum fractional surface coverage, given by

$$X(R) = \alpha^{\left[\frac{\phi}{\phi_{max}}\right]^{\beta}}, \tag{3.36}$$

where α and β are determined by the properties of the lipid/solid and solid/solid interactions and ϕ and ϕ_{max} are respectively the instantaneous and maximum fractional surface area covered by particles. ϕ is given by

$$\phi = \phi_0 \left(\frac{R_0}{R}\right)^2, \tag{3.37}$$

where ϕ_0 is the value of ϕ when $R = R_0$. The value of (3.36) is capped at X_{max} to reflect the variations between coating structures and the limit to which they can withstand compression.

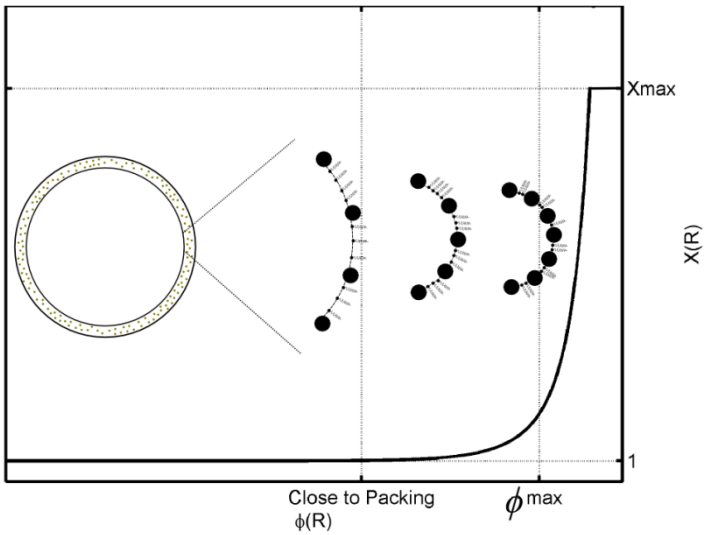

Figure 3.4 The improved compressional resistance model.

The area between the particles at the interface is assumed to be occupied by an initial concentration of lipid molecules. As the radius of this interface decreases, a higher proportion of its area will be occupied by the particles and the concentration of the lipid molecules will also increase, which enhances the effective compressional resistance of that interface. This treatment results in a new equation for the radius at jamming, R_p, given by

$$R_p = \sqrt{\frac{\phi_0}{\phi_{\max}}} R_0. \tag{3.38}$$

The effectiveness of the new compressional resistance model can be demonstrated by replacing $X(R)$ in (3.33) with (3.36) and applying the same protocol and parameter values as before to attain asymmetry ratios against X_{max} at various excitation pressure. The values of ϕ_0 and ϕ_{max} were set to 0.7853 to replicate the same jamming condition as that used to produce the results in Figure 3.3. The results are shown in Figure 3.5. As may be seen, the anomalous features of the curves in Figure 3.3 are no longer present.

In contrast to the previous case, increases in X_{max} (as shown in Figure 3.5b) are now correctly accompanied by decreases in compression regardless of excitation pressure

and higher acoustic pressure amplitudes give rise to increased asymmetry. The results in Figure 3.5a in general show less asymmetry than those in Figure 3.3a. This is due to the lower amplitudes of expansion shown in Figure 3.5b, where unlike the results in Figure 3.3b, $X(R)$ drops rapidly upon expansion and does not contribute to the growth of the bubble.

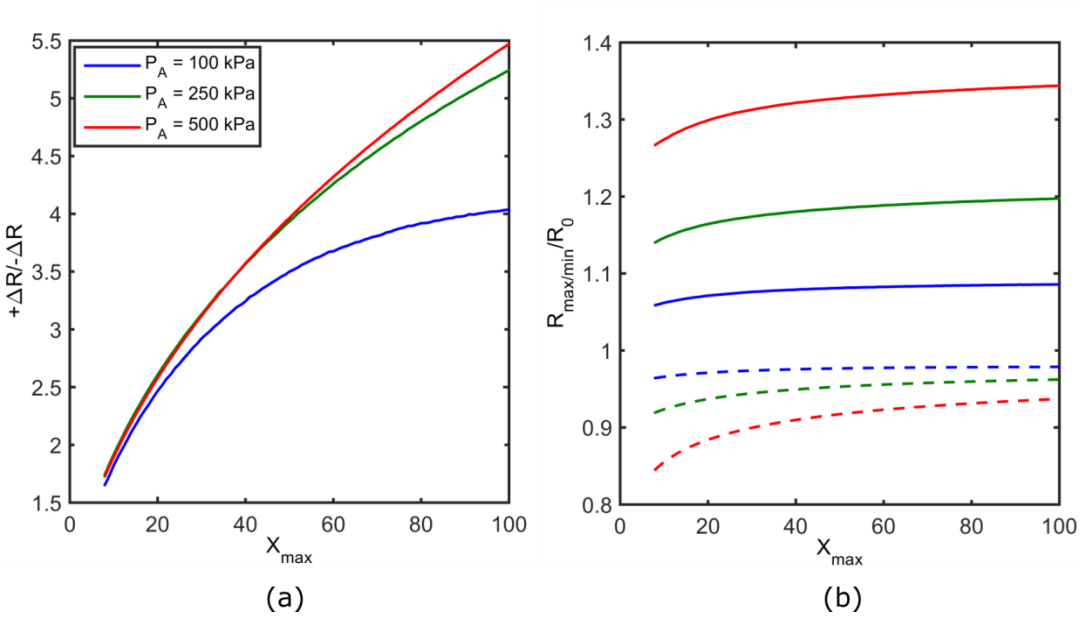

Figure 3.5 a) Predicted asymmetry against particle resistance, X_{max}, for a microbubble calculated using **(3.33)**, with $X(R)$ defined by **(3.36)**, at various excitation pressures. b) R_{max}/R_0 (solid) and R_{min}/R_0 (dashed) components of asymmetry corresponding to the results shown in (a) against increased particle resistance. In all cases: ϕ_0=0.7853 Red = 500kPa; Green 250 kPa, Blue= 100 kPa.

The finite thickness and thin shelled models presented in 3.2.2 and 3.2.3 can be similarly modified to include the influence of embedded nanoparticles. The influence of nanoparticles upon bubble response is modelled in the next section by replacing the constant values of shear modulus and viscosity with the radius dependent functions discussed in this section.

3.4. Results and Discussion

In this section, the response of an armoured microbubble to ultrasound is investigated. Equations (3.20) and (3.23) are employed to describe the radial motion of bubbles with either finite thickness or thin coatings. The influence of nanoparticles is accounted for by replacing the values of shear modulus and viscosity in both equations with functions describing their effective values. The effective shear modulus is given by

$$G_s(R) = G_{s0} X(R), \tag{3.39}$$

where G_{s0} is the shear modules of the shell with no particles present and $X(R)$ is given by (3.36). The effective viscosity of the finite thickness shell is given by

$$\mu_s = \mu_{s0}\left(1 + 2.5\phi_0 + 4.59\phi_0^{\,2}\right), \tag{3.40}$$

where μ_{s0} denotes the viscosity of the shell with no nanoparticles present and Φ is the concentration of the particles in the shell. The effective viscosity of the thin shell is given by

$$\mu_s(R) = \mu_{s0}\left(1 + 2.5\phi(R) + 4.59\phi(R)^2\right), \tag{3.41}$$

where ϕ(R) is the radius dependent particle concentration as given in (3.37).

3.4.1. Simulation Method and Parameter Selection

The modified versions of equations (3.20) and (3.23) were solved numerically in MATLAB® 2012b (MathWorks Inc.) using the native 4th and 5th order Runge-Kutta function ODE45. The parameters were non-dimensionalised using the scheme:

$$[\text{mass}] = \left[\frac{p_0 R_0}{(2\pi f)^2}\right],\ [\text{time}] = \left[\frac{1}{2\pi f}\right],\ [\text{length}] = [R_0],$$

to avoid numerical errors caused by rounding of small numbers. The theoretical results in this section were obtained for the case of Nitrogen-filled bubbles in water. The values of the parameters used in the simulations are given in Table 1. The values of those parameters for which a range has been given are further specified for individual set of results. In addition, the influence of surface tension was assumed to be reduced by the coating, and was therefore neglected in the present study.

Parameter	Value	Unit	Parameter	Value	Unit
R_0	4.0×10^{-6}	[m]	ρ_s	19000	[kgm^{-3}]
ρ_l	1000.0	[kgm^{-3}]	μ_{s0}	0.1-1.77	[Pa.s]
μ_l	1.002×10^{-3}	[Pa.s]	G_{s0}	15-88.8	[MPa]
κ	1.0	-	d_{s0}	4-25	[nm]
p_0	1.0×10^{5}	[Pa]	ϕ_0	0.55-0.82	-
p_A	50-600	[kPa]	ϕ_{max}	0.82	-
f	0.2-5.0	[MHz]	α	2	-
			β	30	-
			X_{max}	2.0-800	-

Table 1 – List of parameters and values used in bubble response simulations

In the literature equations of this type have been widely applied to describe oscillations of arbitrary amplitude. Strictly speaking, however, the equations derived in this chapter are only valid for small oscillations ($<0.1R_0$). For the purposes of this study, therefore, when larger pressure values are used, the insonation frequency is shifted to an off-resonance value to limit the excitation amplitude.

3.4.2. Radial Oscillations and Scattered Pressure

A comparison of radial oscillations alongside the corresponding scattered pressure and its frequency content for nanoparticle coated and surfactant only microbubbles is demonstrated in Figure 3.6. The radius time curves were calculated using the modified version of equation (3.23) and the method described above. The incident field was modelled as a 10 cycle Gaussian pulse of 2.0 MHz and peak pressure of 100.0 kPa. The scattered pressure values were calculated using equation (2.18) and analyzed in the frequency domain using the MATLAB function `fft.m`. The increase in asymmetry of oscillations can be clearly seen in the radius time curve (Figure 3.6a) in case of the armoured microbubble. The sudden increase in coating stiffness causes an abrupt change in wall acceleration which appears as sharp peaks in the scattered pressure as shown in Figure 3.6b. This is reflected in the enhanced harmonics in the frequency spectrum as shown in Figure 3.6c.

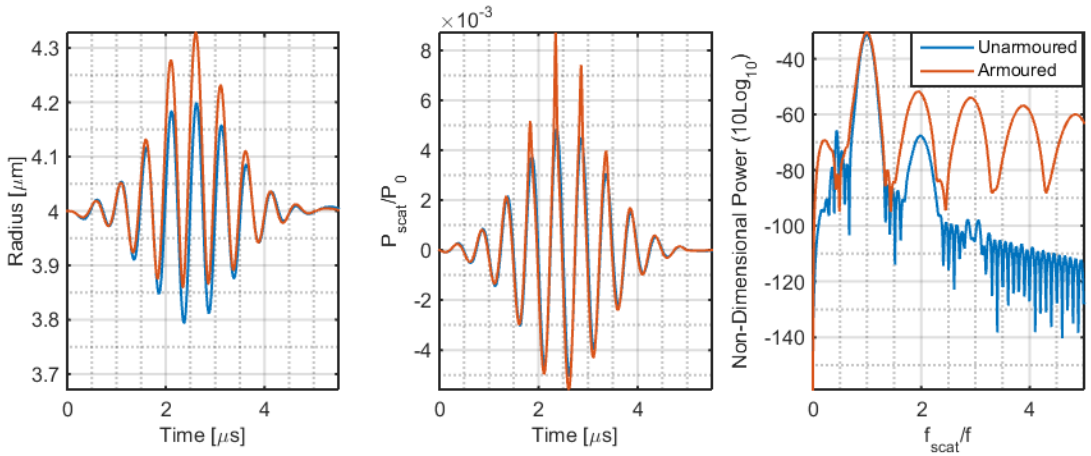

(a) (b) (c)

Figure 3.6 – Comparison between armoured (red) and unarmoured (blue) microbubbles using thin shell the thin shell model with parameters: d_{s0}=4.0 nm, μ_{s0}=0.5 Pa.s, G_{s0}=15.0 MPa, f=2.0 MHz, p_A=100.0 kPa, ϕ_0=0.8, X_{max}=80.0.

The effect of X_{max} upon bubble response is expected to be similar in trend to that shown in Figure 3.5, where increase in X_{max} is accompanied by higher asymmetry. It is appropriate to illustrate this by simulating radius-time curves as well as the frequency content of the scattered signal for a few cases of armouring arrangement. The results, as displayed in Figure 3.7, show the responses of bubbles with X_{max}= 2.0, 8.0, and 80.0. The jamming radius, which is the same for all cases, has been indicated in Figure 3.8a.

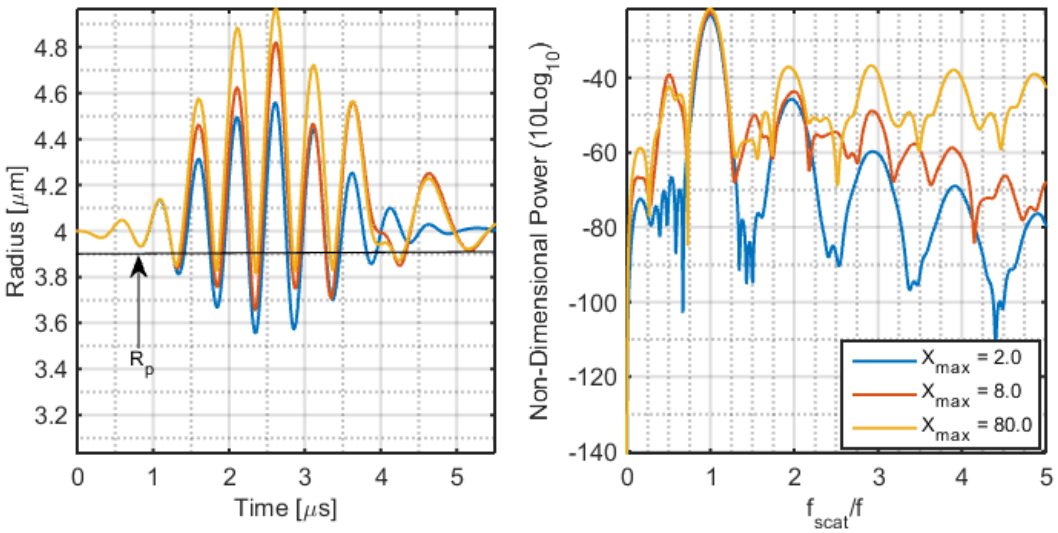

(a) (b)

Figure 3.7 – Comparison between responses of bubbles with various compressional resistances using thin shell the thin shell model with parameters: d_{s0}=4.0 nm, μ_{s0}=0.5 Pa.s, G_{s0}=15.0 MPa, f=2.0 MHz, p_A=250.0 kPa, ϕ_0=0.8, X_{max}=80.0.

It can be seen from the results here that the increase in compressional resistance brings the minimum radius closer to the jamming radius. This, combined with the increase in maximum radius, increases oscillational asymmetry which in turn enhances the nonlinear response of the microbubbles. In addition, as in Figure 3.5, the difference between the maximum radii diminishes with the increase in X_{max}. The effect of variation of shell parameters upon bubble response will be investigated in more detail in the following sections of this chapter.

3.4.3. Resonance Frequency

The increased nonlinearity of the bubble oscillations means that analytical formulas for resonance frequency no longer provide useful information about its behaviour. The effect of shell composition and armouring upon the frequency response of a bubble was therefore investigated numerically by solving (3.23), with effective shear modulus and viscosity defined by (3.39) and (3.41), at different excitation frequencies and recording the maximum bubble radius in each simulation. The shell thickness was set to 4.0 nm. Two sets of shell compositions with shear viscosities μ_{s0} = 0.5 and 1.77 Pa.s and shear modulus of G_{s0} = 15.0 and 88.8 MPa were considered. The shell properties of phospholipid coated contrast agents are reported to be closer to the first set of values [74]. The latter of the two sets, corresponding to albumin coated contrast agents, was included to provide an order of magnitude comparison.

The initial particle concentration was set to ϕ_0 = 0.0 for bubbles with no nanoparticles and ϕ_0 = 0.72 for armoured bubbles. The value of X_{max} was set to 80.0 for all armoured bubbles. In order to provide another point of comparison, a case of an uncoated or "clean" bubble was also considered by setting G_{s0} and μ_{s0} to 0. The incident field was modeled as an ultrasound burst of 10 cycles, modulated by a Gaussian window. The peak excitation pressure was set to 50 kPa for all coated bubbles and 25 kPa for the uncoated case. This was to avoid bubble expansions above $2R_0$ as this would correspond to inertial cavitation, i.e. violent collapse and fragmentation of the bubble [160]. Values for the other parameters not mentioned here are given in Table 1.

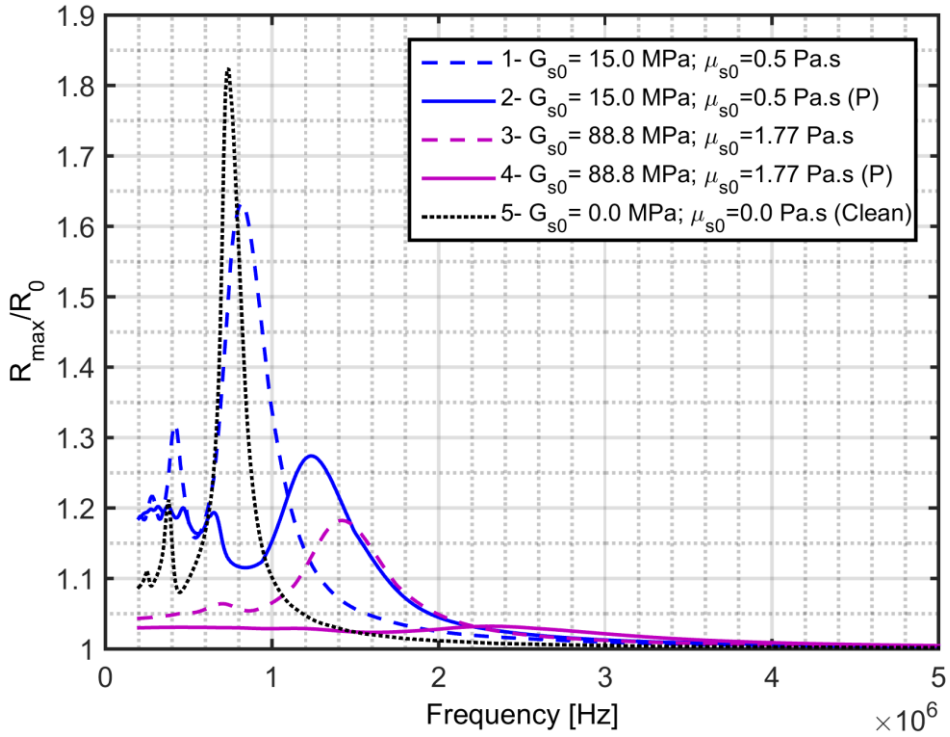

Figure 3.8 The effect of various coating composition and armouring on the maximum response of a bubble of initial radius of 4.0 µm to ultrasonic pulses of varying frequencies as predicted by the modified version of Equation (3.23). The peak frequency response in each case occurs at: 1 - 0.82 MHz; 2 - 1.24 MHz; 3 - 1.42 MHz; 4 - 2.3 MHz; 5 - 0.74 MHz. Viscoelastic properties of the coatings for each case have been given in the legend. The presence of particles in the shell is indicated by letter (P) with parameters: ϕ_0=0.72, ϕ_{max} = 0.82, and X_{max}= 80.0.

A comparison of the frequency response for all cases is given in Figure 3.8. As demonstrated, the frequency at which the maximum response occurs, as well as its amplitude, is strongly affected by the composition of the shell. For unarmoured bubbles (cases 1 and 3) the results show the previously reported trend of higher resonance frequencies for coatings with higher shear moduli [182,200]. Furthermore,

as shell viscosity increases, the resonance peaks broaden. The inclusion of nanoparticles (cases 2 and 4), results in an additional increase in the respective resonance frequencies as well as considerable reduction in maximum response and further broadening of the resonance peak.

The results in Figure 3.8 show the combined effect of modified stiffness and viscosity. In order to investigate the influence of each property upon the frequency response in isolation, an armoured bubble with the properties: d_{s0} = 4.0 nm, μ_{s0} = 0.5 Pa.s, G_{s0} = 15.0 MPa, ϕ_0=0.80, ϕ_{max} = 0.82, and X_{max}= 8.0 was defined as the standard case. Other parameters were set according to the values given in Table 1. Variation in effective stiffness was then simulated by increasing X_{max} and constant μ_{s0}. The dynamic equation and simulation protocol were same as those used to produce Figure 3.8.

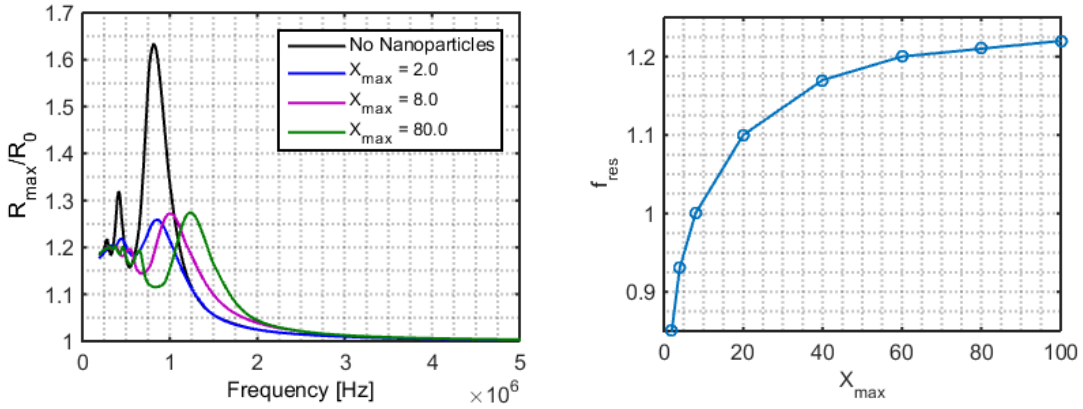

(a) (b)

Figure 3.9 a) Comparison of frequency responses to a 10 cycle pulse of P_A=50 kPa for armoured bubbles with shell parameters: d_{s0} = 4.0 nm, μ_{s0} = 0.5 Pa.s, G_{s0} = 15.0 MPa, ϕ_0=0.80, ϕ_{max} = 0.82, and varying compressional resistances. The frequency response of the unarmoured bubble (ϕ_0=0.0) has been included to provide a point of reference. b) The increase in resonance frequency of armoured bubbles with same parameters as in (a) against various X_{max}.

Figure 3.9a compares the frequency responses of bubbles with different values of X_{max}. The results show an increase in resonance frequency with the increase in effective shell rigidity brought about by higher compressional resistance. This trend is shown more clearly in Figure 3.9b where peak response frequency is plotted against values of X_{max}. Apart from the shift in resonance frequency, two other observations can be made. As X_{max} is increased, a slight increase in the maximum radial response may be observed. Another significant observation here is that the rate at which the resonance frequency increases gets smaller at higher X_{max} values. This

trend is explained by referring back to the results in Figure 3.5b where, for a given excitation pressure, the rate of change in maximum radial amplitude decays with increasing compressional resistance. This is as a result of a balance between the excitation pressure and the compressional resistance, where the multiplier term $X(R)$ does not reach its X_{max} value, thus rendering the value of the latter irrelevant to the response.

The effect of shell viscosity was investigated by decreasing μ_{s0} for the same initial surface concentration of nanoparticles and X_{max}. The results, as displayed in Figure 3.10, show reduced and wider resonance peak at higher viscosities. Viscous damping can have quite significant effects upon asymmetry of the response. This will be investigated further later in this chapter.

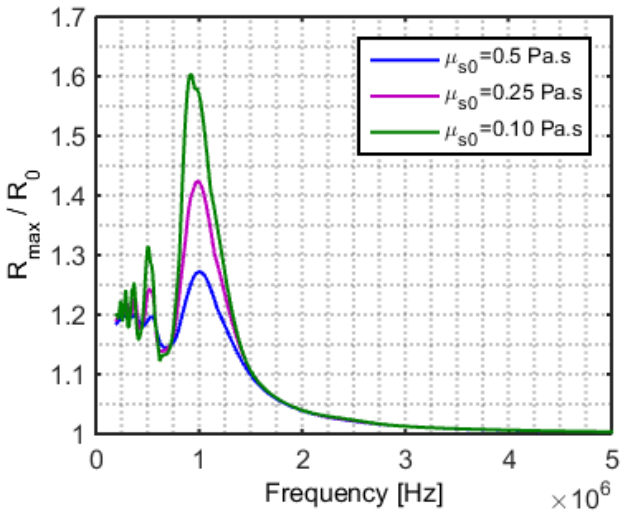

Figure 3.10 Comparison of frequency responses to a 10 cycle pulse of P_A=50 kPa for armoured bubbles with shell parameters: d_{s0} = 4.0 nm, G_{s0} = 15.0 MPa, ϕ_0=0.80, ϕ_{max} = 0.82, X_{max} = 8.0, and varying shell viscosity, μ_{s0}.

3.4.4. Nanoparticle Concentration and Asymmetric Oscillations

The frequency response of an armoured microbubble, as demonstrated in 3.4.3, is highly dependent on the degree to which the nanoparticles embedded in the shell modify its effective stiffness. This is partly determined by the parameter X_{max}, whose influence on resonance frequency and asymmetry of oscillations was investigated in the previous sections. In this section, the role of particle concentration and its effect on bubble behaviour is investigated.

It was shown in 3.3.3 that an increase in asymmetry is primarily caused by increased shell stiffness, which takes place when the particles jam. This is illustrated in Figure

3.11, where three thin shelled bubbles with various initial particle concentrations (ϕ_0) are subjected to 10 cycle, 2.0 MHz pulses of increasing peak excitation pressure. The dashed lines in both graphs denote the jamming radius (R_p) for each case. The results show mildly compression dominated oscillations at lower pressure amplitudes. As the excitation pressure increases, microbubbles are compressed further towards their respective jamming radii, after which their oscillations become increasingly expansion dominated.

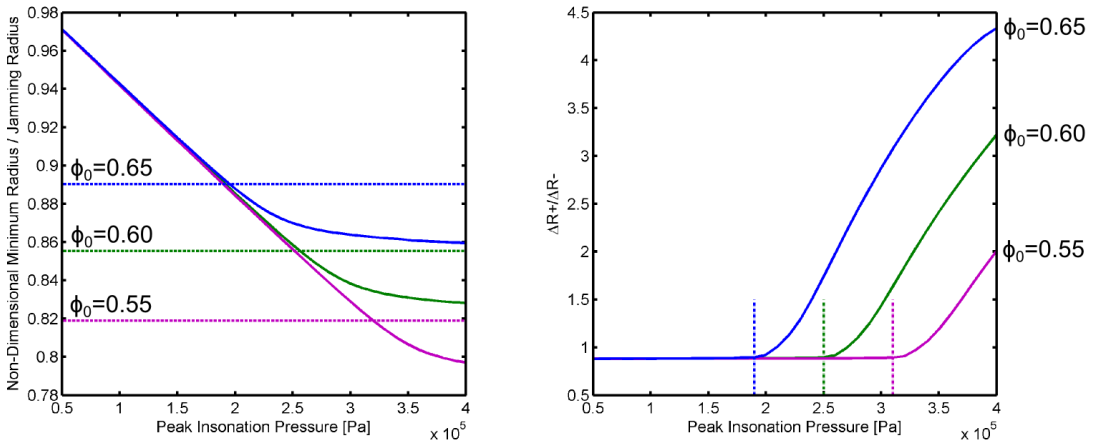

Figure 3.11 Effect of particle concentration on bubble behaviour. Shell parameters: d_{s0} = 4.0 nm, μ_{s0} = 0.5 Pa.s, G_{s0} = 15.0 MPa, and X_{max}= 8000.0 a) Minimum (solid) and jamming (dashed) radii against peak insonation pressure for various ϕ_0. b) Corresponding asymmetry ratio (solid) and the insonation pressure after which $R_{min}<R_p$ (dash-dot).

Perhaps the most obvious observation here is that increasing ϕ_0 leads to higher asymmetry at lower insonation pressures by bringing R_p closer to R_0. While this is true for the cases studied in Figure 3.11, it is important to note that viscoelastic properties of the shell can also influence the operational conditions necessary for the particles to jam. For a given value of ϕ_0, bubbles with stiffer shells may, for example, require exposure to pulses of higher pressure and/or frequency to reach their R_p.

The value of ϕ_0, aside from determining where jamming occurs, does not have any other impact on the effective shell stiffness. The shell viscosity, on the other hand, is continually modified by the presence of particles. It is therefore interesting to see how ϕ_0 affects the asymmetry of oscillations, particularly for cases of low ϕ_0 where it is more difficult for the particles to jam. Two shell viscosities of μ_{s0} = 0.25 and 0.5 Pa.s were examined. The coating thickness was set at 15.0nm. Bubble dynamics were simulated using (3.20) with the effective viscosity described using (3.40), and thus the dependence of viscosity upon surface concentration during oscillations was

removed. The shear modulus of the coating for both cases was kept the same at G_{s0}=15.0 MPa to minimise the dependence of the bubble response upon insonation frequency. The incident field was modelled as a 10 cycle, 1.1 MHz pulse with peak pressure of 100.0 kPa. Note that the thicker coating used here increases the resonance frequency for both cases to approximately 2.6 MHz (using Hoff's approximation in [137]), and thus the bubbles are not excited at resonance.

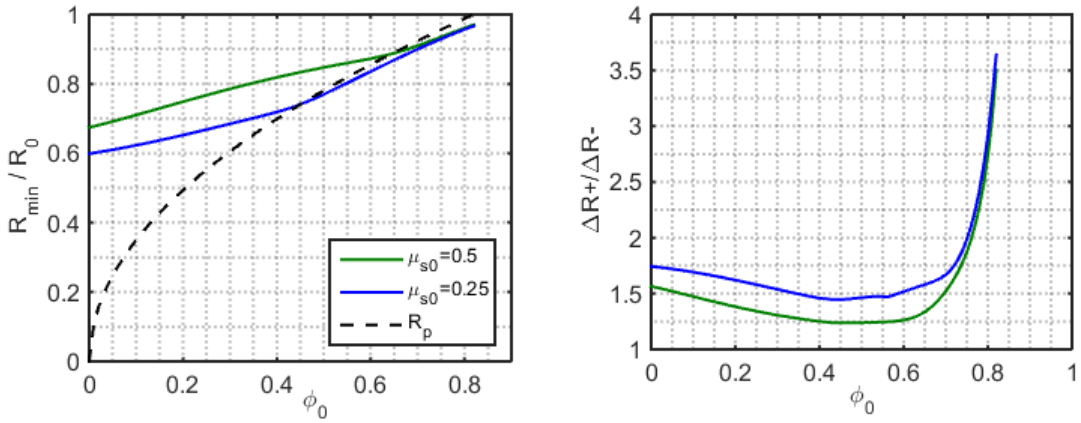

Figure 3.12 - Minimum radius and jamming radius against initial concentration of nanoparticles for various coating viscosities. G_{s0}=15.0 MPa, p_A=100kPa

The results are demonstrated in Figure 3.12, where both cases exhibit similar trends. In Figure 3.12a, the black dashed line denotes the value of R_p as given by (3.38). Of particular interest are the results in the regions of ϕ_0<0.45 for μ_{s0} = 0.25 Pa.s, and ϕ_0<0.6 for μ_{s0} = 0.5 Pa.s, where, R_{min} is still larger than R_p and jamming has not occurred. As shown in Figure 3.12a, higher particle concentration in the shell leads to an increase in minimum radius. In both cases, however, Figure 3.12b shows the asymmetry to be decreasing prior to jamming. From the dip in the asymmetry data, furthermore, it can be concluded that the rate at which the maximum radius decreases is higher within this region relative to that of the increase in minimum radius. This continues until the R_{min} in each case passes the R_p threshold, after which jamming occurs and a significant increase in asymmetry, as shown in Figure 3.11, is visible.

This section focused on the effect of nanoparticle concentration in the coating on the bubbles exhibited asymmetry. On the surface, one conclusion from the results here is that any major enhancement in asymmetry requires the jamming of particles. Further examination, however, has revealed a complicated relationship between coating

material, particle concentration, operating conditions, and their impact on the efficacy of UCAs. Low concentration of particles, for example the 0.4 to 0.6 range in Figure 3.12b, leads to a drop in asymmetry where the particles do not jam. A stiffer shell may also inhibit jamming at low insonation pressures. This is not to say that coatings with high stiffness or viscosity are always disadvantageous. Rather that the mere addition of nanoparticles to a bubble coating will not automatically result in higher non-linearity and may require adjustments in operational parameters such as insonation frequency and acoustic pressure. This will be discussed further at the end of this chapter.

3.4.5. Asymmetry, Harmonic, and Sub-Harmonic Content

The primary motivation behind developing nanoparticle coated UCAs is to increase the harmonic content of their signal. This will allow isolation of signals unique to UCAs from the reflection from their surroundings. Experimental studies on armoured bubbles conducted to date have demonstrated an enhanced harmonic response compared to surfactant–only coated bubbles. Interestingly, similar trends have also been observed in the sub-harmonic response; something that can have significant implications in the utility of armoured microbubbles as UCAs. This section will concentrate on the ability of the models presented earlier to predict the enhancements in armoured bubble response observed experimentally by other colleagues.

Figure 3.13 shows the results of experimental investigation, conducted by Paul Rademeyer at the University of Oxford, into the acoustic responses of armoured and unarmoured bubbles. The details of how the experiments were carried out have been included in Appendix A of this thesis. It is appropriate, however, to include a brief description here. Armoured and unarmoured bubbles with a mean radius of 4.0μm were exposed to 5 cycle, 2.0 MHz Gaussian windowed pulses of ultrasound. The peak excitation pressure was varied from 50 to 600 kPa. The signal reflected from the bubbles were collected at 90° using a 3.5 MHz focused transducer and processed using MATLAB's native Fast Fourier Transform function (`fft.m`). The solid lines in Figure 3.13 represent exponential fits to the acoustic data using the weighted mean average at each pressure. The dotted lines represent the 95% confidence intervals in

each case. The results here show a visible enhancement of both harmonic and subharmonic components of in the reflected signal for the armoured microbubbles.

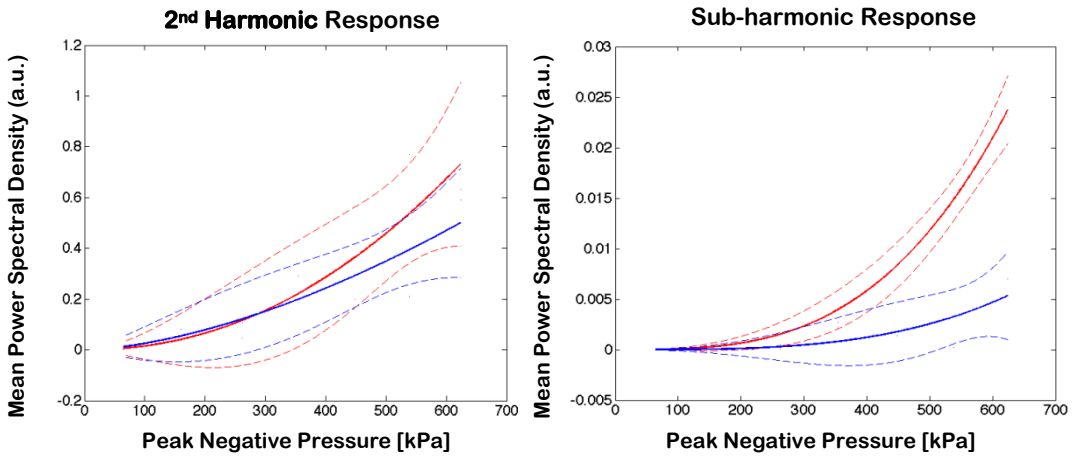

(a) (b)

Figure 3.13 - Experimental investigation of harmonic and subharmonic components of scattered pressure signal from microbubbles with armoured (Red) and unarmoured (Blue), exponentially fitted to the acoustic data based on the mean weighted average at each pressure. The dotted lines indicate observational confidence interval of 95%. (Courtesy of P. Rademeyer, BUBBL, Oxford University).

Seeking a quantitative comparison between the theoretical results here is somewhat impractical, mainly because of the inability to independently measure the bubble coating parameters. These are usually determined through 'fitting' a dynamic equation, such as those presented in this chapter, to the experimental measurements. Moreover, converting the results in Figure 3.13 to a meaningful quantity such as pressure is not straight forward as the response of the detecting transducer is not the same for all frequencies and their error margin have been shown to departure from the manufacturers' data.

The coating parameters used were μ_{s0}=0.9 Pa.s, G_{s0}=15.0 MPa, and d_{s0}= at 4.0 nm which reflect the published values for contrast agents with similar coating material. Recent experimental investigations by Hosny *et al.* [201] using FLIM (Fluorescence Lifetime Imaging Microscopy) have demonstrated the shear viscosity to be in the range 0.1 - 1 Pa.s. In addition, it was found that the shell is made up of multiple layers of surfactant molecules. The parameters relating to the nanoparticles were set as ϕ_0=0.78, ϕ_{max}=0.82, and X_{max}=8.0; meaning that the armoured bubble is close to its jamming radius. Simulations were conducted using the thin shell model, with the insonation parameters the same as those in the experiments. The frequency content

of the scattered pressure signal was calculated using the same method outlined in 3.4.2. The maximum amplitude of power spectral density was recorded within a window around ½ and 2 times the fundamental frequency corresponding respectively to sub-harmonic and 2nd harmonic contents.

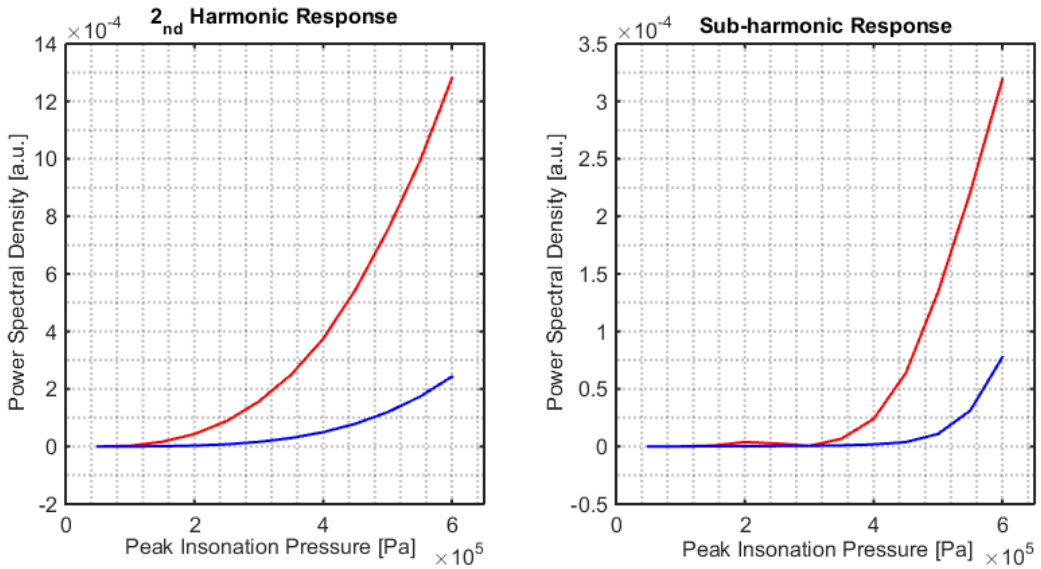

(a) (b)

Figure 3.14 – Comparison between the harmonic and sub-harmonic content of armoured (Red) and unarmoured microbubbles.

The results, as displayed in Figure 3.14, show an enhancement in the harmonic and sub-harmonic responses of the armoured bubble. They exhibit the same trends as the experimental results shown in Figure 3.13. The increased asymmetry of the oscillations, as a result of the asymmetric stiffness imposed by the nanoparticles, is responsible for the increased harmonic response shown in Figure 3.14a. The enhancement in the harmonic response is shown in Figure 3.14a to occur immediately after 100 kPa. This indicates a better performance in comparison to the experimental results shown in Figure 3.13a where the enhancement is relatively lower and starts at the higher acoustic pressure of 300 kPa. This perhaps highlights some of the difficulties in matching theoretical results to the experiments. While parameters can be tuned perfectly in the model, there will be a degree of variability in the composition of the microbubbles. The inability of independently measuring the parameters used in simulations also means that there is no way of verifying the uniformity in the composition of the microbubbles produced in experiments. For example, the concentration of particles adsorbed on the bubble surface during manufacturing can widely vary between individual bubbles. Bubbles with very low

particle concentrations, as shown in 3.4.4, may exhibit lower asymmetry, even when compared to those with no nanoparticles.

The origin of the sub-harmonic response is the fact that the frequency of insonation is larger than the resonance frequency of the bubble as calculated in Figure 3.7. If the amplitude of oscillation is sufficiently large, the bubble will continue to oscillate at its resonance frequency for a few periods after the insonation has ended. The shift in the resonance frequency, furthermore, means that an armored bubble may exhibit larger amplitude of oscillation at a higher frequency compared to an unarmoured, but otherwise identical, bubble. An example of this can be found in the responses 1 (unarmoured) and 2 (armoured) in Figure 3.7 where the latter shows visibly larger maximum response at the off-resonance frequency of at 2.0 MHz. The increase in insonation pressure amplifies the response at a given frequency and thus the bubble will oscillate for longer and at higher amplitudes at its resonance frequency.

The results and discussion presented in this section first illustrate the ability of the models presented earlier to illustrate the trends observed in the experiments. In addition, a number of difficulties in matching theoretical results to the experiments have been highlighted. This is an issue which will be revisited repeatedly and commented on further in the next chapters.

3.5. Summary

The aim of this chapter was to develop models to account for the observed increase in the nonlinear character of nanoparticle coated bubbles under ultrasound excitation. Enhancing the harmonic content at low excitation pressures has been identified as an important avenue in developing new UCAs as it can increase the image contrast without increasing the risk of microbubble destruction and/or harmful bio-effects. Adding nanoparticles increases the resistance of coating to compression through a "jamming" effect. This happens when the bubble is compressed to the extent that the particles reach their packing density.

The influence of nanoparticles was taken into account by introducing into the equation of motion effective coating viscosity and stiffness of which increase as the nanoparticle packing density is approached. Two types of coating were considered: A thin coating with constant thickness and an incompressible coating of finite variable thickness. Equations for both cases were derived based on existing approaches and solved by numerical integration.

The interplay between the nanoparticle concentration and coating properties was found to be complex and to significantly affect microbubble oscillations and associated degree of nonlinearity. Large increases in asymmetry, as shown in Figure 3.11, were only observed when the minimum radius of the bubble reached the limit of particle packing. Once jamming has occurred, the asymmetry of oscillations continues to increase with the driving pressure. For an acoustic signal of a given frequency and pressure, the armoured bubbles showed enhancement of the second harmonic as well as subharmonic content at moderate acoustic pressures as shown and discussed in section 3.4.5.

Developing a model for and studying the response of armoured microbubbles led to new findings with regards to the optimisation of insonation parameters and coating composition. Nanoparticle embedded coatings exhibit larger effective viscosity and bubbles with such coatings were shown to demonstrate optimal response at higher insonation frequencies. There can therefore be combinations of particle volume fraction and viscosity where significant damping masks the desired effect of the nanoparticles. A high viscosity coating with low particle concentration, for example, will require higher insonation pressure in order to exhibit enhanced nonlinearity.

Such factors should therefore be taken into account when designing new bubbles to use as UCAs. Further comments on design and manufacturing of armoured bubbles will be provided in chapters 5 and 6.

In is necessary to provide a few comments about the limitation of the models presented here. Apart from the assumptions of small wall movement taken in deriving the equations of motion, another reason for limiting the bubble vibrations to small oscillations was that the models do not account for any change in shell composition as a consequence of large oscillations. Under large oscillations, the high pressure on the nanoparticle coating may result in ejection of particles from the bubble surface. The mechanism by which this happens is analogous to lipid shedding [202]. The reduction of nanoparticle concentration will similarly affect the equilibrium radius of the bubble and thus change its behaviour. Furthermore, it is likely that the bubble cannot maintain a spherical shape under large pressures. The nanoparticle shell can also collapse into the bubble, allowing the gas inside to escape, and effectively create a mass of nanoparticles clumped together. The practicality of developing a model in which such outcomes are considered will be further discussed in Chapter 6.

Another factor omitted in the current study was the nonlinearity of the coating material itself. As discussed before, both stiffness and viscosity of a surfactant coating have been reported to be dependent on shell strain, insonation frequency, and concentration. This was done here for sake of simplification and to avoid introducing more yet-to-be-experimentally-determined parameters into consideration.

The theoretical work presented in this chapter together with experimental data provided by co-workers has partly verified the utility of armoured bubbles for harmonic imaging. Whether the amplification in nonlinearity is sufficient for medical imaging applications requires further theoretical and experimental investigations which take more realistic environmental conditions into account. This will be discussed further in Chapter 6.

4. Stability against Dissolution

4.1. Overview

Uncoated microbubbles tend to dissolve in liquids due to the gas concentration gradient at their boundary as well as interfacial tension. The rate of bubble at which a bubble dissolves depends on its radius, the gas-liquid coefficient of diffusion, and the amount of gas dissolved in the liquid. Adequate circulation time is an essential requirement for any imaging contrast agent. UCAs thus must be resilient against dissolution to provide contrast enhancement at their intended target during a diagnostic procedure. In addition, the ability to maintain a constant radius at rest, as previously discussed, is an important factor when it comes to the predictability and reproducibility of UCAs' response to ultrasound.

The effect of nanoparticles on the nonlinear behaviour of UCA was modelled in the previous chapter. In addition to enhanced nonlinear behaviour, populations of nanoparticle coated microbubbles have exhibited considerable resistance against dissolution while maintaining monodispersity. The aim of this chapter is to devise and test hypotheses regarding this observed longevity of nanoparticle coated microbubbles. A number of stabilising mechanisms due to both the surfactant coating and the presence of nanoparticles are first discussed. A dissolution model developed by Epstein and Plesset [10] for uncoated bubbles is then modified to include the effect of proposed stabilising mechanisms. The validity of the new model is tested against experimental observations followed by a discussion of the results.

4.2. Dissolution of Uncoated Microbubbles

This section provides a brief review of the theoretical model derived by Epstein and Plesset for the dissolution of an uncoated microbubble in a quiescent liquid. Prior to that, however, it is necessary to provide a description of the physical parameters which will be referred to in this and later sections. A schematic of a nanoparticle coated microbubble and its surrounding environment is shown in Figure 4.1. Here, R is the microbubble radius, and r is the radial distance from the centre of the microbubble. D and σ are respectively the coefficient of diffusion and interfacial tension which, in the case of a coated microbubble, are both functions of R. The density of the gas inside the bubble is denoted by $\rho(R)$, and $\rho(\infty)$ is the density of the gas at the ambient pressure. The concentration of the dissolved gas, assumed to be uniform throughout the liquid, is denoted by C_i, and C_{sat} is the saturation concentration. The symbols (R) and (∞) that follow C_{sat} respectively denote values at radius and far away from the surface of the bubble. The relationship between saturation concentration and pressure is governed by Henry's law in which the amount of gas soluble in a liquid is directly proportional to the partial pressure of that gas. The constant of proportionality is termed Henry's constant and is a function of temperature. For the purposes of this work, the bulk solution is assumed to be at a constant temperature and pressure and therefore $C_{sat}(\infty)$ is constant. $C_{sat}(R)$, on the other hand, will change according to the Laplace pressure, given by

$$P_{Laplace} = \frac{2\sigma}{r_c}, \tag{4.1}$$

where r_c is radius of curvature at the interface. As long as the bubble remains spherical, its interface is centred at the centre of the bubble and thus $r_c = R$.

Fick's first law states that the flux, J, of a component of concentration, C, across a unit area of membrane, in a predefined plane, is proportional to the concentration differential across that plane, and is expressed in spherical polar coordinates as

$$J = -D\nabla C = -D\frac{\partial C}{\partial r}. \tag{4.2}$$

The mass flow rate through a microbubble surface will therefore be

$$\frac{dm}{dt} = -4\pi R^2 D \frac{\partial C}{\partial r}. \tag{4.3}$$

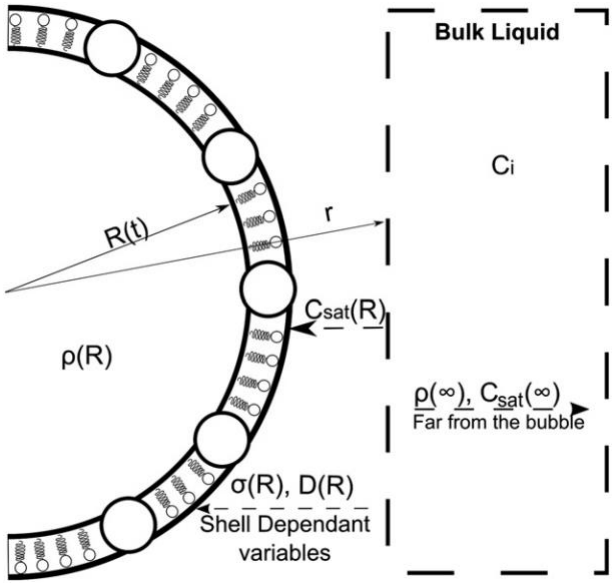

Figure 4.1 Schematic of a microbubble with surfactant and nanoparticle coating suspended in an infinite liquid of variable dissolved gas content. The thickness of the shell is in reality much smaller than the bubble radius but has been exaggerated here for illustration purposes.

Ignoring the effects of convection and using a solution given in Carslaw [203], Epstein and Plesset [204] found that

$$\left(\frac{\partial C}{\partial r}\right)_R = \left[C_i - C_{sat}(R)\right]\left[\frac{1}{R} + \frac{1}{\sqrt{(\pi D t)}}\right]. \tag{4.4}$$

Substituting (4.4) into (4.3) gives

$$\frac{dm}{dt} = 4\pi R^2 D\left(\frac{\partial C}{\partial r}\right)_R = 4\pi R^2 D\left(C_i - C_{sat}(R)\right)\left[\frac{1}{R} + \frac{1}{\sqrt{(\pi D t)}}\right]. \tag{4.5}$$

Now from the ideal gas law, the equation of state for a coated gas bubble can be written as

$$P + \frac{2\sigma}{R} = \left(\frac{B}{M}\right)\rho(R)T, \tag{4.6}$$

where B is the universal gas constant, M is the molecular weight of the gas, ρ is the density of the gas in the bubble. Rearranging (4.6) in terms of gas density gives

$$\rho(R) = \frac{M}{BT} P + \frac{2\sigma}{R} \frac{M}{BT}. \tag{4.7}$$

The mass of the gas bubble is therefore given by,

$$m = V\rho(R) = \frac{4}{3}\pi R^3 \rho(\infty) + \frac{4}{3}\pi R^3 \frac{2M\sigma}{BTR} = \frac{4}{3}\pi R^3 \rho(\infty) + \frac{8M}{3BT}\pi R^2 \sigma, \tag{4.8}$$

where the term (∞) denotes conditions at zero curvature as above. Another expression for flux can, therefore, be written as

$$\frac{dm}{dt} = 4\pi R^2 \frac{dR}{dt}\left(\rho(\infty) + \frac{4M\sigma}{3BTR}\right). \tag{4.9}$$

Equating (4.5) to (4.9) finally yields

$$\frac{dR}{dt} = \frac{C_i - C_{sat}(R)}{\left(\rho(\infty) + \frac{4M\sigma}{3BTR}\right)}\left[\frac{D}{R} + \sqrt{\frac{D}{(\pi t)}}\right]. \tag{4.10}$$

It should be noted that convection has been neglected in deriving (4.10). The fully coupled mass transport problem was solved by Ready and Cooper [161] and Weinberg [205]. It was found that the effects of convection, particularly for bubbles with diameter of less than 1 mm, were however very small compared to those of surface tension. The following derivation will therefore concentrate on the effects of surfactants and solid particles upon bubble dissolution.

4.3. Influence of Surfactant Coating

The effect of a surfactant coating is to reduce the interfacial tension as well as providing a barrier to mass transfer across the bubble wall. As discussed before, these effects become significant with increasing surface concentration of surfactant molecules. The relationship between interfacial tension and surface concentration has been the subject of a number of experimental studies [206-208]. Two theoretical models describing this relation were presented previously (c.f. section 2.5.2). The value of the parameters used in both of these models, are derived from fitting to experimental data. In addition, discontinuities in both of these models further

complicate their inclusion into a new dissolution model. The relationship between surface concentration and interfacial tension here is therefore written as a Sigmoid function

$$\sigma(\Gamma) = \sigma_{\min} + \frac{\sigma_0 - \sigma_{\min}}{\left(1 - Q\exp\left(-b\left(\Gamma - m\right)\right)\right)^{\frac{1}{\upsilon}}}, \tag{4.11}$$

where σ_0 is the bulk surface tension of surrounding liquid, $\sigma_{\min}$ is the minimum surface tension, Γ is the instantaneous surface concentration, and parameters *Q, b, m,* and υ are dependent on the characteristics of individual lipids/surfactants. Parameter values can be determined by fitting (4.11) to experimental results.

Reduction of interfacial tension as a result of the existence of a surface active monolayer, however, is not enough to account for the lower mass transfer rate from a bubble. This was noted by Borden *et al.* [171] where they compared the radius-time curve for dissolution of a microbubble with no interfacial tension against their experimental measurements. A conclusion was drawn that, aside from reducing the interfacial tension, the monolayer also acts as a barrier to mass transfer. Such resistance to permeation, among other factors, is likely dependent on surface concentration of a given surfactant. To author's best knowledge, no conclusive experimental data exist on dissolution through lipid/surfactant monolayers at the time of writing. Experimental studies by Nedyalkov *et al.* [209] have suggested the relation of monolayer permeation to be exponentially related in the case of "Black Foam" films, which are surfaces with metastable regions that appear black when their surface is illuminated. It is hypothesised that a similar relation exists for lipid/surfactant films and can be written as

$$D(\Gamma) = D_0 Y(\Gamma),\ Y(\Gamma) = a_1 \exp\left[a_2\left(1 - \left(\frac{\Gamma}{\Gamma_{\max}}\right)\right)\right], \tag{4.12}$$

where a_1 and a_2 are surfactant specific constants, D_0 denotes the diffusion coefficient of the gas/liquid interface in the absence of any surfactant and Γ is the instantaneous concentration of surfactant on microbubble's surface. Here the surfactant molecules are considered to be responsible for resistance to mass transfer. When $\Gamma = \Gamma_{\max}$, the power of the exponential term is 0. Thus the product of a_1 and D_0 is the effective

diffusion coefficient of the surfactant when maximum surface concentration is reached. The constant a_2 scales the dependence of D on the change in surface concentration. At lower surfactant concentrations, the value of D will increase until $\Gamma = 0$, at which point $D(\Gamma)$ should revert to $D0$. This requires the condition $a_1 \exp[a_2] = 1$ to be true and thus puts a restriction upon the value of a_2.

4.4. Influence of Nanoparticles

4.4.1. Reduction of Surface Area

The mass transfer rate of gas from the core of a microbubble to its surroundings, as discussed previously, is directly proportional to the available interfacial area for the gas molecules to escape through. Compared to an uncoated bubble of the same size, an "armoured" bubble will have a smaller surface area available for gas diffusion due to the presence of the nanoparticles. Assuming that no further transfer of nanoparticles takes place between microbubble interface and the bulk liquid throughout the dissolution process, the proportion of the surface area covered by nanoparticles increases as the "armoured" bubble becomes smaller. The instantaneous uncovered interfacial surface area, S_D, can be written as:

$$S_D = 4\pi R^2 - \phi 4\pi R^2 = 4\pi R^2 (1-\phi) = 4\pi R^2 \left(1 - \phi_0 \left(\frac{R_i^{\,2}}{R^2}\right)\right) \tag{4.13}$$

where ϕ_0 and ϕ are respectively the initial and instantaneous fraction of microbubble surface area covered by nanoparticles. It is obvious from equation (4.13) that at the limit of $R \rightarrow 0$, $\phi \rightarrow \infty$. This is, however, physically impossible and ϕ is limited to a maximum packing density ϕ_{max}. The maximum packing density of hard spheres on a cylindrical or spherical surface is always less than 1, leading to further diffusion through the uncovered surface regions. The ramifications of this are discussed next.

4.4.2. Local Modification of Surface Curvature

It is impossible for spherical particles to fully cover a bubble's surface. The gas inside the bubble can therefore diffuse into the surrounding liquid through the gaps between particles either because of the gradient across, and/or the curvature of these uncovered regions. Studies of particle coated bubbles, however, have demonstrated stability over long periods of time [13,180]. This implies that gas diffusion is still

somehow significantly inhibited. The phenomena discussed in 4.3 and 4.4.1 only act to retard the dissolution process. Further consideration should therefore be given to the events after particle jamming occurs.

The basis of the work presented below follows that originally developed by Kam and Rossen [210]. They stipulated that stability observed in particle coated bubbles is as a result of small distortions of the uncovered portion of the interface between the particles. The process is illustrated schematically in Figure 4.2. Note that the size of the particles relative to the bubble radius has been exaggerated here for illustration purposes.

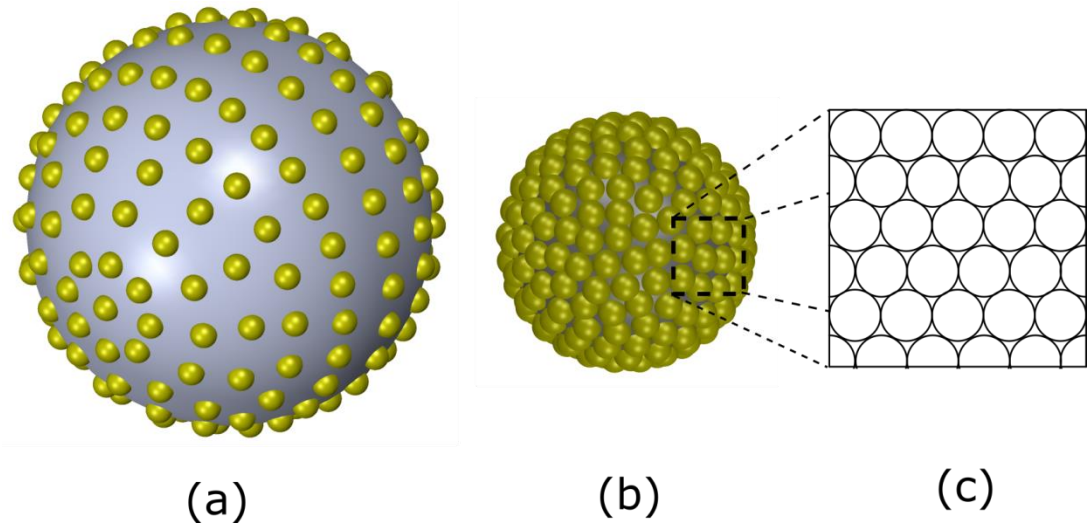

Figure 4.2 – Three-dimensional illustration of a particle coated microbubble undergoing dissolution. a) The particles are far away from each other. The bubble shape at this point can be assumed to be spherical. b) As the bubble shrinks, the particles become close and closer until they reach their close packing density. c) An ideal close packing scenario, where each particle is surrounded by 6 others in a hexagonal arrangement which provides maximum coverage of approx. 90%.

Figure 4.2a illustrates the bubble at a point where the particles are far from each other. At this stage, its dissolution is driven by the concentration gradient across the bubble interface as well as the interfacial tension. Supposing that the particles are uniform and spherical, it can be assumed that the bubble surface is free from distortions. The radius of curvature for the bubble in Figure 4.2a is therefore equal to its instantaneous radius (r_c=R). The surface density of nanoparticles increases as the armoured bubble shrinks, up to a point where they form a packed structure (Figure 4.2b). The structure of jammed nanoparticles here supports the bubble against interfacial tension. Figure 4.2c illustrates a small surface area of the microbubble on which the particles are close packed in a hexagonal arrangement. In reality, the

particles are likely to form a mixture of hexagonal and squared packing structures around a sphere.

The radius of the bubble at which packing occurs is termed packing radius and denoted by the symbol R_p. The shape of the interface is simply assumed to be spherical prior to the particles jamming. After this point, however, the interface becomes complex. The problem is therefore simplified by presenting it in two-dimensions both for illustrative and modelling purposes. Figure 4.3a depicts the bubble at packing radius (R_p). The particles here are shown to be separated by larger circles. It is necessary to briefly explain the reason behind this. The maximum packing density on a circle (as in the 2D case here) is 100%, meaning no interface can exist between the particles. In order to compensate for this, a minimum distance between the centres of particles at packing density is defined and given by $2(r_p + \delta)$, where r_p is the particle radius and δ is a length quantity based on the packing structure. Further information about how the value of δ is chosen can be found in 4.6.2.

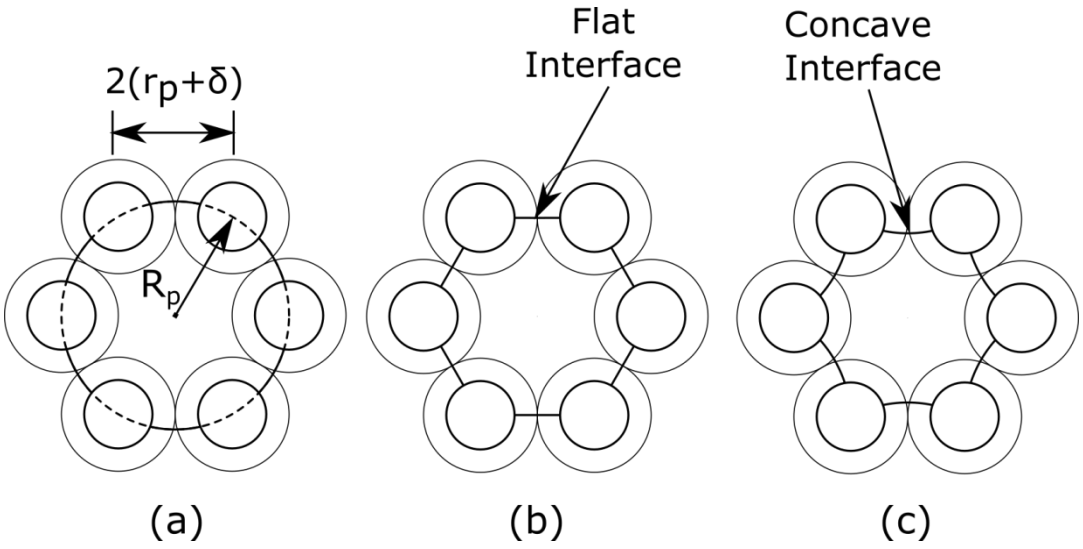

Figure 4.3 – Deformation of local curvature after close packing of particles. Larger circles represent the equivalent distance between neighbouring particles in 2D when close packed. a) The particles have just reached their close packing density and the interfaces between particles have their centre at the centre of the bubble. *R*p denotes the bubble's radius at this point. b) As the gas inside of the bubble escapes, the interfaces move towards the centre of the bubble and eventually flatten and laplace's pressure diminishes. c) Upon further gas diffusion into the surrounding liquid, the interfaces become concave and Laplace's pressure becomes negative.

At R=R_p, the centres of interfaces coincide with that of the bubble and thus $r_c = R_p$. Gas diffusion from the bubble into its surrounding liquid will continue through the gaps between the packed particles. The bubble, on the other hand, maintains its spherical shape and will not shrink due to the supporting structure that the particles provide. Any further decrease in the gas volume inside the bubble, therefore, requires the interface to move towards the centre of the bubble while maintaining some contact with the particles. This leads to the interface to become flat (Figure 4.3b) or concave (Figure 4.3c). Consequently, the Laplace pressure will diminish or becomes negative, thus removing a major driver of dissolution from the process.

According to the hypothesis presented above, therefore, the radius of curvature, r_c, can be described in two regimes:

$$r_c = \begin{cases} R, R \geq R_p \\ \mathrm{f}(R), R < R_p \end{cases}, \tag{4.14}$$

where f(R) is a function of the radius of the bubble. At 15nm±10%, the diameter of the nanoparticles considered in this study is ~1000 or more times smaller than the radius of microbubbles usually employed in medical diagnostic imaging, whose radii range from 1-10μm. The angle and arc length between two nanoparticles will thus be very small at packing density. Local curvatures are, therefore, highly sensitive to very small changes in volume. The speed of this alteration is rapid, so much so that computing the positions of particles and interfaces based on interfacial tension and free-surface energy between the phases would not yield usable information about the evolution of local curvatures. This process is therefore simplified using the approach described next and demonstrated in Figure 4.4.

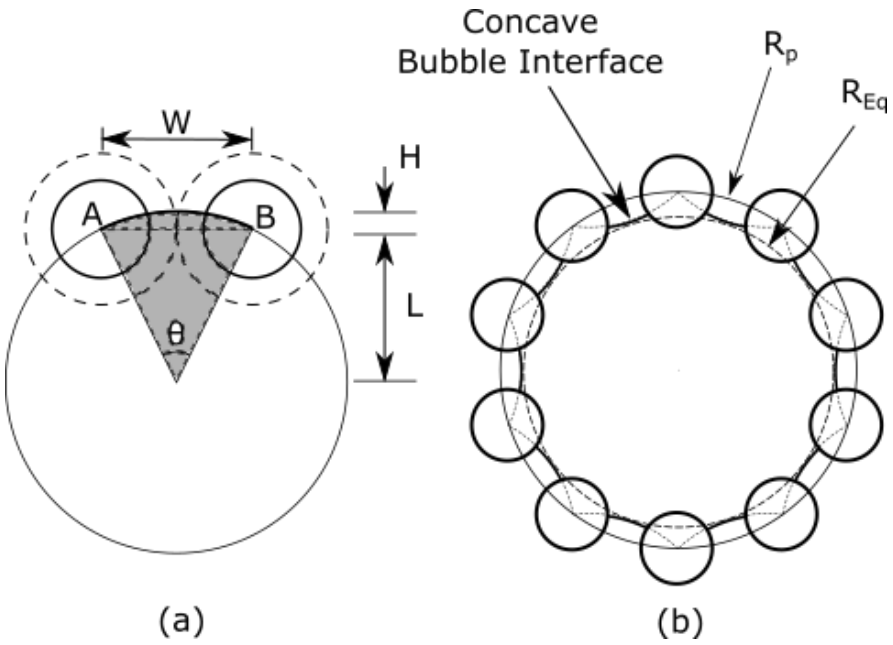

Figure 4.4 –a) Definition of geometrical parameters used in the modelling of effective curvature. b) Exaggerated schematic of change in local curvature due to diffusion after packing density is reached. The model presumes that the perimeter of an imaginary bubble with radius R_{Eq} is tangential to the midpoint of each interface.

Consider the grey segment in Figure 4.4a. The arc AB represents the interface between the two particles. Its ends are fixed at the centre of the neighbouring particles. Here, W is the chord length of the segment, H is its height, and L is the height of its triangular portion. The radius of curvature for AB, r_c, can be written as

$$r_c\left(R < R_p\right) = \frac{H}{2} + \frac{W^2}{8H}, \tag{4.15}$$

with the chord length, W, given by

$$W = 2\left(r_p + \delta\right). \tag{4.16}$$

The value of H can be approximated if the distance between the midpoint of arc AB and the centre of the bubble is known. Imagine another bubble whose surface does not deform upon the close packing of the particles. The instantaneous bubble radius here can be calculated using an equation like a modified version of (4.10) which accounts for the effects discussed in 4.3 and 4.4.1. The radius of this bubble, illustrated in Figure 4.4b as the dotted circle inside the bubble, is denoted by R_{Eq}. Assume that the perimeter of the imaginary bubble is tangential to the midpoint of each of the uncovered interfaces. Then, as R_{Eq} reduces, the midpoint of each

interface is pulled in towards the centre of the bubble. An approximation for H can, therefore, be written as

$$H = R_{Eq} - L = R_{Eq} - R_p \cos(0.5\theta). \tag{4.17}$$

The segment angle, θ, is given by

$$\theta = 2arcsin\left(\frac{W}{2R_p}\right) \approx 2\left[\left(\frac{2(r_p+\delta)}{2R_p}\right) + \frac{1}{2}\frac{1}{3}\left(\frac{2(r_p+\delta)}{2R_p}\right)^3 + \ldots\right]. \tag{4.18}$$

In the case considered here, W and R_p are respectively in the orders of 10^{-9} and 10^{-6}, leading to $\theta \approx 0$ and $\cos(\theta/2) \approx 1$. Substituting equations (4.16) and (4.17) in (4.15) gives:

$$r_c(R < R_p) = \frac{R_{Eq} - R_p \cos(0.5\theta)}{2} + \frac{1}{2}\frac{(r_p+\delta)^2}{R_{Eq} - R_p \cos(0.5\theta)}. \tag{4.19}$$

Finally, using the small angle approximation and substituting (4.19) into (4.14) yields:

$$r_c = \begin{cases} R, R \geq R_p \\ \frac{1}{2}\left[R_{Eq} - R_p + \frac{(r_p+\delta)^2}{R_{Eq} - R_p}\right], R < R_p \end{cases} \tag{4.20}$$

4.5. A New Equation

The modifications proposed in sections 4.3 and 4.4 can be applied to the derivation described in section 4.2. Radius dependant diffusion and effective surface area terms, described in equations (4.12) and (4.13) are used to modify (4.5). Thus the rate of mass transfer can be written as

$$\frac{dm}{dt} = 4\pi R^2 \left(C_i - C_{sat}\left(R\right)\right)\left[\frac{D(R)}{R} + \sqrt{\frac{D(R)}{\pi t}}\right]\left(1 - \phi_0\left(\frac{R_i}{R}\right)^2\right). \tag{4.21}$$

Application of radius dependency to surface tension and radius of curvature to (4.9) results in

$$\frac{dm}{dt} = 4\pi R^2 \frac{dR}{dt} \times \left(\rho(\infty) + \frac{2M}{BT}\left(\frac{\sigma(R)}{r_c(R)} + \frac{R}{3r_c(R)}\frac{d\sigma(R)}{dR} + \frac{R\sigma(R)}{3}\frac{d}{dR}\left(\frac{1}{r_c(R)}\right)\right)\right). \tag{4.22}$$

Dependency on R is dropped from this point onward for clearer presentation. Following Epstein and Plesset [204], the following relationships can be defined:

$$C_f = \frac{C_i}{C_{sat}},\ \tau = \frac{2M}{BT},\ \text{and}\ d = \frac{C_{sat}(\infty)}{\rho(\infty)} = \frac{C_{sat}(R)}{\rho(R)} = \frac{C_{sat}(R)}{\rho(\infty) + \tau\sigma / R}$$

Equating (4.21) and (4.22) and rearranging in for the derivative of radius gives

$$\frac{dR}{dt} = d\,\frac{C_f - 1 - \dfrac{\tau\sigma}{r_c\rho(\infty)}}{\left(\rho(\infty) + \dfrac{2M}{BT}\left(\dfrac{\sigma}{r_c} + \dfrac{R}{3r_c}\dfrac{d\sigma}{dR} + \dfrac{R\sigma}{3}\dfrac{d}{dR}\left(\dfrac{1}{r_c}\right)\right)\right)} \times \left[\frac{D}{R} + \sqrt{\frac{D}{\pi t}}\right]\left(1 - f_{p0}\left(\frac{R_i}{R}\right)^2\right). \tag{4.23}$$

Finally, the derivatives in denominator must be calculated. Differentiating $\sigma(R)$ with respect to R gives:

$$\frac{d\sigma}{dR} = \left(\sigma_0 - \sigma_{\min}\right)\left[\frac{-2\dfrac{\Gamma}{R}Qb\exp\left[-b\left(\Gamma - m\right)\right]}{\nu\left(1 + Q\exp\left(-b\left(\Gamma - m\right)\right)\right)^{(1+1/\nu)}}\right] \tag{4.24}$$

where surfactant concentration is given by $\Gamma = \Gamma_0 \left(R_i / R \right)^2$. The derivative of the *1/r_c* term can be calculated through:

$$r_c = \begin{cases} R, R \geq R_p \\ r_c(R), R < R_p \end{cases} \Rightarrow \frac{1}{r_c} = \begin{cases} \frac{1}{R}, R \geq R_p \\ \zeta(R), R < R_p \end{cases}$$

$$\frac{d}{dR}\left(\frac{1}{r_c}\right)_{R<R_p} = \frac{d}{dH}\left(\frac{1}{r_c}\right)\frac{dH}{dR} = \frac{8\left(W^2 - 4H^2\right)}{\left(4H^2 + W^2\right)^2} \approx \frac{2\left[\left(r_p + \delta\right)^2 - \left(R_{Eq} - R_p\right)^2\right]}{\left[\left(R_{Eq} - R_p\right)^2 + \left(r_p + \delta\right)^2\right]^2}$$

$$\therefore \frac{d}{dR}\left(\frac{1}{r_c}\right) = \begin{cases} -\frac{1}{R^2}, R \geq R_p \\ \frac{2\left[\left(r_p + \delta\right)^2 - \left(R_{Eq} - R_p\right)^2\right]}{\left[\left(R_{Eq} - R_p\right)^2 + \left(r_p + \delta\right)^2\right]^2}, R < R_p \end{cases}$$

It is necessary here to make a few comments about r_c, $d / dR\left(1 / r_c\right)$, and the importance of the terms including them in (4.23). The model for r_c, given by (4.20), predicts a flat surface at $R = R_p$ due to the small angle estimation made in its derivation and is thus discontinuous. This discontinuity is exacerbated in the derivative of $1/r_c$ where, depending on the values of r_p and delta, there can be a several orders of magnitude shift in its value at $R = R_p$. For example, when r_p and delta are in orders of 10^{-8} and the bubble radius is in order of 10^{-6}, the value of $d / dR\left(1 / r_c\right)$ will shift from the order of 10^{12} to 10^{16}. The shift causes significant nonlinearity in (4.23) and, since the derivative term appears in its denominator, radically reduces the rate of dissolution. This is however not unexpected expected since the change in r_c for $R < R_p$ is governed by a different process and depends on the size of and the space between the nanoparticles. The derivative term eventually falls in magnitude as $R_{Eq} - R_p \to W / 2$, which is when the other r_c terms in the denominator become large enough to compensate for its diminishing and thus the bubble will appear to have stabilised.

4.6. Results and Discussion

4.6.1. Numerical Solution

Numerical integration of equation (4.23) presents a number of issues; the time term appears in the denominator and the small magnitude of some terms may necessitate extremely small time steps which may result in inaccurate solutions. These are overcome by the introduction of new dimensionless variables into (4.23):

$$\hat{R} = \frac{R}{R_i}, \quad \hat{t}^2 = \left(\frac{2dD_0}{R_i^2} \right) t$$

The change of variables propagates through all radius dependent terms and requires the rescaling of R_p, r_p, and δ, resulting in the following:

$$\Gamma = \Gamma_0 \left(1/\hat{R}\right)^2, \quad \hat{r}_c = R_i r_c(\hat{R}) \quad , \quad \frac{d\sigma(\hat{R})}{d\hat{R}} = \frac{d\sigma(R)}{dR} R_i \quad , \quad \frac{d}{d\hat{r}_c}\left(\frac{1}{r_c(\hat{R})} \right) = \frac{d}{dr_c}\left(\frac{1}{r_c(R)} \right) R_i$$

Combining gives:

$$\frac{d\hat{R}}{d\hat{t}} = -\frac{1 - C_f + \dfrac{\tau\sigma}{\hat{r}_c R_i \rho(\infty)}}{\left(1 + \dfrac{\tau}{\rho_\infty}\left(\dfrac{\sigma}{\hat{r}_c R_i} + \dfrac{\hat{R}}{3\hat{r}_c}\dfrac{d\sigma}{d\hat{R}} + \dfrac{\hat{R} R_i \sigma}{3}\dfrac{d}{d\hat{R}}\left(\dfrac{1}{\hat{r}_c} \right) \right) \right)} \left[\frac{Y\hat{t}}{\hat{R}} + \sqrt{\frac{2dY}{\pi}} \right] \left[1 - f_{p0}\left(\frac{1}{\hat{R}} \right)^2 \right] \quad (4.25)$$

Equation (4.25) and its associated functions were coded in MATLAB® (R2012b, MathWorks Inc., USA) which provides various functions for numerical solution of differential equations. Use of standard 4th-5th order Runge-Kutta method (function ode45) is inefficient and yields inaccurate results as rapid variations in local curvature after packing requires the use of time steps beyond the accuracy of the solver. Equation (4.25) is therefore solved using the variable order method for stiff ODEs (function ode15s).

4.6.2. Choice of Parameters

Stability experiments for microbubble populations were conducted by *Graciela Mohamedi* (Biomaterials Laboratory, Mechanical Engineering department, UCL). Microbubbles produced using a micro-fluidic device were collected in clean glass vials and suspended in glycerol on glass slides. The liquid phase in the device contained a citrate gold suspension to which 0.5 vol% (5 mg/mL) poly(ethylene glycol) 40 stearate (PEG40S) and 0.01 vol% (0.67 mg/mL) 1,2-distearoyl-sn-glycero-3-phosphocholine (DSPC) were added. Nitrogen was used as the gas phase in all cases. Further details of the micro-fluidic production process can be found in [13]. A control experiment was later conducted in which the liquid phase only contained water and PEG40S. The slides were placed under an optical microscope and the bubbles were observed over a period of time. Figure 4.5 illustrates the results. It was observed that, over a period of 72 hours, the nanoparticle coated microbubbles only experienced a 14% reduction in radius and maintained their monodispersity (Figure 4.5D-F). This was compared to the control batch, shown in Figure 4.5A-C, in which higher rates of dissolution and widespread coalescence lead to highly polydisperse population over a period of 24 hours.

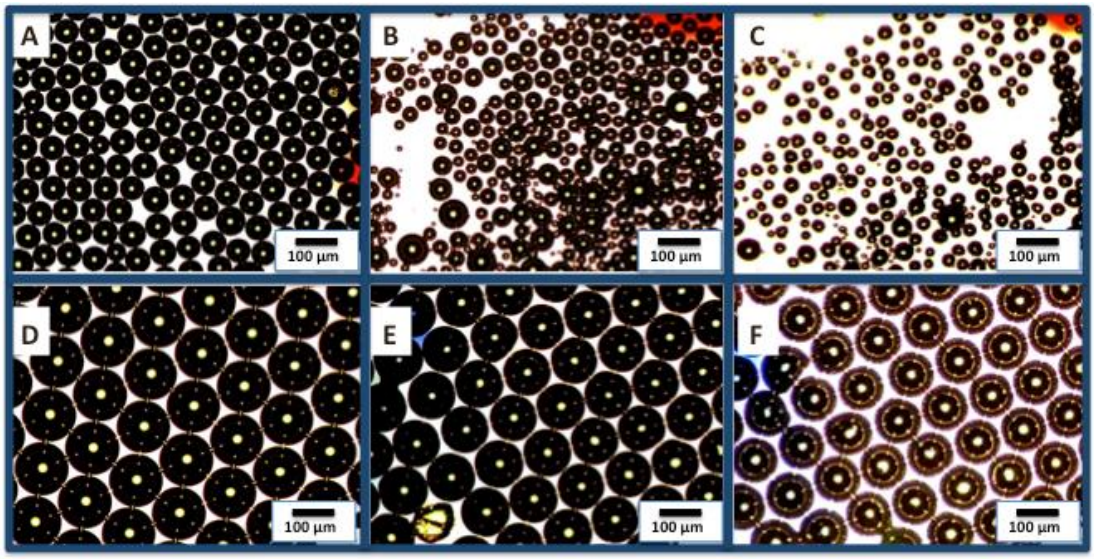

Figure 4.5 - Time study comparing the stability of microbubbles without nanoparticles (A-C) against gold nanoparticle coated microbubbles (D-F). A. t=0, B. t=60 min, C. t=24 hours, D. t=0, E. t=24 hours, F. t=72 hours (Courtesy of G. Mohamedi [13]) .

In fitting the theoretical model to the experimental results, it is appropriate to limit range of parameters as much as possible to closely match the experimental conditions. The full list of parameter values used in simulations can be found in

Table 2. It is appropriate, however, to elaborate on the thinking behind some of these choices.

A sigmoid approximation for $\sigma(R)$ was set by a fitting a curve to Marmottant's discontinuous surface tension model [144] with the surface concentration normalized with respect to Γ_{max} and elastic coefficient set to represent a slow compression (χ=*0.1*). The resulting curve along with the original piece-wise linear model can be viewed in Figure 4.6.

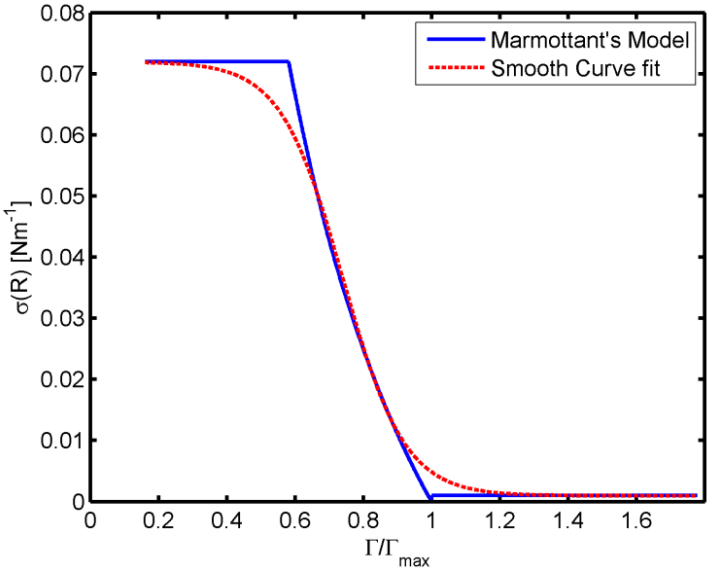

Figure 4.6 – Smooth Sigmoid curve fitted to Marmottant's discontinuous model. (*Q* =10,*m* = -11, *b* = 0.95, *v*=1.0)

Microbubbles are closely packed on the collection slides and therefore the gas to liquid volume ratio is large. It is thus reasonable to assume that the fluid is always near saturation and that the value of C_f must therefore be set accordingly. It is assumed that the ratio between saturation concentration of Nitrogen in the solution and its density to be similar to that of Nitrogen and water. The constant d is therefore set to 0.02 following Epstein and Plesset [10]. Maximum packing density of particles, ϕ_{max}, was set to 0.86 assuming that the particles are monodisperse rigid spheres packed hexagonally [211] and, therefore, $\delta = 0.05r_p$.

Parameter	Value	Unit	Parameter	Value	Unit
C_f	0.9	-	Q	10	-
ϕ_{max}	0.86	-	m	-11	-
ϕ_0	0.65,0.0	-	b	0.95	-
d	0.2	-	v	1.0	-
D_0	2.0×10^{-9}	[m^2s^{-1}]	σ_{max}	0.072	[Nm^{-1}]
a_1	0.018	-	σ_{min}	0.01	[Nm^{-1}]
a_2	4.0	-	Γ/Γ_{max}	0.34	-
r_p	7.5×10^{-9}	[m]	δ	$0.05r_p$	[m]

Table 2 - List of parameter values used in the dissolution simulations

4.6.3. Comparison with Experiments

The validity of the hypothesised stabilising mechanisms described in sections 4.3 and 4.4 was tested by first simulating the results of dissolution of nanoparticle-coated bubbles and then setting the initial particle coverage, ϕ_0, to zero for simulating the control case.

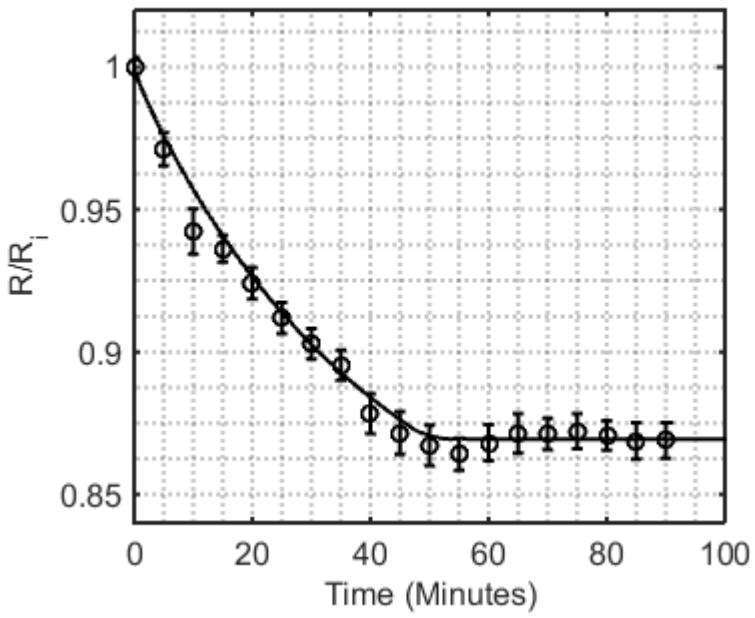

Figure 4.7 - Diffusion equation fitted to the experimental results for microbubbles coated with nanoparticles and surfactant. Initial particle concentration was set at ϕ_0=0.65 and the values of all other parameters can be found in Table 2.

The dissolution of nanoparticle-coated bubbles is presented in Figure 4.7. After a certain period of time (~60 min) the rate of mass transfer becomes negligibly small. It is hypothesized that this corresponds to the point at which the gold particles reach their packing density on the bubble surface, minimizing the surface area available for further gas diffusion and significantly reducing the effective interfacial tension due to a decrease in the surface to volume ratio.

Equation (4.26) was initially solved to simulate the results for nanoparticle-coated bubbles. Values of a_1, a_2, $\Gamma_0/\Gamma_{max,}$ and ϕ_0 were determined by fitting the diffusion equation to the experimental results for the armoured bubbles. The best fit line was found by the method of least sum of squared differences. The average relative error between the theoretical and experimental results was calculated at 0.31 % and some numerical instability is visible around 50 minutes mark when R_p is reached.

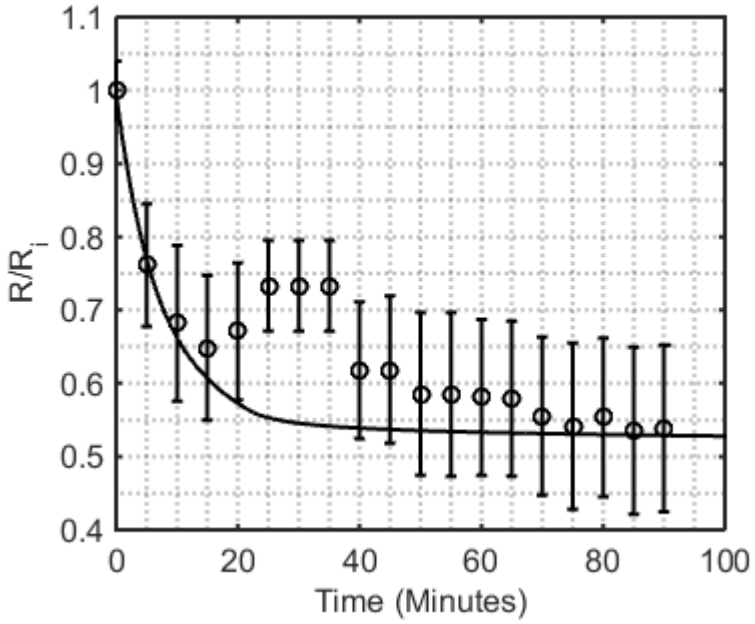

Figure 4.8 - Diffusion equation fitted to the experimental results for microbubbles coated with surfactant only. Initial particle concentration was set at ϕ_0=0.00 and the values of all other parameters can be found in Table 2.

The initial rate of shrinkage of surfactant-only microbubbles is shown in Figure 4.8 to be much faster than that of armoured bubbles. The experimental observations here, however, demonstrate a period of growth between 20 and 35 minutes. This trend is in direct contradiction to the expected sequence of events outlined earlier and is most likely due to interaction between multiple bubbles. Since the model does not account for such events, these points must be regarded as outliers when assessing

its validity. As the bubbles shrink further (between 40-90 minutes), their rate of dissolution is reduced considerably due to the increase in surfactant concentration on microbubbles' surface; reducing both diffusivity and interfacial tension which are the drivers of dissolution.

Equation (4.27) was solved for the results of the control experiment by setting ϕ_0 = 0.0 (i.e. no particles present on the bubble surface). Other parameters were not altered from those the nanoparticle-coated case, reflecting the identical protocol used to conduct the experiments. The theoretical model is able to describe most of the experimental points with an average error of 6.10%. The experimental readings between 25 and 35 minutes were considered outliers most likely due to some agglomeration of bubbles not accounted for by the model and consequently were not used in error calculations. This will be commented upon further at the end of this section.

Reasonable agreement is evident here between the theoretical and experimental results. The fact that such is achieved by running the simulations as to mimic the experimental procedure is of particular importance. While encouraging, the parameters values attained here must not be taken as quantitative properties of armoured/non-armoured coatings. This is largely due to two reasons: First, the nature of the model and second discrepancies between the assumptions made in deriving the model and the experimental procedure. Equation (4.23) contains various radius dependant terms which can be highly nonlinear. It may therefore be possible for various combinations of parameters to yield results which closely agree with experimental data. All parameters, bar the initial particle concentrations, were therefore fixed and kept identical for both cases prior to simulations in order to circumvent this issue.

It is finally necessary to comment on some of the discrepancies between the experimental results and the hypothesised behaviour. The model has been developed for a single microbubble suspended in an infinite under-saturated or saturated liquid. Gas will therefore always flow from bubble core to surrounding liquid, causing shrinkage in all cases and eventual disappearance where no coating is present. In both experiments there are instances of transient bubble growth which the model does not account for. This phase, particularly pronounced over the period from ~20

to ~40 minutes in the un-armoured case, can be attributed to the close proximity of the microbubbles on the glass slide. The observed growth of the unarmoured bubbles can, with a high degree of certainty, be attributed to Ostwald ripening of the microbubbles [212]. The polydispersity of these bubbles at t=0 is clearly evident from Figure 4.5a. As time goes on, smaller microbubbles will merge into larger ones in order to reduce the overall free energy of the system [213]. Ostwald ripening is also responsible for the large error bars present in Figure 4.8.

4.6.4. Notes

A number of additional assumptions were made in deriving (4.23) which should be noted here. In obtaining the relation between bubble radius and surface concentration, the transport of surfactants into the bulk liquid has not been included explicitly. This effect would, however, be implicit in the parameters fitted to experimental data for both surface tension and effective diffusion. The same is also true for the effect of surface "hardening" [214], when the surfactant molecules reach a critical packing density and provide a mechanical resistance to counter Laplace pressure similar to the particle jamming effect, has not been explicitly incorporated into the model. The exponential function proposed for the effective diffusion coefficient has not been verified explicitly against experiments designed purely for that purpose. There are unfortunately very few surfactants for which the relationship between the resistance to mass transfer and interfacial concentration has been characterised.

The bubble sizes considered here are larger than those which are relevant for medical applications but Equation (4.23) is valid for smaller bubbles down to a few 100 nm. Another important consideration in the case of biomedical agents is that they typically contain high molecular weight gases (e.g. perfluorocarbons) not naturally present in the body and these undergo substitution with dissolved gases in the blood following injection [215]. The model proposed here could, however, be modified to account for dissolution behaviour in a multi-gas environment. This would be achieved by writing the gas pressure inside the microbubble as the sum of the partial pressures of its various constituent species resulting in a new equation of state for each of the gases at the bubble boundary. Applying Henry's law would result in a concentration equation at the boundary and in the bulk liquid for each of the species

which could then be used to re-derive new forms of equation (4.23) and hence a new model consisting of a set of equations to describe the rate of change of bubble size.

4.7. Summary

The significant increase in the stability of nanoparticle coated bubbles observed in experiments is modelled through modification of the Epstein-Plesset equation for bubble dissolution. Several contributory mechanisms towards reduction and eventual termination of mass flux from the bubble into the surrounding liquid are considered. These are: the reduction of surface tension and increase of resistance to mass transfer with increasing concentration of surface active molecules; variation of surface area available for molecule diffusion with fractional nanoparticle coverage; and modification of local curvature as the result of continuing mass transfer after particle packing density is reached. The equation is rescaled by introducing non-dimensional variables to avoid numerical instability and solved using a numerical routine appropriate for stiff ODEs.

The new model is compared with experimental observations. Appropriate parameter values are selected from peer-reviewed literature where possible. Where parameters are unavailable, their value is limited to ranges through taking reasonable assumptions considering the experimental procedure. A good fit of the model to experimental data for armoured bubbles is produced through alteration of surfactant dependent constants for effective diffusion coefficient as well as the initial nanoparticle coverage on the interface. The experimental protocol is replicated by excluding terms relating to the particles from the model and leaving other parameters unaltered. Results amounted to a good description of control experiment.

The model successfully replicates the experimental results, vindicating the initially proposed stabilising mechanisms. It also shows some of these processes to be more effective than others during different stages of dissolution. Reduction in diffusivity, diffusion area, and interfacial tension play important roles at the beginning of dissolution process. A surfactant more resistant to gas permeation, for example, will prolong the time it takes for the bubble to reach its stable radius. The local modification of curvature plays the most important role is halting the dissolution process. Without this mechanism, the Laplace pressure at the interface would result in the model predicting further gas diffusion into the liquid at the “jamming” stage.

The parameter values presented here can only be taken as qualitative indicators since discrepancies between theoretical assumptions and experimental conditions prevent a fully quantitative comparison. Experimentally measuring parameters such as initial concentrations of surfactant molecules and nanoparticles on a single bubble is challenging; however experiments can be designed to more closely resemble the modelled conditions. These will be discussed further in the final chapter of this thesis.

5. Microfluidic Production of Microbubbles

5.1. Overview

Achieving consistent behaviour is an important milestone in the path to engineering and optimisation of microbubbles for any application. The theoretical work presented in the previous chapters has highlighted the need for controlled and repeatable experimental studies. It has also shown that small changes in factors such as surfactant properties can significantly alter the dynamics of microbubble oscillations.

The first step towards engineering microbubbles is to have the ability to control their size. A number of common fabrication methods were described briefly in section 2.4. The advent of microfluidic devices has brought about new methods of creating monodisperse populations of bubbles and droplets. There is a large body of research into droplet generation (liquid-liquid) using this method. The same cannot be said, however, about bubble fabrication (gas-liquid), particularly in terms of Computational Fluid Dynamic simulations (CFD). Fluid flows on the micro scale typically exhibit significantly different dependence on physical properties from those observed at macro scales. This chapter, therefore, begins with an overview of the physics of multiphase flows at the micro scale, followed by a review of three microfluidic devices commonly used in the production of droplets and bubbles.

The latter parts of this chapter are concerned with the study of two microfluidic devices: A cross flowing device (T-Junction) and the capillary embedded T-Junction which is a novel device developed and tested by project collaborators [216]. The models and various schemes used in the simulations are initially verified against peer reviewed and published experimental results. The significance of various parameters such as device geometry, phase viscosities, and flow rates are then studied using a computational fluid dynamics (CFD) model. In the last section the insights gained from investigations are used to provide recommendations for the production of microbubbles suitable for use for medical ultrasound applications.

5.2. Multiphase Flow at the Microscale

Fluid dynamics at the microscale differ considerably from those at the macroscale and further complexity arises when two phase flow is considered. These differences are particularly significant in developing appropriate computational models of microfluidic systems as will be undertaken later in the chapter. This section, therefore, provides an overview of key physical concepts and dimensionless parameters based on fundamental consideration of governing forces and how they interact.

5.2.1. Reynolds Number and Flow at Microscale

The Reynolds number (*Re*) of a flow is the ratio of inertial to viscous forces, often used to determine they type of fluid flow regime. In a cylindrical pipe it is given by:

$$\mathrm{Re} = \frac{\rho U d}{\mu}, \tag{5.1}$$

where ρ, μ, and U are respectively the density, dynamic viscosity, and characteristic velocity of the fluid, and d is the hydraulic diameter of the pipe. Flow can be categorised as laminar for $Re<2300$, transitional for $2300<Re<4000$, and fully turbulent for $Re>4000$. This definition has been widely used in the literature to determine the flow regime in liquid-liquid and liquid-gas flows with value of ρ set to the larger density of the two fluids. Shannak [217] has extended the above formulation for two phase flows in which a two phase *Re* is calculated by summing the inertial and viscous force contributions from both phases and taking their ratio. Moreover, studies on microflows have reported that flow transition in microchannels, with hydraulic diameters of the order of 10^{-4} m, may occur at lower values than expected. These studies propose critical *Re* values ranging from 300 to 2000 [218-220], although the strength of evidence for a transition limit below 1000 has been questioned [221].

While Reynolds number is the most significant dimensionless parameter in macro flows, it seldom becomes of importance in microfluidics. In this study, for example, flow velocity is of the order of 10^{-1} $ms^{-1}$and the channel sizes range from 10 to 100μm. In addition, the viscosity of the continuous phase ranges from 1.0 to 20.0 mPa.s and its density is of the order of 10^{3} kgm^{-3}. The value of *Re* will therefore

range from 10^{-6} to 10 which, according to all definitions, is well within the laminar regime.

5.2.2. Surface Tension at Phase Interface

Compared with single phase microfluidic flow problems, the primary modification brought about by introducing a new immiscible phase is the introduction of interfacial or surface tension. Surface tension acts to reduce the free energy of any surface by minimising its total area, leading to an unconstrained droplet or bubble adopting a spherical shape, whilst the shape of a confined bubble will also be determined by the surrounding walls. The pressure difference at the interface is described by the Young-Laplace pressure

$$p_{Laplace} = \sigma\left(\frac{1}{r_1}+\frac{1}{r_2}\right), \tag{5.2}$$

where r_1 and r_2 are the two principal radii of curvature, and σ is the interfacial tension between the two phases. The expression for p_{Laplace} as used in the previous chapters is recovered by assuming spherical symmetry. The presence of this additional pressure is important in determining the conditions under which bubble formation occurs.

5.2.3. Phase Viscosities

Since the immiscible fluids cannot be transported across the interface, new boundary conditions are introduced. The local normal component of the velocity in each fluid must be equal to the interface velocity. The velocities tangent to the interface must also be equal on either side of the droplet/bubble. Similarly, the tangential shear stresses must be balanced at the interface when it is clean of contaminants. This means that the variation of the tangential velocity $u_{\|}$ with respect to normal direction, r, inside and outside of the interface must obey

$$\mu_{disp}\left.\frac{\partial u_{\|}}{\partial r}\right|_{disp} = \mu_{cont}\left.\frac{\partial u_{\|}}{\partial r}\right|_{cont}, \tag{5.3}$$

where μ is dynamic viscosity, and subscripts *disp* and *cont* refer to the dispersed and continuous phases. This signifies the importance of the difference between the phase

viscosities in determining the velocity field inside and outside of a moving droplet or bubble, and is expressed through the viscosity ratio $\lambda = \mu_{cont} / \mu_{disp}$.

5.2.4. Capillary Number

The competition between the viscous shear force and surface tension is expressed through the dimensionless capillary number:

$$Ca = \frac{\mu U}{\sigma} \tag{5.4}$$

where μ is the larger viscosity of the two fluids, U is the characteristic velocity, and σ is the interfacial tension. A low value of Ca therefore indicates the dominance of interfacial tension. Bubbles formed under such conditions tend to adopt a spherical shape corresponding to minimum surface area. High Ca in turn corresponds to dominance of viscosity in which case bubbles may adopt non-spherical shapes.

5.2.5. Bond Number and Weber Number

The influence of gravity upon microfluidic flows is evaluated by the Bond number (*Bo*) which is the ratio of gravitational to capillary force and is given by

$$Bo = \frac{\Delta\rho g l^2}{\sigma}, \tag{5.5}$$

where $\Delta\rho$ is the difference in fluid densities, g is the gravitational acceleration, σ is surface tension, and l is the characteristic length.

The Weber number (*We*) can be used to assess the significance of inertia compared to surface tension and is given by

$$We = \frac{\rho U^2 l}{\sigma}, \tag{5.6}$$

where ρ is the density of the carrier fluid, σ is surface tension, and l and U are respectively the characteristic length and velocity scales. The values of *Bo* and *We* tend to be <<1 in microfluidic devices given their length scale being in the order of 10^{-4} m and maximum flow velocities in the order of 10^{-1} m/s. In microfluidics, therefore, gravity and fluid inertia do not have a significant influence upon flow characteristics.

5.2.6. Channel Geometry and Operating Conditions

Flow characteristics are dependent on a number of other parameters, in particular the relative phase velocities and flow rates ($U_r=U_{disp}/U_{cont}$ and $Q_r=Q_{disp}/Q_{cont}$ respectively), as well as the relative dimensions of microfluidic channels ($\Lambda=w_{in}/w_{out}$). Subscripts *cont* and *disp* respectively refer to the continuous (i.e. the carrier fluid) and dispersed phases of the multiphase flow. *w* is the characteristic width of a channel and subscripts *in* and *out* in respectively refer to the width of the entry point of dispersed phase and width of the channel where the two fluids mix. In more complex geometries, such as flow focusing devices (see 5.3.3.), more than one geometrical ratio will affect the outcome.

5.3. Passive Production of Microbubbles

5.3.1. Co-Axial Flow Devices

Devices utilising co-axial streams for bubble or droplet production consist of an inner tube in coaxial arrangement with another channel, usually of square or rectangular cross section. The physics of drop formation at the capillary tip in a liquid-liquid system were studied by Cramer *et al.* [222]. They showed that drop breakup in these devices, as demonstrated in Figure 5.1, can be separated into two regimes: dripping and jetting.

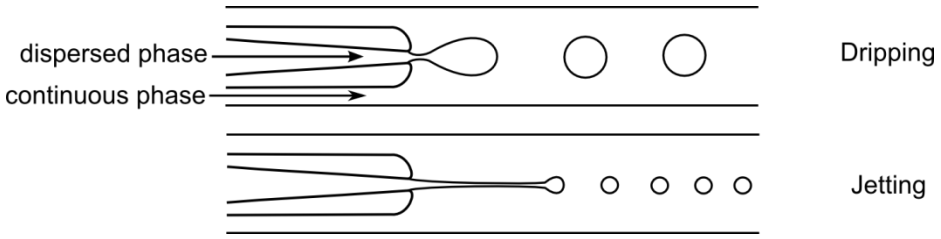

Figure 5.1 Schematics of a co-axial flow device and different flow regimes. The dispersed phase is injected into the continuous phase through an inner tube.

The dripping regime refers to the situation when the dispersed phase flow breaks up close to the capillary tip. Jetting occurs when the dispersed phase extends further into the main channel and forms a filament upstream of the capillary tip from which drops break off. The continuous phase flow velocity at which this transition occurs is termed the 'critical velocity'. In general, the detachment rate of the drops increases with the velocity of the continuous phase and results in smaller drop diameters. This

relationship is illustrated in Figure 5.2, where the dripping-to-jetting transition region is signified by the sudden decrease in drop diameter.

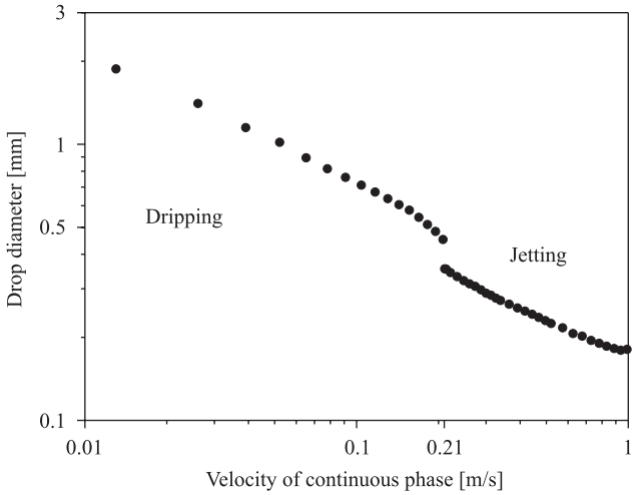

Figure 5.2 - Droplet diameter against the velocity of the continuous phase as obtained by Cramer *et. al.* [222]. The flow rate of the dispersed phase was set at 0.25 ml/min. The viscosities of the continuous and dispersed phases were 38.0 and 37.0 mPa.s respectively.

For a given viscosity ratio and interfacial tension, the critical velocity increases with decreasing dispersed flow rate [222]. Flow transition into jetting at low dispersed flow rates is thus inhibited, regardless of the continuous phase flow rate. Conversely, at high disperse flow rates, jetting may occur even in a quiescent continuous phase [223]. In a more comprehensive study, Utada *et al.* [224] found jet formation to be dependent on the Capillary number (*Ca*) of the continuous phase ($Ca_{cont.}$). When $Ca_{cont.}<1.0$, surface tension between the phases dominates and the continuous phase cannot drag the dispersed phase out to form the jet. Conversely, when $Ca_{cont.}\geq 1.0$, the shear stress exerted by the continuous phase is large enough to drag the dispersed phase downstream and form the jet. The diameter of this jet is initially equal to the tip of the capillary and decreases as it protrudes further downstream but ultimately reaches a constant value. The diameters of the droplets formed in this regime were found to be the same order as that of the jet itself.

5.3.2. Cross-Flowing Devices

Cross-flowing devices, commonly known as T-junctions because of their shape, consist of two orthogonal flow channels. Their first reported use was by Thorsen *et al.* [225] who generated water droplets in a variety of oils.

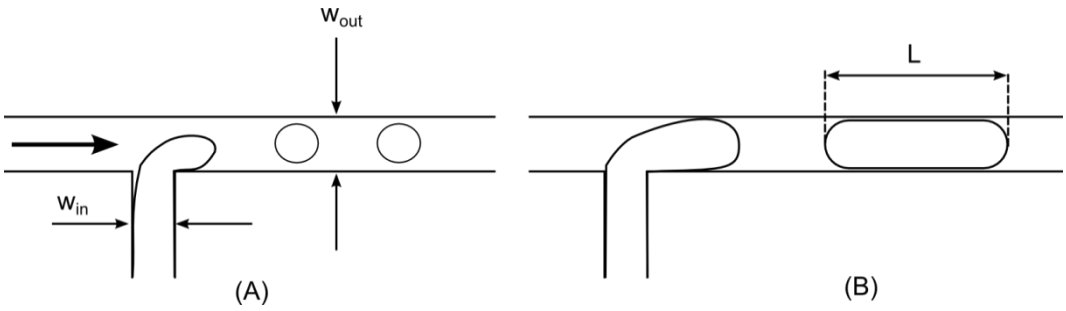

Figure 5.3 Example of a T-Junction and droplet breakup regimes: a) Dripping (Bubbly flow); b) Squeezing (Slug flow).

In these devices, droplets or bubbles are formed where the two channels meet. The mechanisms of droplet generation in T-Junctions can be divided into two main regimes of Dripping and Squeezing. Dripping, as demonstrated in Figure 5.3a, refers to a shear driven breakup mechanism whereby the gas stream is pinched off before it fills the entire channel. Squeezing refers to a regime where gas stream grows to fill the entire width of the channel (Figure 5.3b). The obstruction causes an increase in the dynamic pressure upstream of the bubble, thus forcing the interface to initially neck and eventually the bubble to pinch off.

5.3.3. Flow Focusing Devices

In a flow focusing device, such as the one illustrated in Figure 5.4, the dispersed phase in squeezed into an orifice by two counter flowing streams of the continuous phase. A very early version of this device for production of highly monodisperse microbubbles was first developed by Alfonso and Gordillo [226] using capillary tubes.

The geometry was later integrated into a microfluidic chip and studies on droplet generation were conducted by Anna *et al.* [227] and Dreyfus *et al.* [228] who identified four main breakup regimes as the parameters were varied: squeezing, dripping, jetting, and thread formation. The large number of geometrical aspect ratios have meant that developing simple scaling laws for these devices is difficult,

although there have been some attempts by Garstecki *et al.* [229] and Dollet *et al.* [230].

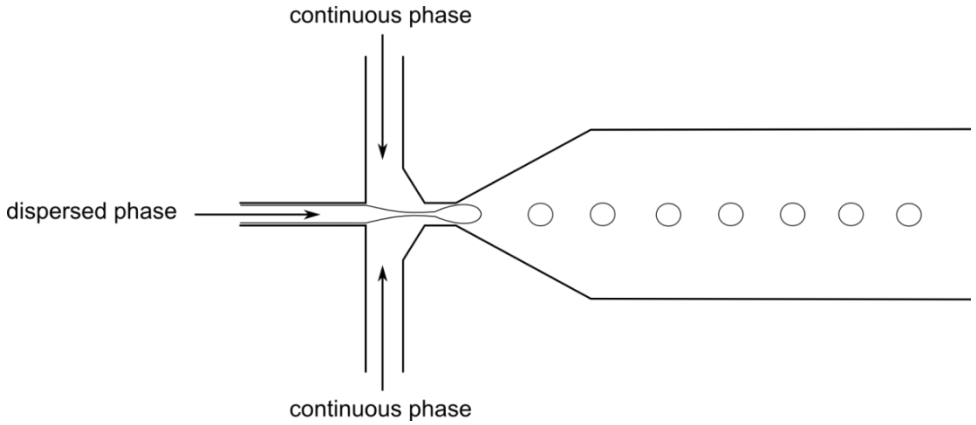

Figure 5.4 An example of a Flow Focusing Device with two continuous phase inlets and an expanding outlet.

5.4. Numerical Modelling Method

The previous section discussed the characteristics of microfluidic devices most commonly used in droplet and bubble fabrication, as well as the parameters affecting their operation. The influence of operational parameters upon microbubble generation in two microfluidic devices is presented in later sections using CFD simulations. While such studies have been conducted widely for liquid-liquid systems, the same cannot be said for gas-liquid systems. It is therefore appropriate to validate the simulation method beforehand using available published data and this is the aim of the following section.

5.4.1. Computational Model

Numerical simulations of microbubble production were conducted using the ANSYS Workbench 13.0 (ANSYS Inc., USA) software package. Fluid domains were sketched in 3D using ANSYS Design Modeller and meshed in ANSYS Mesher. All geometries were meshed using a hexahedral strategy in order to increase the orthogonally of the mesh as well as reducing the number of mesh elements.

The flow in microchannels was modelled using a transient pressure based solver in ANSYS FLUENT. The fluids for the primary and secondary phases were set as gas and liquid respectively with surface tension and wall adhesion options turned on. The boundary types for the inlets and outlet were set as Velocity and Outflow

respectively. The explicit Volume of Fluid (VOF) model [231] with implicit body force option was used for the multiphase flow formulation.

The solver was set as pressure based and transient. The transient formulation was set as first order implicit with non-iterative time advancement and Pressure-velocity coupling was done using the PISO algorithm. Pressure, momentum, and volume fraction were respectively discretised using the Pressure Staggering Option (PRESTO!), Second Order Upwind, and Piecewise Linear Interface Construction (Geo-Reconstruct). The fluid domain was initially filled with the liquid phase via the Patch tool.

The use of an explicit scheme here requires that the solver parameters meet the Courant-Friedrichs-Lewy (CFL) condition [232] for convergence. This is given by

$$C = \frac{u\Delta t}{\Delta x} \leq 1.0, \tag{5.7}$$

where C is a dimensionless parameter termed Courant number, u is the flow velocity, Δt is the time step, and Δx is the node spacing. The maximum global Courant number was therefore set at 0.95 and controlled by the program using variable time steps.

Two dimensional modelling of three dimensional systems is common practice in fluid flow problems where axisymmetric assumptions can be justified. This was found, however, to yield inaccurate results during development and testing of the CFD simulations. Consider the case of bubble break-off in a T-Junction. Surface tension, in the form of Laplace pressure, is an important factor in the “pinch off” process after necking has occurred. There can be conditions, such as that demonstrated in Figure 5.6, where the interface appears flat in the two dimensional view. Since this surface curvature in a two dimensional system only exists in one plane, the Laplace pressure will be very small within the simulation. This manifests in significant retardation of the pinching process and considerable difference between the results from the model and that of the experiments. Considering this case in three dimensions, however, it is immediately obvious that the interface is curved on the orthogonal plane due to hydrodynamic forces and wetting of the walls by the continuous phase. The existence of this curvature results in eventual collapse

of the interface and break-off. All of the studies presented in this chapter were, therefore, conducted in three dimensions.

5.4.2. Model Verification against Experimental Results

Numerical model and solver settings were tested against the published experimental observations of Santos and Kawaji [233] for verification. Fluid domain dimensions and the associated mesh structure are illustrated in Figure 5.5.

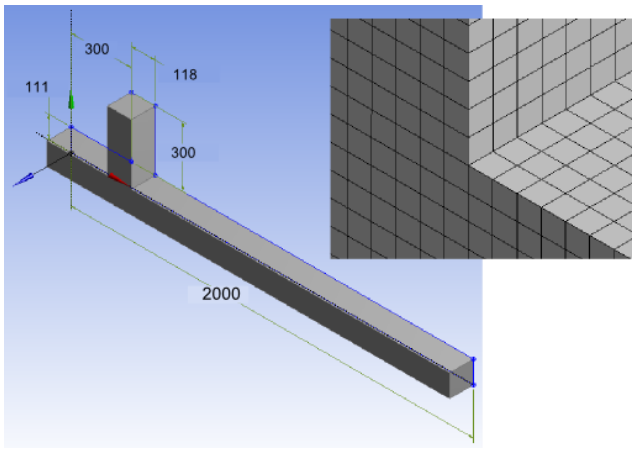

Figure 5.5 Fluid domain and hexahedral mesh detail used in modelling the T-Junction used in simulating the observations in [233]. (Dimensions in µm)

The continuous and dispersed phases were set to water (ρ_l = 998.2 kgm^{-3} μ_l = 1.002 mPa.s) and air (ρ_g = 1.20 kgm^{-3} μ_g = 0.18 mPa.s) respectively with an interfacial tension of 0.072 Nm^{-1} and wall contact angle of 36°. Phase velocities corresponding to the slug flow regime observed by Santos and Kawaji [233] were set to U_l = 0.336 ms^{-1} and U_g = 0.317 ms^{-1}. The optimum mesh size was determined by initially conducting simulations with identical boundary conditions, as set out above, on geometries with uniform hexahedral mesh sizes of 10 µm, 5 µm, 4 µm, and 3.7 µm. The simulations were set to terminate automatically at the simulation time of 5.0 ms. Slug length measurements were performed on images with identical resolutions using the open source imaging software GIMP. Independence from grid was then assessed by comparing the change of slug length between consecutive configurations. The results, shown in Table 3, show a change of 0.34% between 4 µm and 3.7 µm mesh grids and the latter was thus deemed suitable for T-Junction simulations.

Mesh Size [µm]	Simulation result at 5.0 ms	Length [µm]	% Change
10.0	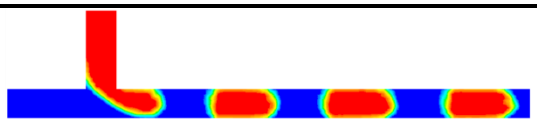	250.3	N/A
5.0	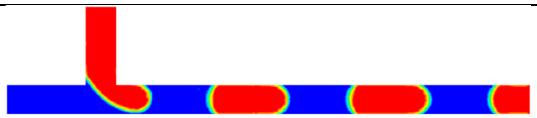	304.7	21.74
4.0	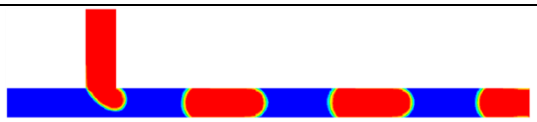	322.1	5.71
3.7	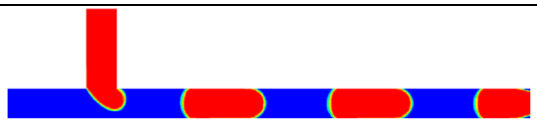	323.2	0.34

Table 3 – Grid independence studies for a T-Junction, the dimensions of which can be found in Figure 5.5. Mesh size here refers to the node spacing in a hexahedral grid and the %change in each case was calculated relative to the slug length measured in the previous case. The continuous phase (blue) was set as water (ρ_l = 998.2 kgm-3 μ_l = 1.002 mPa.s) with flow velocity U_l = 0.5 ms^{-1}, and the dispersed phase (red) is air (ρg = 1.20 kgm-3 μg = 0.18 mPa.s) with flow velocity U_g = 0.5 ms^{-1}.

The result for breaking slug formation is demonstrated in Figure 5.6. The simulation results here show good reproduction of the breakup process when compared against the published images in [233]. The slug lengths were measured using GIMP and a difference of 2.3% was recorded. The VOF model was thus deemed suitable for the simulation of gas/liquid microflow patterns. This setup is used in the next sections of this chapter for parametric studies of multiple geometries.

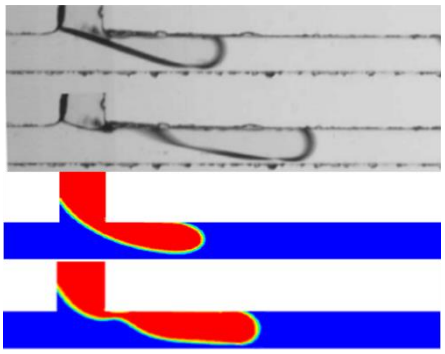

Figure 5.6 Comparison between simulations and observations in [233]: Breaking slug formation (U_l = 0.336 ms^{-1}, U_g = 0.317 ms^{-1})

5.5. T-Junction Sensitivity Studies

5.5.1. Solution Domain and Boundary Conditions

A T-Junction with an overall length of 1.5mm and 0.1×0.1mm cross section was considered as the standard case. A schematic of this domain and its dimensions is illustrated in Figure 5.7.

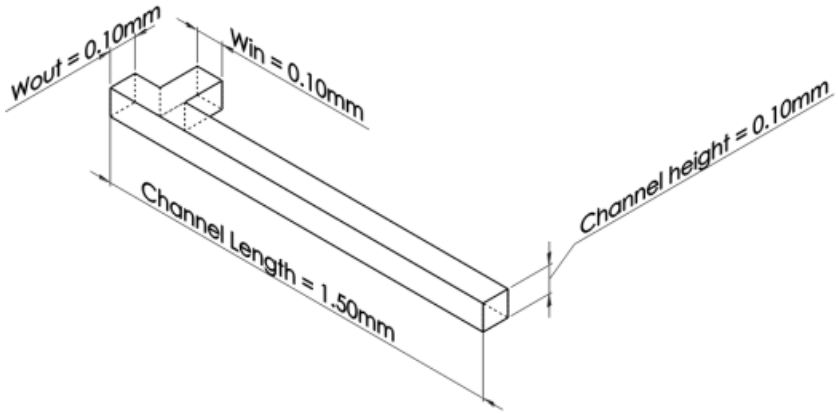

Figure 5.7 Illustration of the standard fluid domain used in the parametric studies.

The working fluids for the continuous and dispersed phases were respectively defined as water and air with the same material properties as those described in 5.4.2. The inlets were modelled as velocity inlets with a uniform velocity profile. The outlet was modelled as as an outflow with a pressure of 101325 Pa. The velocity of the continuous phase at the inlet in all cases was set at U_l=0.5 ms^{-1} and wall contact angle was set to 1° with no-slip boundary condition.

5.5.2. Effect of Channel Size

The influence of channel size upon the size and formation regime of bubbles was studied in four configurations. Apart from the standard case, where the widths of the inlet and outlet channels are equal (Figure 5.7), three new configurations with width ratios (Λ) of 0.25, 0.5, 0.75 were obtained by modifying the dimension w_{in}. In each case, the channel height was set equal to w_{in}, thereby preserving the aspect ratio of the dispersed phase inlet channel. The flow velocity ratio was set at U_r = 0.8. The meshing for the smallest channel width was refined to 2.0 μm in order to preserve accuracy.

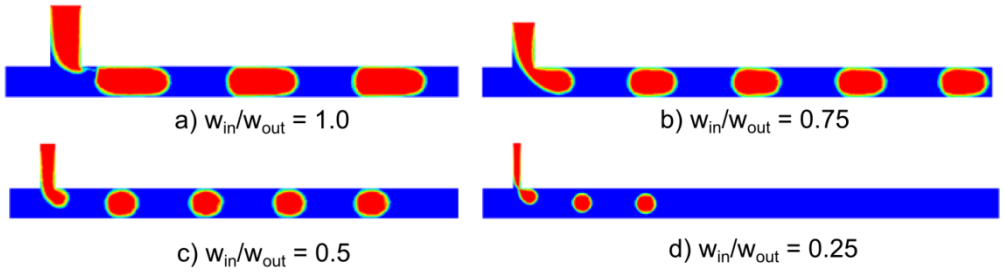

Figure 5.8 – Influence of the change in channel width ratios on the pinch off process. w_{out} = 0.1mm for all cases and channel height is equal to w_{in}. It is clear that as the width ratio decreases, there is a transition from squeezing (a) to dripping (d) regimes.

The results shown in Figure 5.8 clearly demonstrate the effect of width ratio upon flow transition from slug to bubbly flow. It is evident that the flow transition occurs when w_{in}/w_{out} = 0.5. This result directly reflects the prediction of Garstecki *et al.* [234] who, for the same capillary number, estimated the width ratios at which the transition from squeezing to dripping regimes occurs. When $w_{in}/w_{out} \geq 0.5$, the bubble fills the entire channel and the pinch off process is shear dominated. For $w_{in}/w_{out} < 0.5$ the shear stress greatly distorts the bubble tip before it fills the entire channel and eventually results in pinching off.

5.5.3. Effect of Viscosity and Flow Rate

The influence of the continuous phase viscosity and relative flow rates upon microbubble size were simulated for 5 values of viscosity at 5 relative flow rates, giving a total of 25 cases. The standard geometry (w_{in}= 100.0 µm, w_{out} = 100.0 µm) was used for all cases in this study. The viscosity of the continuous phase was varied between 1.002 mPa.s and 20.0 mPa.s for ranges of U_r between 0.5 and 1.5. The value of U_r was changed by keeping U_l constant at 0.5 ms^{-1} and varying U_g. Slug lengths were measured by pixel analysis on high definition images using the measurement tool in GIMP imaging manipulation software.

Slug lengths were normalized against w_{out} and plotted against U_r (Figure 5.9). A clear linear relationship between the slug length and flow rate ratios is apparent. These agree well with the findings in [234] where the same relation was observed for droplets of water in oil for $U_r \geq 0.5$. The results of the simulations can also be organized in terms of the *Ca* for various flow ratios. The trend seems to show that for a given flow rate ratio, there is a viscosity limit after which the size of the bubble produced is not reduced further.

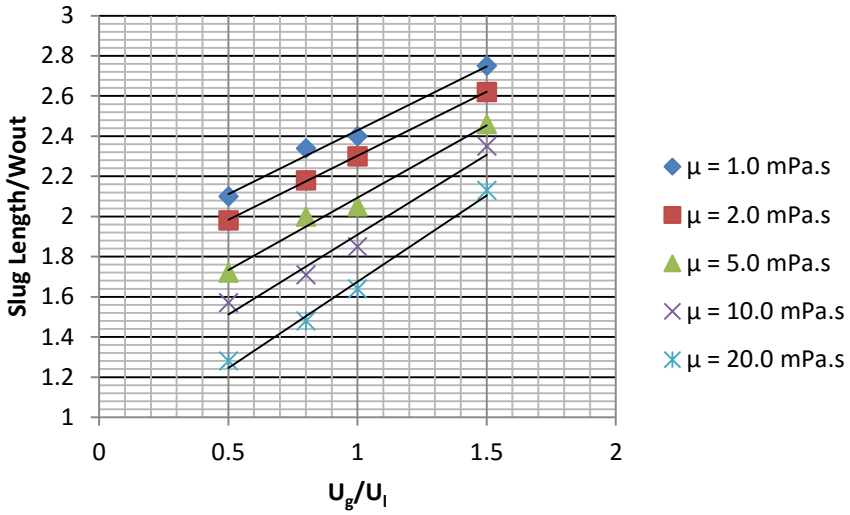

Figure 5.9 – The variation of slug length with flow rate ratios for various viscosities of the continuous phase. The standard geometry was used in all cases and the continuous phase flow velocity vas set to U_l=0.5 ms^{-1}. Viscosity was varied as multiplies to that of water (μ=1.002 mPa.s).

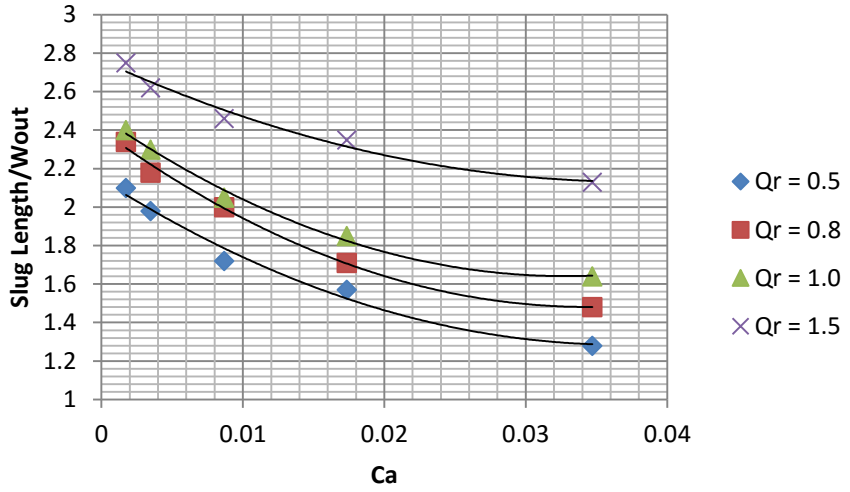

Figure 5.10 – Normalised slug length as function of Capillary number for various flow ratios. The standard geometry was used as the continuous phase velocity was set at U_l=0.5 ms^{-1}. Changes in Capillary number are as a result of variation in the viscosity of the continuous phase.

Perhaps the most important conclusion of this section is that the size of bubbles produced using the T-Junction is highly constrained by its geometry. Devices with channel sizes required to fabricate microbubbles of the size used in medical applications, however, are susceptible to failure due to blockages. It is, additionally, particularly difficult operate these devices at high flow rates and/or with highly viscous liquids. The implications of the findings in this section are discussed in more detail at the end of this chapter.

5.6. Capillary Embedded T-Junction

5.6.1. Device Setup

Pancholi *et al.* [97,235] proposed a novel low cost method of microbubble fabrication using microcapillary tubes. The device consists of a polymer block with two orthogonal channels drilled into it. Three capillaries of fixed outer diameter are inserted into these conduits to form a "T" shaped mixing region (Figure 5.11).

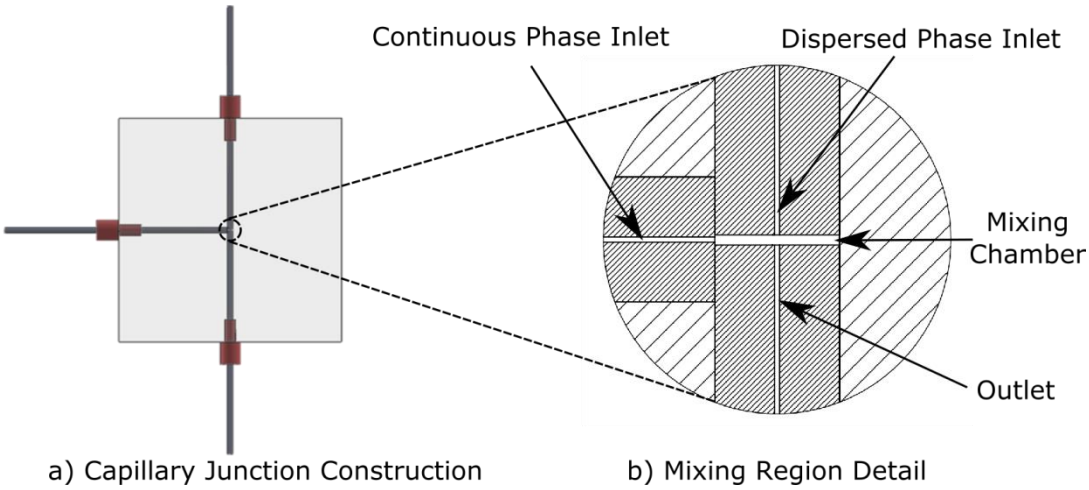

Figure 5.11 a) An overall schematic of the Capillary T-Junction. The capillaries are inserted into a polymer block into which two orthogonal channels are drilled. b) Detail view of the mixing region where the capillaries meet. The finely hashed region here denotes the capillary tubes which have a larger outer diameter compared to their inner conduit. The region with coarse hash denotes the polymer block.

The construction provides a low maintenance system for microbubble/droplet production. Blocked capillaries can be swapped for new ones at the point of failure and no special cleaning or replacement of the entire junction is required. The design also allows rapid geometry modifications by using tubes of different inner diameter in a multitude of arrangements.

The fluid domain thus created differs significantly from the T-Junction presented earlier. This has been confirmed in experimental observations [216]. There have been very limited theoretical studies of this type of junction carried out to date and this section is an initial attempt to gain an insight into the formation of microbubbles in such a device.

5.6.2. Simulation Setup

Solution Domain

A scale drawing of the fluid domain in the capillary T-Junction and the one used in simulations are shown in Figure 5.12a. The capillaries have very large inner to outer diameter ratios. This in turn creates a large disc shape within the fluid domain. All meshing was carried out in ANSYS ICEM CFD 13.0 (Ansys Inc.) which provides flexible tools for meshing complex geometries. The curved interface between the orthogonal channel and the mixing chamber, however, was found to be particularly sensitive to the chosen mesh grid. Obtaining an effective and efficient mesh grid, therefore, necessitated a number of modifications to the domain geometry. The result of these modifications is illustrated in Figure 5.12b where the mixing chamber and the continuous phase inlet cross-sections have been changed from circular to rectangular. These modifications were thought to have minimal impact on the operational characteristics of the device. The interaction between the phases takes place in the centre of the mixing chamber at the dispersed phase inlet and mixture outlet. The width of the mixing chamber is more than 10 times the diameter of the dispersed phase inlet and outlet, thereby rendering wall effects insignificant. Similarly, the continuous phase inlet is deemed sufficiently far from the centre of the mixing chamber for its shape not to affect the flow profile at the mouth of the outlet.

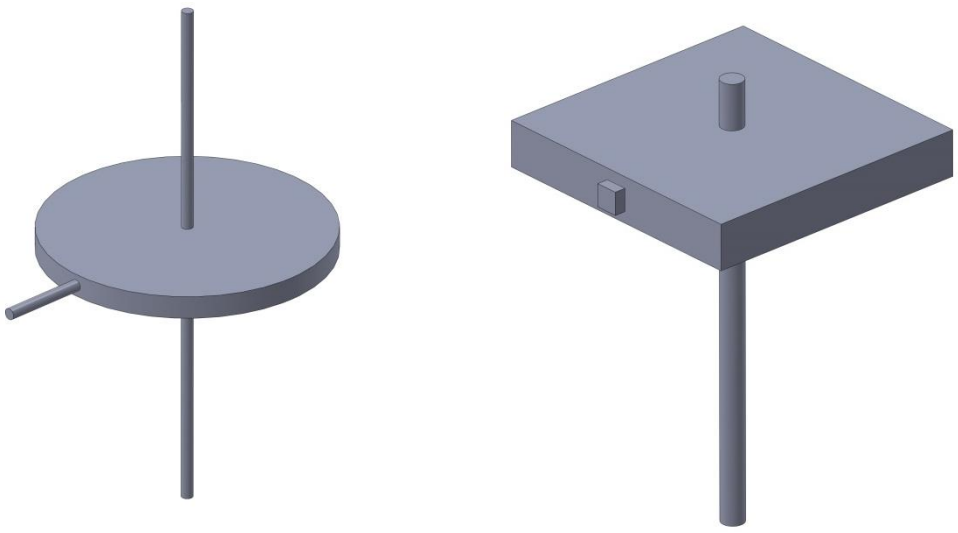

(a) (b)

Figure 5.12 – a) Isometric view of the fluid domain of the capillary T-Junction of 100 µm inner diameter. b) The simulation domain with rectangular mixing chamber and continuous phase inlet. The dispersed phase inlet and the outlet remain circular.

Operational Parameters

In addition to the operational parameters common with other microfluidic devices, such as viscosity and flow rate ratio between the phases and internal capillary diameter, the design of the CETJ allows for the height of the mixing chamber to be altered. This creates a very large parameter space, the exploration of which in its entirety is unfeasible and thus necessitates setting a number of restrictions. In the simulations that follow, the internal capillary diameters were fixed at 100.0 μm and the mixing chamber width was set at 1.2 mm. The viscosity and surface tension properties of the continuous phase were set according to the measurements provided by Parhizkar *et al.* [216] which are given in Table 4.

Aqueous solution [glycerol / SLS]	**Viscosity (μ) [mPa.s]**	**Surface tension (σ) [mNm^{-1}]**
5.00 wt.% / 1.0 wt.%	1.2	50.0
35.0 wt.% / 1.0 wt.%	3.0	55.0
50.0 wt.% / 1.0 wt.%	6.0	56.0
60.0 wt.% / 1.0 wt.%	10.8	57.0
70.0 wt.% / 1.0 wt.%	22.5	58.0

Table 4 – Bulk viscosity and surface tension properties of the aqueous solution, as measured by Parhizkar *et al.* [216], used as the continuous phase in the simulations. The solutions were prepared by diluting 99% purity glycerol to various degrees and addition of equal amount of sodium lauryl sulphate (SLS) to each solution.

Unless otherwise specified, in the simulations that follow, U_{cont} was set at 0.5 ms^{-1} (Q_{cont} = 0.03 ml/min) and the height of the chamber was 200.0 μm.

5.6.3. Bubble Formation Process and the Effect of Flow Rate Ratio

Figure 5.13 shows the results for a viscosity of 1.2 mPa.s and different flow rate ratios, obtained by increasing the gas flow rate relative to that of the continuous phase.

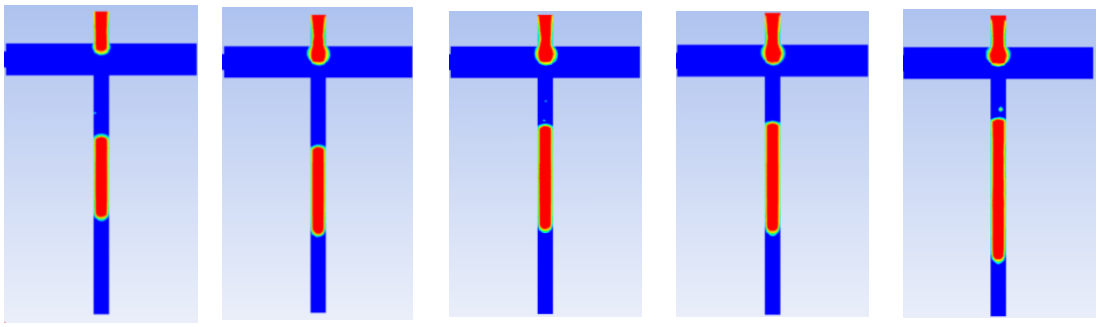

Q_r = 0.25 Q_r = 0.5 Q_r = 0.75 Q_r = 1.0 Q_r = 1. 5

(a)

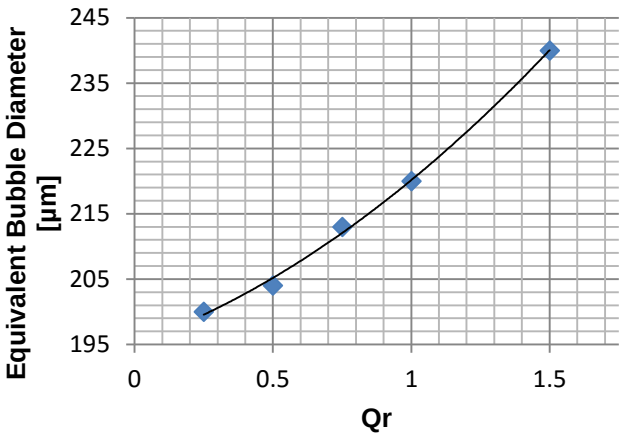

(b)

Figure 5.13 – The effect of flow rate ratios upon slug length in CETJ. a) Simulation results for various dispersed to continuous phase flow rate ratios. b) Equivalent bubble diameters calculated from the slug length measurements in (a) against flow rate ratios.

The length of the slug increases with flow rate ratio as anticipated. The change is clearer when the volume is measured and then converted into bubble radius (Figure 5.13b). These results can perhaps be better understood by looking at the bubble formation process in the CETJ, as shown in Figure 5.14 for the case of Q_r = 1.0 in Figure 5.13a. When the dispersed phase first reaches the mixing chamber, it expands into a spherical shape or a "bulb" (Figure 5.14a) and grows until it reaches the outlet (Figure 5.14b). The bulb is then dragged into the outlet due to the strong flow at its mouth (Figure 5.14c) and pinch off eventually occurs due to mechanism similar to the squeezing regime previously discussed for the T-Junction (Figure 5.14d). The

interface then retracts fully back up to the inlet and the process starts again (Figure 5.14e).

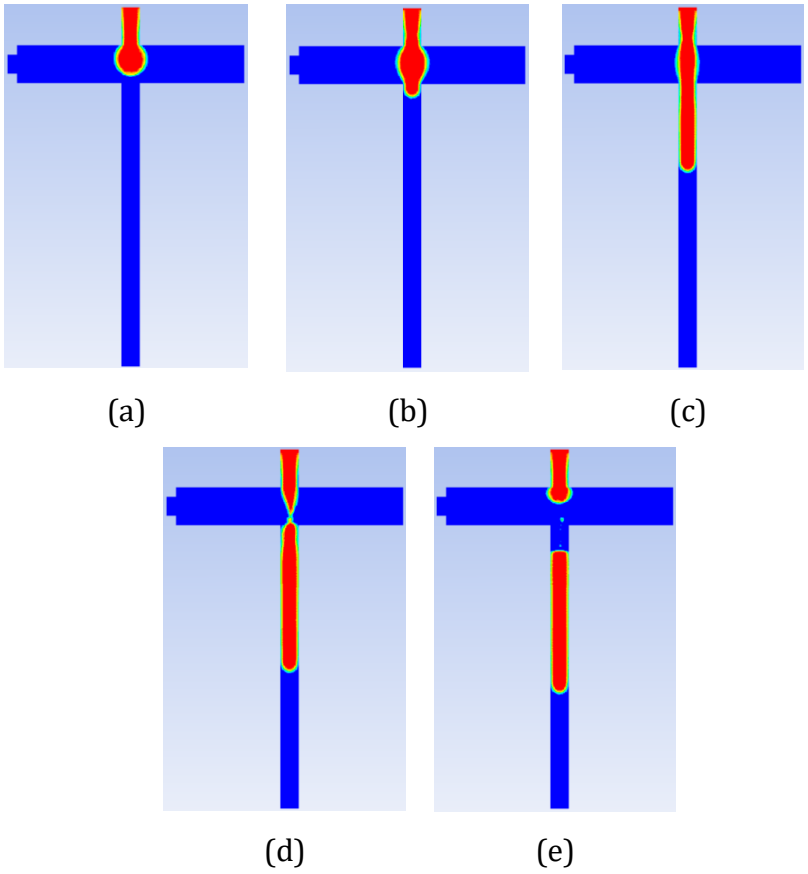

Figure 5.14 – Bubble formation process in the CETJ. a) Expansion of gas "bulb" in the mixing chamber. b) "Bulb" drawn into the outlet conduit. c) Distortion of the "bulb" into a slug and start of the pinch off process. d) Completion of the pinch off process and the formation of a gas slug. e) Formation of a slug and retraction of the interface due to interfacial tension.

The bulbs which are created in the chamber reach the same maximum size in all above cases, although it is not shown here. Similarly, for a fixed liquid flow rate, the time it takes for the bulb to get dragged into the outlet and be pinched off decreases with decreasing disperse flow rate. This was approximately calculated at 0.5 ms by taking the difference in the timestamps from the simulation output at the aforementioned stages. Hence as the gas flow rate increases, there will be more gas entering the outlet conduit before pinch off leading to a variation in slug length. In addition, at lower gas flow rates, it takes longer for the bulb to grow down to the outlet and hence the pinch off frequency drops. Thus, for the cases displayed in Figure 5.13, the approximate rate of bubbles produced for Q_r = 0.25 to 1.5 were respectively 20, 35, 46, 55, and 69 thousand bubbles per minute.

5.6.4. Effect of Mixing Chamber Height

Parhizkar *et al.* [216] do not investigate the effect of chamber height on bubble sizes. Precise setting of this parameter in the experiments is somewhat difficult using the current setup. Having conducted a number of simulations, however, it became clear that this parameter can significantly affect the size of the bubbles produced. Figure 5.15 illustrates the results for CETJs with three different chamber heights and otherwise identical operating conditions. The viscosity of the continuous phase here was set at 1.2 mPa.s and Q_r = 1.0.

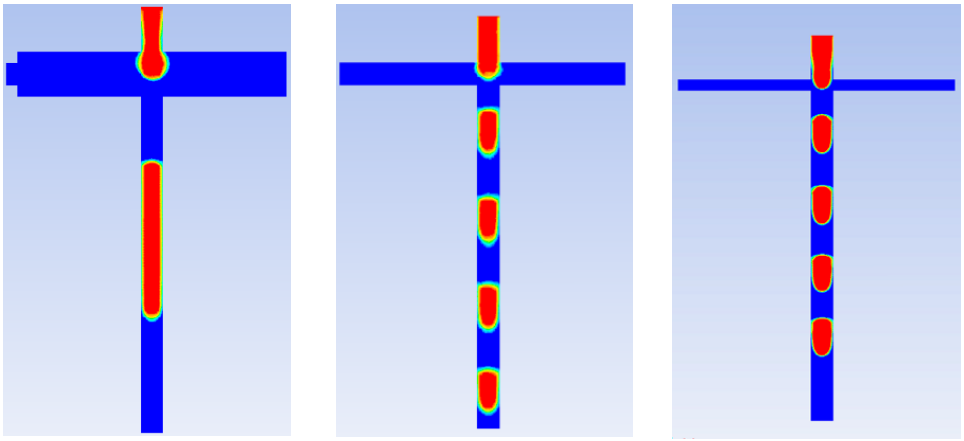

(a) (b) (c)

Figure 5.15 – Side by side comparison of the effect of the mixing chamber heights (and resulting bubble diameters) of: (a) 200.0 µm (240.0 µm), (b) 100.0 µm (140.0 µm), and (c) 50.0 µm (100.0 µm) on bubble sizes.

As may be seen, the smaller the chamber height, the shorter the distance the gas column can penetrate before entering the outlet and the more rapid the pinch off process leading to smaller bubbles. In the cases shown here, there was an approximately 30.0% reduction in relative bubble size for 50.0% relative reduction of the chamber height. While this demonstrates the chamber height to be an effective parameter in controlling bubble size, there will be a limit to its value in practice which will be discussed further at the end of this chapter.

5.6.5. The Onset of "Jet" Formation

In sections 5.6.3 and 5.6.4, the bubble formation regime in all cases was a hybrid of the dripping flow in the co-axial devices, as discussed in 5.3.1; and squeezing flow in the cross flow devices, as discussed in 5.3.2. The similarity to former flow regime is in the interface rebounding back up to the dispersed phase inlet and to the latter in the dispersed phase needing to fill up the outlet conduit prior to pinch off. Another characteristic of this formation regime was the apparent non-chaotic nature of the flow, resulting in formation of identical sized bubbles. Further investigation of the parameter space indicated that, following a transitional phase, a different break-off regime, analogous to jetting in co-flowing streams could observed for different combinations of liquid viscosity and flow rate ratio.

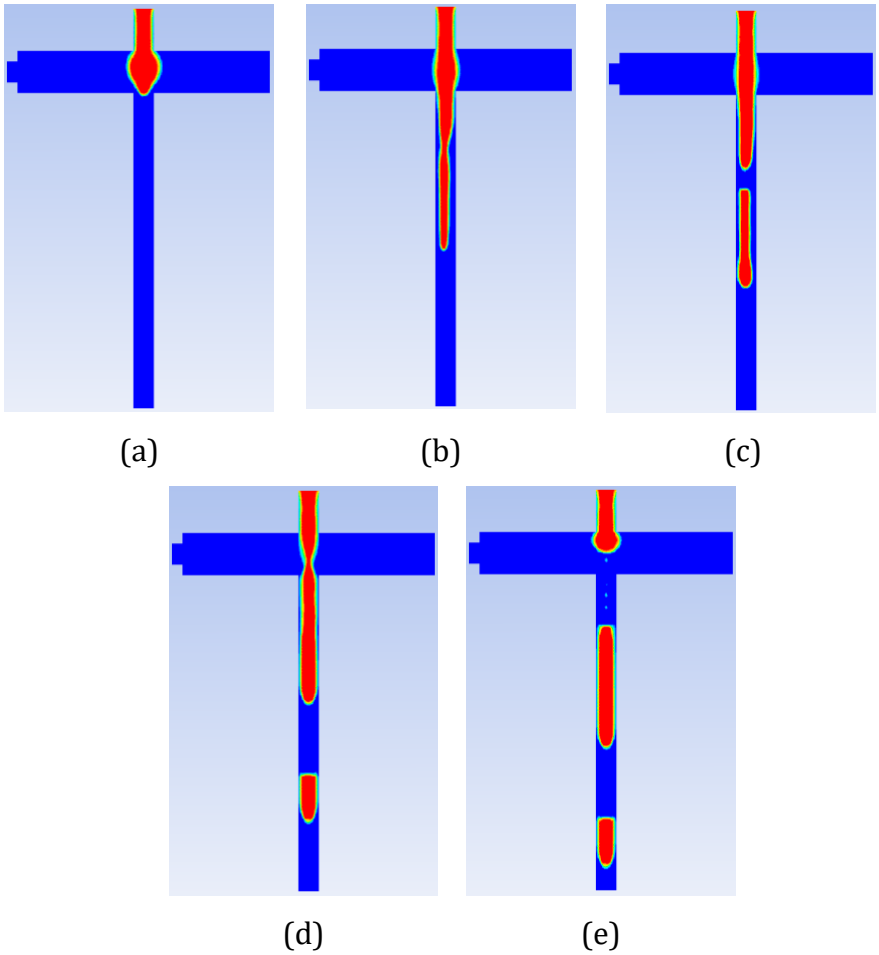

Figure 5.16 – Transitional flow behaviour of the CETJ (μ_{cont} = 6.0 mPa.s, U_{cont} = 0.5 ms^{-1}, Q_r = 1.0). a) After expansion into the mixing chamber, the bulb is dragged into the outlet conduit. b) The dispersed phase is stretched into a thread and a neck appears in the outlet. c) The thread breaks up downstream from the mixing chamber as another neck appears in the mixing chamber. d) The second pinch off is completed and the interface rebounds towards the dispersed phase inlet.

Figure 5.16 illustrates a case of transitional flow for the flow parameters of μ_{cont} = 6.0 mPa.s, U_{cont} = 0.5 ms^{-1}, and Q_r = 1.0. After expansion into the mixing chamber (Figure 5.16a), the higher shear force, due to higher continuous phase viscosity, causes the dispersed phase to be drawn into the outlet conduit and form a thread (Figure 5.16b). As the thread stretches into the outlet, an initial neck appears downstream from the mixing chamber and thus a small bubble is pinched off (Figure 5.16c). The bulb in the mixing chamber is finally squeezed to create a second, larger, bubble (Figure 5.16d). The gas interface then rebounds towards the dispersed phase inlet when the interfacial tension takes over (Figure 5.16e) and the process starts again.

The transitional phase demonstrated above was akin to the transitional phase in the co-flowing devices, where the hydrodynamic forces are not large enough to overcome the surface tension force. Upon increasing the continuous phase viscosity further, a new flow regime similar to "jetting" flow in co-flowing devices appears. The shear driven process in the jetting regime, as displayed in Figure 5.17, is immediately apparent during the formation of the gas bulb where the surface is deformed prior to its entry into the outflow capillary eventually forming a jet. Bubbles are formed at the tip of the jet and are eventually sheared off. In this regime, the balance of forces between the continuous and dispersed phase prevent the interface to retract fully back into the capillary. There is, however, a slight retraction due to surface tension forces which moves the jet tip slightly upstream.

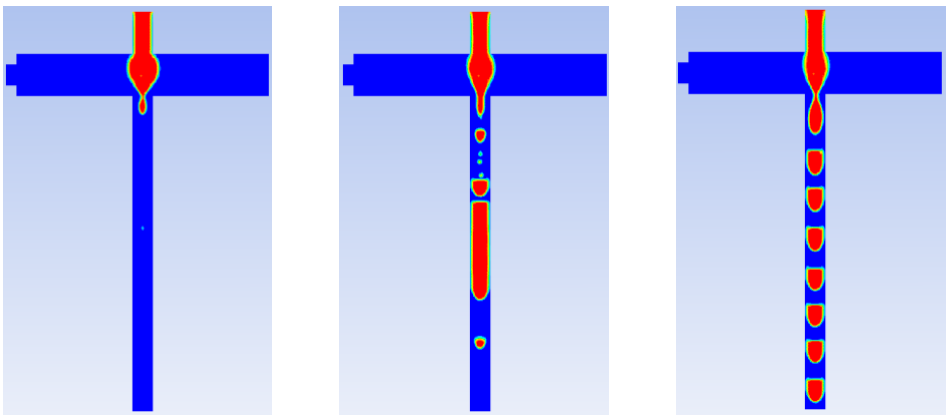

Figure 5.17 – Jet flow behaviour of the CETJ (μ_{cont} = 10.8 mPa.s, U_{cont} = 0.5 ms^{-1}, Q_r = 1.0). a) The bulb is deformed upon reaching the outlet and a new bulb grows from its tip. b) Initially the slugs tend to be poly-dispersed. c) Eventually a balance of forces is reached and monodisperse bubbles radii of 40.0 µm are produced. The rate of bubble production at this stage is approximately 590 thousand bubbles per minute.

The results from this case, as presented in Figure 5.17b & c, show that after producing a few bubbles, slugs of same length tend to appear. The initial polydispersity can be attributed to an "unstable jet". This occurs whilst the competing forces from gas pressure, surface tension and flow shear stress are balancing in the mixing chamber. Jet instability is also observed during experimental studies where it is common practice to stabilise the production process by allowing the device to run for a short time [236] before collecting bubbles. In addition to the mechanisms mentioned, further factors such as vibration of the device and small variations in flow rate or pressure may contribute to experimentally observed instability. The model used in simulations is free from such environmental factors. It is therefore possible for jet stabilisation to occur sooner in simulations and then remain in that stable state.

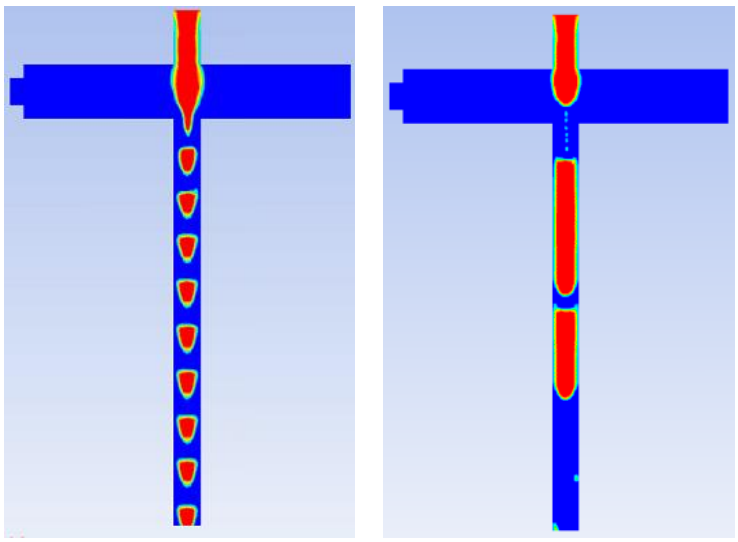

(a) (b)

Figure 5.18 – a) Jet flow for μ_{cont} = 6.0 mPa.s and *Ca*>0.95 resulting in small monodisperse bubbles of radii 30.0 µm. b) Transitional flow for μ_{cont} = 10.8 mPa.s and *Ca*<0.95, leading to polydisperse bubbles.

Having observed the transition to jet flow similar to that demonstrated in co-flowing devices it became interesting to investigate the threshold at which transition occurs. The jet flow formation, as discussed for Figure 5.17, was attributed to higher shear stress resulting from the larger viscosity of the continuous phase in comparison to that of the transitional phase, displayed in Figure 5.16. Increasing the flow rate, and thereby the shear stress in case of μ_{cont} = 6.0 mPa.s and Q_r = 1.0 should, therefore, result in jetting flow. The continuous phase velocity was gradually increased in a

series of simulations until jetting regime was observed at U_l = 0.95 ms^{-1} corresponding to the capillary number of Ca = 0.1 (Figure 5.18a). Conversely, lowering the continuous phase velocity for the μ_{cont} = 10.8 mPa.s and Q_r = 1.0 case resulted in transitional phase like behaviour (Figure 5.18b).

In addition, the onset of jetting was observed to be insensitive to the flow rate ratio. In their experiments, Parhizkar et al. [216], for a given continuous phase flow rate, observed a reduction in bubble size with decreasing gas pressure. The information given in that study is, however, not enough to estimate gas flow rate at inlet boundary from its pressure. The transition was therefore investigated qualitatively as demonstrated in Figure 5.19 by considering two flow ratios of 1.0 and 1.5 for μ_l = 10.8 mPa.s and Ca_{cont} = 0.95. The results as demonstrated in Figure 5.19 show a proportional increase in slug length successfully replicate the empirical observations.

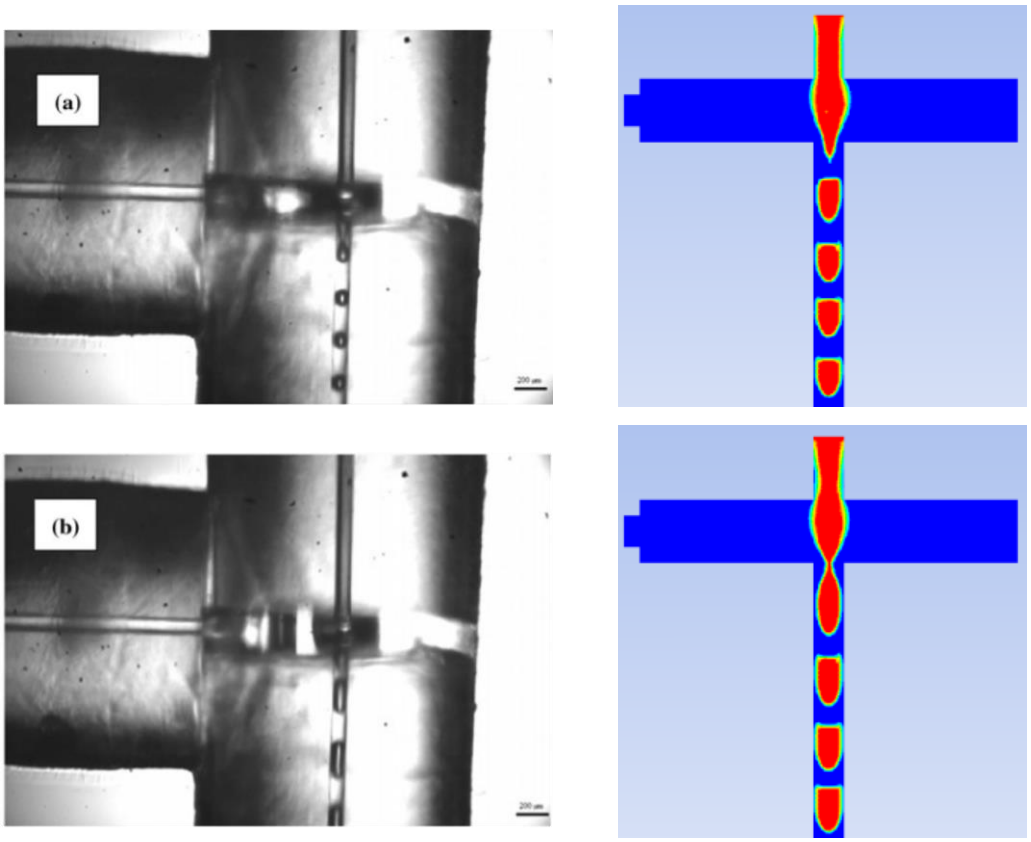

Figure 5.19 – Influence of reduction in disperse phase flow rate upon slug size in jetting regime and quantitative comparison with experimental results in [216] for continuous phase viscosity of 10.8 mPa.s. a) Experimental gas pressure 150.0 kPa and simulation gas/liquid flow rate ratio of 1.0 and slug lengths of 100.0 µm. b) Experimental gas pressure 170.0 kPa and simulation gas/liquid flow rate ratio of 1.5 and slug lengths of 150 µm,

5.7. Discussion and Recommendations

The ability to produce monodisperse populations of microbubbles with diameters smaller than 8.0 μm has been highlighted as an important stepping stone towards engineering of microbubbles for research and clinical use. Having studied the significance of several operating parameters upon the production of microbubbles, this chapter concludes with a number of observations regarding the feasibility of such devices for the aforementioned applications.

The parametric study of the T-Junction has shown that bubble sizes can be decreased by increasing the viscosity of the continuous phase. Figure 5.10 shows a decreasing trend in slug length as *Ca* increases, suggesting that much smaller bubble sizes can be achieved by further increase in viscosity or the flow rate of the continuous phase. While this may seem an attractive course of action, pushing highly viscous liquids at high flow rates through microfluidic channels is a difficult task in practice, resulting in large hydrodynamic pressures. Such high pressures may result in leakage in the pumping syringe as well as tubing interconnections. For example in the experiments of Christopher *et al.* [237] the value of *Ca* was limited to 0.1 to avoid leakages.

Utilising cross flow devices to produce microbubbles for clinical applications can be quickly ruled out based on production rates. Bubble formation rates in all simulations performed approximately ranged from 1-10 per millisecond. This may seem impressive at first, but is insignificant when compared to a commercially available contrast agent such as SonoVue® which has a concentration of $2\text{-}5\times10^{8}$ bubbles/ml [238] that can be prepared in under 1 minute. Low rates of production are however less of an obstacle in a research context where longer timescales can generally be tolerated and investigations of single bubble responses forms a large portion of the research field.

It has been shown here that change in the width of the inlet channel of a T-Junction considerably influences the size of slug length produced. As Figure 5.8 demonstrates, the shortest slug lengths were found to be the same order as the outlet conduit for $\Lambda>0.5$. This may possibly be the most effective method of microbubble size control, particularly when combined with the effect of channel height on the overall volume of the bubble produced. Perhaps the most important conclusion from these studies is that, in contrast to geometry variations, controlling the size of a

microbubble in a T-Junction solely through fluid properties or operating conditions has limited scope. The operating conditions required for such large size reductions would results in extreme practical difficulties.

The embedded capillary T-Junction (CETJ) has been presented as a new, low cost method for microbubble fabrication. Previous observations of the differences in bubble formation in this device and conventional T-Junctions have been confirmed in the simulations and existence of two regimes of "dripping" and "jetting" have been established.

Initial studies into the effect of flow ratio in the dripping regime have demonstrated its direct influence on the bubble size. It is worth noting, however, that the bubbles achieved in the dripping regime, as shown in Figure 5.13, are many times larger than those required for UCA applications. Another important observation here is the role of the outlet channel dimension. In all simulations, a sample of which is illustrated in Figure 5.14, it was observed that the pinch off process was initiated only after the disperse phase filled the outlet conduit. A narrower outlet channel will require a lower volume of the disperse phase in order for it to be filled and thereby the pinch off process starts earlier, and leading to smaller bubbles can be produced. This assertion has been demonstrated in the experimental studies of Parhizkar *et al.* [216]. The height of the mixing chamber was studied in 5.6.4. as another important geometrical factor influencing the bubble size. The resulting bubble diameter, as demonstrated in Figure 5.15, is shown to be reduced by 30% for 50% reduction in chamber height. It should, however, be noted that this device is not immune to difficulties arising from highly viscous flows and there is an operating limit above which failure occurs. Its construction also makes the geometry of the mixing chamber an important operating parameter and one for which there is no provision for accurate control.

Formation of bubbles in this device is in many ways very similar to that in a co-axial flow device, particularly the existence of the jetting regime and its role in dramatic reduction of microbubble size. During the course of simulations, the onset of "jetting" was found to occur approximately at the capillary number of 0.1 for continuous phase viscosities of 10.8 and 6.0 mPa.s. The bubbles made in this regime tend to be much smaller than those observed in dripping. This is a result of the new

bubbles growing from the tip of the bulb which, due to its shape, provides a thin initial "neck" that can be pinched off quicker. It was interesting to note, however, that geometrical factors can be disregarded completely. Indeed, in all simulations performed in the "jetting" regime, the bubbles growing from the bulb tip grew up to the walls of the outlet channel before being pinched off. Instances of this observation can be found in Figures 5.17, 5.18, and 5.19. This, again, demonstrates the significance of the inner capillary dimension in determining the bubble size. Operating in jetting regime can also maximise the rate of bubble production. For example the findings in 5.6.3 and 5.6.5 demonstrate, for a given U_{cont} and Q_r, the rate of bubble formation to increase from 55×10^3 to 590×10^3 bubbles per minute when transitioning from dripping to jetting. The high production rate in the latter case is primarily the result of faster pinch off combined with the liquid/gas interface not rebounding in the mixing chamber. These rates are, however, still insignificant compared to commercially available UCAs such as SonoVue®.

An important difference between the model setup and experiments is setting the gas inlet boundary type as a velocity inlet. The flow rate of the gas in almost all of the experiments in the literature is controlled indirectly through its pressure. Flow rate and pressure are usually linearly related to each other in single phase flow. However, the study into droplet generation in flow focusing devices by Ward *et al.* [239] has shown higher sensitivity of the bubble size to flow rate variation when flow rate rather than pressure is controlled.

The findings here can directly inform the design process of a suitable device for producing armoured microbubbles. The existence of colloidal particles means that instances of blockage in devices with narrow channels may be more frequent. The modification of viscosity as a result of particle addition presents another limiting factor in using narrow channels. It is therefore essential for the device to be easily maintained and fast to replace. Although the capillary embedded T-Junction has this advantage, the minimum bubble size achieved in experiments is far larger than that required for a UCA. Small changes in its design, however, can make it a potentially viable candidate for UCA fabrication. The formation and control of the jetting regime for example would be much easier if the viscous drag was applied in a more symmetric manner. This could be easily achieved by adding another inlet channel on the other side of the mixing chamber. In addition, the gas capillary could be replaced

by a fine needle or a micropipette tip as the gas inlet conduit. These can be as fine as 5.0 μm in width and are relatively easy to replace. Further design suggestions and indirect methods of controlling bubble size are given in Chapter 6.

5.8. Summary

The microfluidic method of bubble fabrication has been only made possible in the last ten years thanks to advances in micro fabrication methods. The main attraction of these devices over other means of bubble production is their ability to produce highly monodisperse populations. The aim of this chapter was to investigate the feasibility of using such devices to fabricate microbubbles for use in medical diagnostics. The study was conducted theoretically using commercial computational fluid dynamic software, thus circumventing various issues presented by production of multiple devices and experimental uncertainties.

Production of bubbles in a cross flow device (T-Junction) was initially considered. Although liquid-liquid multiphase flow in this device has been subject to a number of studies, the same could not be said about gas-liquid flows. The effect of fluid properties, operating parameters, and geometry of the device were investigated. The outcome conclusively demonstrated that size of the microbubble fabricated in such a device is largely bound by the width of its channels. Using this geometry for production of microbubbles suitable for *in vivo* administration, therefore, requires narrow channels which are expensive to make, difficult to maintain, and prone to failure.

The embedded capillary T-Junction is a novel device proposed to overcome the shortcomings described above. This device is in early stages of testing and its physics was not previously theoretically investigated. Computer simulations were carried out to investigate its behaviour. Two main regimes of bubble breakoff were observed with change in relative viscosity: Dripping and Jetting. These were akin to regimes observed in co-axial flow devices. The size of the microbubble was demonstrated to reduce considerably in the jetting region. It was noted, however, the physical design of this junction does not allow the degree of control necessary for fine adjustments and further work in this area needed.

6. Conclusions

6.1. Overview

The overall aims of this thesis were to theoretically explain the empirically observed improved characteristics of nanoparticle coated microbubble contrast agents and investigate the feasibility of microfluidic method of microbubble fabrication. This chapter assesses the progress made with respect the stated objectives as laid out at the beginning of this thesis. This is then followed by a section identifying future avenues of research arising from the findings in this work.

6.2. Contributions

A review of applications of ultrasonic microbubbles was given in Chapter 2. With advances in harmonic imaging of ultrasound contrast agents, there is a drive to engineer UCAs which exhibit highly nonlinear oscillations. One proposed method of achieving this is by embedding nanoparticles into the UCA coating. Initial experimental observations had confirmed that this indeed increased the harmonic response of a bubble. UCAs with such a coating structure had not been subjected to detailed theoretical investigations. The aim of Chapter 3 was model their dynamic behaviour. The influence of nanoparticles was modelled as a modification in coating stiffness and its viscosity and the effect upon microbubble oscillations examined. The results demonstrated a complicated relationship between particle concentration, inherent coating properties, and ultrasound exposure conditions. The addition of nanoparticles was found to shift the frequency response curve. The shift was found to be larger for coatings that were more resistant to compression. This was attributed to an increase in effective stiffness. In addition, the inclusion of nanoparticles greatly dampened bubble oscillations. Next the relationship between particle concentration and asymmetric behaviour was investigated. It was demonstrated that asymmetry is strongest when the bubble is compressed beyond a limiting radius at which the particles reach their packing density. It was also found that, under certain conditions, the inherent shell parameters may mask the effect of nanoparticles. The influence of nanoparticles upon the harmonic and sub-harmonic content in bubble signal was investigated in 3.4.5. It was argued the sub-harmonic content is the result of bubbles

oscillating at their resonance frequency after being subject to insonation at a higher frequency. Because of the shift in the frequency response curve, nanoparticle coated contrast agents are likely to be more responsive than their surfactant-only counterparts at a higher frequency. This in turn makes longer, higher amplitude oscillations at resonance frequency more likely for an armoured bubble post insonation.

Resistance mechanisms to mass transfer from a nanoparticle coated microbubble to its surrounding were investigated Chapter 4. A significant enhancement in stability had been previously observed empirically in bubbles with a nanoparticle coating. These undergo size reduction for a short time after production and rapidly achieve a stable radius. A dissolution equation developed by Epstein and Plesset [240] was re-derived to include nanoparticles to investigate this process. Four stabilising mechanisms were identified and heuristic models were developed to account for them. These were: Reduction of surface tension as a result of increase in surfactant surface concentration; Increase in resistance to mass transfer as a result of the additional surfactant layer; Decrease in surface area available for gas molecules to escape through due to presence of solid nanoparticles in the shell; The collapse of the interface between the particles after packing density is reached.

The new model was then compared to the experimental results by following the same protocol. The additional parameters in the dissolution model were initially limited to physically appropriate ranges and then fitted to the experimental results for nanoparticle coated bubbles using the least squares method. The control experiments were then simulated only by setting the surface concentration of nanoparticles to zero. The results agreed closely with those of the experiments, thereby validating the principles behind the theoretical treatment. The results in 4.6.3 showed that reduction of surface tension and diffusivity with the increase of surfactant concentration acted to retard the dissolution process in unarmoured microbubbles. The dissolution trend, displayed in **Figure** 4.8, however suggests that the process may continue, albeit at a much reduced rate, until the unarmoured microbubbles dissolve completely. This is due to the Laplace pressure continually acting to squeeze the gas out of the bubble, even when the surrounding liquid is saturated. The addition of nanoparticles to the coating results in the elimination of Laplace pressure due to modification in local curvature as proposed and modelled in 4.4.2. Given the significant role of Laplace

pressure in driving dissolution, it can be argued that its elimination is the most important mechanism contributing to the stability of armoured microbubbles.

In order to engineer the behaviour of a microbubble to suit a particular application, one must first have the ability to fabricate microbubbles with near identical properties to allow for controlled experimental results. Having shown promising results, fabrication of microbubbles using multiphase flow in microfluidic devices was considered with the particular aim of assessing their feasibility to produce microbubbles in sizes suitable for medical diagnostics. The physics of microfluidic multiphase flows as well as a number of microfluidic devices commonly used in bubble/droplet generation were briefly reviewed. The focus was then turned to study the physical parameters influencing the bubble size in a T-Junction. This was achieved by simulating the multiphase flows using a commercially available CFD package.

The models and settings used in simulations were first validated, by comparing numerical results against published experimental studies of gas/liquid flows in T-Junction. Changing the geometry of the channel by reduction of inlet-outlet width ratios, Λ, to below 0.5 resulted in a clear transition from slug to bubbly flow. The effect of changing the viscosity of the continuous phase and the flow rate ratio was then considered by conducting simulations for a range of values for the case of Λ = 1.0. The length of the resulting slugs decreased linearly with the reduction of gas-liquid flow ratio. Higher Capillary numbers (*Ca*) achieved by increasing the viscosity of the continuous phase also resulted in a reduction of slug lengths It was concluded that although clearly influenced by physical properties and the flow rate of the continuous phase, the size of bubbles in a T-Junction is dependant chiefly on the geometry of the device. Reduction in channel size increases the chances of blockages due to fluid impurities. In addition, relatively higher hydrodynamic pressures are needed to achieve the same flow rates compared to that required in larger channels. The findings were important in assessing the design limitations of T-Junction devices for surfactant or nanoparticle coated microbubbles suitable for intravenous injection.

The characteristics of a novel microfluidic device for microbubble fabrication utilising tube capillaries called Capillary Embedded T-Junction (CETJ) instead of

lithographic techniques was the subject of another study in this chapter. The device was subjected to a number of sensitivity studies, covering both geometric and operational parameters. Although the parameter space was much larger than that studied, the results in 5.6 capture a wide range of behaviour and provide an initial window into the workings of the CETJ. An important contribution here was to confirm the existence of two regimes of dripping and jetting. Similar to co-axial flow devices, the transition from dripping to jetting regime was shown in 5.6.5 to be highly influenced by the flow strength of the continuous phase and happened approximately at capillary number of 0.1. Additionally, it was argued in 5.7 that channel dimensions play a significant role in determining bubble sizes regardless of the flow regime. It was concluded that the potential of this device to produce bubbles of the size appropriate for UCA use can be fully realised without the precise control of operational and geometrical parameters; the latter necessitating a revision in the design of CETJ.

6.3. Future Work

The contributions of this thesis to the field of ultrasonic contrast agents were reviewed in the previous section. The use of nanoparticle coating in ultrasonic contrast agent is a novel development in the field with no theoretical study previously conducted. The subjects considered in this thesis were therefore wide ranging in their scope and there is much room for improvement and further interesting areas of research.

The most important area in need of further work in fact relates to experimental studies of microbubble response. For example, most of the models for microbubble dynamics and/or dissolution can be used to simulate very similar behaviour by manipulation of model parameters making it difficult to assess their validity. A very useful contribution to improve contrast agent modelling would there for be devise experimental means of independently quantifying the various parameters used in the models here. For example, the effective coefficient of diffusivity could be experimentally investigated by time studies of a single bubble suspended in a fluid chamber using optical tweezers or at the tip of a micropipette. The resulting controlled environment would provide a better model for fitting the dissolution model to experimental data.

The excitation amplitudes used in the dynamic simulations were limited as mechanisms operating at large amplitude oscillations were not considered in the dynamic models presented in Chapter 3. Large amplitudes of oscillation will result in the coated bubble contracting to a much smaller size than its equilibrium state. Assuming the surfactant and particle concentrations to be respectively near equilibrium and close to packing density, large compressions would mean that the bubble must either deform into a non-spherical shape or eject some surfactant and/or particle from its surface. Good qualitative agreement has been achieved in modelling of surfactant shedding by defining a shedding rate in relation to maximum concentration and the rate of change in surface area. A similar treatment is possible in the case of nanoparticle ejection. However, this will only be beneficial up to a point. Perhaps the most important next step, therefore, is to investigate the stability of armoured microbubbles against high excitation amplitudes using high speed

photography. This would inform further modelling work as well as enabling better means of testing the modelling approach detailed in Chapter 3.

As previously discussed, the sub-harmonic response is observed because of post insonation "ringing". Sub-harmonic response can be useful in diagnostics as the resulting scattered signal experiences less attenuation while travelling through tissue. Such free oscillations, however, are likely to be heavily damped in a more viscous liquid such as blood. Another area of further investigation is to test the efficiency of armoured bubbles in environments mimicking *in vivo* conditions. This will allow for better appreciation of their detectability. It will also provide a better indication of the utility of their sub-harmonic response.

The dissolution of a bubble with a finite thickness shell involves two stages of gas transfer from core to shell and shell to the surrounding liquid. The model presented in Chapter 4 does not account for this. This further complicates the model as the differential equations governing the concentration gradient between each phase must be coupled and new parameters relating to gas dissolution in the new phase must be evaluated which further emphasises the case for the need for future experiments as described above.

The importance of viscosity in bubble formation in microfluidic devices was studied in chapter 5. Surface tension, however, was not considered as a parameter in the studies. The presence of surfactants can considerably affect the interfacial tension at the gas-liquid interface in channel. The resulting alteration in Laplace pressure affects the dynamics of the pinching process and thus the bubble volume and its rate of production. This has been demonstrated in liquid-liquid systems by Schneider *et al.* [241] for droplets generated in a T-Junction. Another parameter not investigated here is the angle between the channels of a cross-flowing device. Both of these could be investigated by conducting further CFD simulations.

Having discussed the difficulties in controlling microbubble sizes independent of channel geometry and the associated problems with smaller channels, it is necessary to also look into methods of size manipulation after formation. One possible way of achieving this would be to create an uncoated microbubble and allow it diffuse for a period before passing it through surfactant solution or nanoparticle colloid dispersion. As well as the potential possibility to control the final size of

microbubbles, the initially larger surface area increases the likelihood of adsorption of surfactants and/or nanoparticles, resulting in more uniform microbubbles. Another possible strategy to reduce microbubble volume while maintaining monodispersity is filtration after production. Active and passive filtration methods such as decantation [74,242], or acoustic filtering can be employed to this end.

The geometry of microfluidic devices is constrained significantly due to their method of production. Lithography processes can only be used to create channels of rectangular cross sections. The cost of manufacturing these devices can also be considerable especially with the need to replace the devices after failure. The recent advances in the processes used in 3D printing have meant that models of much finer detail and more complex geometries can be created. There has been recent research into manufacturing micro reactors using 3D printers [243,244]. The cost of such devices and the expertise required for operating them is considerably less than that of the traditional production methods. They also allow for rapid design modifications. These benefits make further investigation into 3D printed devices for microbubble fabrication an attractive option going into the future.

The development of a nanoparticle coated UCA is in its early phases. The findings in this thesis, however, suggest that they could be viable contrast agent subject to better control of their composition and fabrication. Going forward therefore, there is also a need to consider the safety of such contrast agents. For example the presence of nanoparticles in blood can provoke immune-stimulation reactions such as hypersensitivity and inflammation, or immune-suppression effects such as lowering the body's response to infected and cancerous cells. In addition, the prolonged stability of armoured microbubbles means that further investigation into how they are filtered in the body is essential.

List of Publications

- Azmin, M., Harfield, C., Ahmad, Z., Edirisinghe, M., & Stride, E. (2012). "How do microbubbles and ultrasound interact?" Basic physical, dynamic and engineering principles. *Current pharmaceutical design*, *18*(15), 2118-2134
- Azmin, M., Mohamedi, G., Edirisinghe, M., & Stride, E. P. (2012). Dissolution of coated microbubbles: the effect of nanoparticles and surfactant concentration. *Materials Science and Engineering: C*.
- Mohamedi, G., Azmin, M., Pastoriza-Santos, I., Huang, V., Pérez-Juste, J., Liz-Marzán, L. M., & Stride, E. P. (2012). Effects of gold nanoparticles on the stability of microbubbles. *Langmuir*, *28*(39), 13808-13815.
- Azmin, M., Mohamedi, G., Rademeyer, P., Edirisinghe, M., Liz-Marzan, L., & Stride, E. (2013, June). Investigating the acoustic response of gold nanoparticle coated microbubbles. In *Proceedings of Meetings on Acoustics* (Vol. 19, p. 075042).

Reference List

[1] S. Lafitte, N. Alimazighi, P. Reant, M. Dijos, A. Zaroui, A. Mignot, M. Lafitte, X. Pillois, R. Roudaut, and A. DeMaria, Validation of the Smallest Pocket Echoscopic Device's Diagnostic Capabilities in Heart Investigation, Ultrasound in Medicine & Biology, 37 (2011) 798-804.

[2] M. Hamilton and D. Blackstock, Nonlinear Acoustics, Academic Press, 1998.

[3] M. A. Vannan, P. N. Burns, D. Hope-Simpson, M. Averkiou, and J. E. Powers, Pulse Inversion Detection, an improved method for myocardial contrast echocardiography: Experimental studies and preliminary clinical experience, Circulation, 98 (1998) 503.

[4] P. N. Burns, S. R. Wilson, and D. H. Simpson, Pulse Inversion Imaging of Liver Blood Flow: Improved Method for Characterizing Focal Masses with Microbubble Contrast, Investigative Radiology, 35 (2000).

[5] V. Mor-Avi, E. G. Caiani, K. A. Collins, C. E. Korcarz, J. E. Bednarz, and R. M. Lang, Combined Assessment of Myocardial Perfusion and Regional Left Ventricular Function by Analysis of Contrast-Enhanced Power Modulation Images, Circulation, 104 (2001) 352-357.

[6] M. Averkiou, J. Powers, D. Skyba, M. Bruce, and S. Jensen, Ultrasound contrast imaging research, Ultrasound quarterly, 19 (2003) 27-37.

[7] S. B. Barnett, H. D. Rott, G. R. ter Haar, M. C. Ziskin, and K. Maeda, The sensitivity of biological tissue to ultrasound, Ultrasound in Medicine & Biology, 23 (1997) 805-812.

[8] D. Dalecki, Mechanical bioeffects of ultrasound, Annual Review of Biomedical Engineering, 6 (2004) 229-248.

[9] L. A. Crum, Acoustic cavitation series: part five rectified diffusion, Ultrasonics, 22 (1984) 215-223.

[10] P. S. Epstein and M. S. Plesset, On the Stability of Gas Bubbles in Liquid-Gas Solutions, Journal of Chemical Physics, 18 (1950) 1505-1509.

[11] E. Talu, K. Hettiarachchi, S. Zhao, R. L. Powell, A. P. Lee, M. L. Longo, and P. A. Dayton, Tailoring the size distribution of ultrasound contrast agents: possible method for improving sensitivity in molecular imaging, Molecular imaging, 6 (2007) 384.

[12] E. Stride, K. Pancholi, M. J. Edirisinghe, and S. Samarasinghe, Increasing the nonlinear character of microbubble oscillations at low acoustic pressures, Journal of the Royal Society Interface, 5 (2008) 807-811.

[13] G. Mohamedi, M. Azmin, I. Pastoriza-Santos, V. Huang, J. Pérez-Juste, L. M. Liz-Marzan, M. Edirisinghe, and E. Stride, Effects of Gold Nanoparticles on the Stability of Microbubbles, Langmuir, 28 (2012) 13808-13815.

[14] R. Olszewski, J. Timperley, S. Cezary, M. Monaghan, P. Nihoyannopoulis, R. Senior, and H. Becher, The clinical applications of contrast echocardiography, European Journal of Echocardiography, 8 (2007) S13-S23.

[15] N. S. Chahal and R. Senior, Clinical Applications of Left Ventricular Opacification, Jacc-Cardiovascular Imaging, 3 (2010) 188-196.

[16] S. C. Lee, C. L. Carr, B. P. Davidson, D. Ellegala, A. Xie, A. Ammi, T. Belcik, and J. R. Lindner, Temporal Characterization of the Functional Density of the Vasa Vasorum by Contrast-Enhanced Ultrasonography Maximum Intensity Projection Imaging, Jacc-Cardiovascular Imaging, 3 (2010) 1265-1272.

[17] S. Meairs, Contirast-enhanced ultrasound perfusion imaging in acute stroke patients, European Neurology, 59 (2008) 17-26.

[18] S. F. Huang, R. F. Chang, W. K. Moon, Y. H. Lee, D. R. Chen, and J. S. Suri, Analysis of tumor vascularity using three-dimensional power Doppler ultrasound images, IEEE Transactions on Medical Imaging, 27 (2008) 320-330.

[19] E. Horowitz, R. Orvieto, D. Rabinerson, R. Yoeli, and I. Bar-Hava, Hysteroscopy combined with hysterosalpingo contrast sonography (HyCoSy): A new modality for comprehensive evaluation of the female pelvic organs, Gynecological Endocrinology, 22 (2006) 225-229.

[20] K. Darge, R. T. Moeller, A. Trusen, F. Butter, N. Gordjani, and H. Riedmiller, Diagnosis of vesicoureteric reflux with low-dose contrast-enhanced harmonic ultrasound imaging, Pediatric Radiology, 35 (2005) 73-78.

[21] A. Martegani, S. Meairs, C. Nolsøe, F. Piscaglia, P. Ricci, G. Seidel, B. Skjoldbye, L. Solbiati, L. Thorelius, and F. Tranquart, Guidelines and Good Clinical Practice Recommendations for Contrast Enhanced Ultrasound (CEUS) - Update 2008, (2008), Ultraschall in der Medizin, 29 (2008) 28-44.

[22] H. Bleeker, K. Shung, and J. Barnhart, On the Application of Ultrasonic Contrast Agents for Blood Flowmetry and Assessment of Cardiac Perfusion, Journal of Ultrasound in Medicine, 9 (1990) 461-471.

[23] V. Mahue, J. M. Mari, R. J. Eckersley, and M. X. Tang, Comparison of Pulse Subtraction Doppler and Pulse Inversion Doppler, Ieee Transactions on Ultrasonics Ferroelectrics and Frequency Control, 58 (2011) 73-81.

[24] K. Wei, A. R. Jayaweera, S. Firoozan, A. Linka, D. M. Skyba, and S. Kaul, Quantification of myocardial blood flow with ultrasound-induced destruction of microbubbles administered as a constant venous infusion, Circulation, 97 (1998) 473-483.

[25] E. Leen, P. Ceccotti, C. Kalogeropoulou, W. J. Angerson, S. J. Moug, and P. G. Horgan, Prospective multicenter trial evaluating a novel method of characterizing focal liver lesions using contrast-enhanced sonography, American Journal of Roentgenology, 186 (2006) 1551-1559.

[26] E. Leen, P. Ceccotti, S. J. Moug, P. Glen, J. MacQuarrie, W. J. Angerson, T. Albrecht, J. Hohmann, A. Oldenburg, J. P. Ritz, and P. G. Horgan, Potential value of contrast-enhanced intraoperative ultrasonography during partial hepatectomy for metastases - An essential investigation before resection?, Annals of Surgery, 243 (2006) 236-240.

[27] J. R. Lindner, Detection of inflamed plaques with contrast ultrasound, The American Journal of Cardiology, 90 (2002) L32-L35.

[28] Stride, E., Tang, M, and Eckersley, R. J. Physical Phenomena Affecting Quantitative Imaging of Ultrasound Contrast Agents. Applied Acoustics 70(10) (2009) 1352-1362.

[29] Kiessling, F., Huppert, J., and Palmowski, M. Functional and Molecular Ultrasound Imaging: Concepts and Contrast Agents. Current Medicinal Chemistry 16(5) (2009) 627-642.

[30] A. L. Klibanov, Ligand-Carrying Gas-Filled Microbubbles: Ultrasound Contrast Agents for Targeted Molecular Imaging, Bioconjugate Chemistry, 16 (2004) 9-17.

[31] M. Schneider, Molecular imaging and ultrasound-assisted drug delivery, Journal of Endourology, 22 (2008) 795-801.

[32] A. L. Klibanov, Microbubble contrast agents - Targeted ultrasound imaging and ultrasound-assisted drug-delivery applications, Investigative Radiology, 41 (2006) 354-362.

[33] A. V. Alexandrov, Ultrasound Enhanced Thrombolysis for Stroke, Seminars in Cerebrovascular Diseases and Stroke, 5 (2005) 106-110.

[34] S. Datta, C. C. Coussios, L. E. McAdory, J. Tan, T. Porter, De Court, and C. K. Holland, Correlation of cavitation with ultrasound enhancement of thrombolysis, Ultrasound in Medicine and Biology, 32 (2006) 1257-1267.

[35] K. Hanajiri, T. Maruyama, Y. Kaneko, H. Mitsui, S. Watanabe, M. Sata, R. Nagai, T. Kashima, J. Shibahara, M. Omata, and Y. Matsumoto, Microbubble-induced increase in ablation of liver tumors by high-intensity focused ultrasound, Hepatology Research, 36 (2006) 308-314.

[36] C. W. Zhou, F. Q. Li, Y. Qin, C. M. Liu, X. L. Zheng, and Z. B. Wang, Non-thermal ablation of rabbit liver VX2 tumor by pulsed high intensity focused ultrasound with ultrasound contrast agent: Pathological characteristics, World Journal of Gastroenterology, 14 (2008) 6743-6747.

[37] Y. S. Tung, H. L. Liu, C. C. Wu, K. C. Ju, W. S. Chen, and W. L. Lin, Contrast-agent-enhanced ultrasound thermal ablation, Ultrasound in Medicine and Biology, 32 (2006) 1103-1110.

[38] A. van Wamel, K. Kooiman, M. Harteveld, M. Emmer, F. J. Ten Cate, M. Versluis, and N. de Jong, Vibrating microbubbles poking individual cells: Drug transfer into cells via sonoporation, Journal of Controlled Release, 112 (2006) 149-155.

[39] K. Iwanaga, K. Tominaga, K. Yamamoto, M. Habu, H. Maeda, S. Akifusa, T. Tsujisawa, T. Okinaga, J. Fukuda, and T. Nishihara, Local delivery system of cytotoxic agents to tumors by focused sonoporation, Cancer Gene Therapy, 14 (2007) 354-363.

[40] S. Meairs and A. Alonso, Ultrasound, microbubbles and the blood-brain barrier, Progress in Biophysics & Molecular Biology, 93 (2007) 354-362.

[41] J. Wu, J. Pepe, and M. Rincon, Sonoporation, anti-cancer drug and antibody delivery using ultrasound, Ultrasonics, 44 (2006) E21-E25.

[42] Y. Song, T. Hahn, I. P. Thompson, T. J. Mason, G. M. Preston, G. Li, L. Paniwnyk, and W. E. Huang, Ultrasound-mediated DNA transfer for bacteria, Nucleic Acids Research, 35 (2007) e129.

[43] L. J. M. Juffermans, O. Kamp, P. A. Dijkmans, C. A. Visser, and R. J. P. Musters, Low-intensity ultrasound-exposed microbubbles provoke local hyperpolarization of the cell membrane via activation of BKCa channels, Ultrasound in Medicine and Biology, 34 (2008) 502-508.

[44] D. M. Hallow, A. D. Mahajan, T. E. McCutchen, and M. R. Prausnitz, Measurement and correlation of acoustic cavitation with cellular bioeffects, Ultrasound in Medicine and Biology, 32 (2006) 1111-1122.

[45] T. R. Porter and F. Xie, Therapeutic Ultrasound for Gene Delivery, Echocardiography, 18 (2001) 349-353.

[46] K. Ferrara, R. Pollard, and M. Borden, Ultrasound Microbubble Contrast Agents: Fundamentals and Application to Gene and Drug Delivery, Annu. Rev. Biomed. Eng., 9 (2007) 415-447.

[47] L. J. M. Juffermans, A. van Dijk, C. A. M. Jongenelen, B. Drukarch, A. Reijerkerk, H. E. de Vries, O. Kamp, and R. J. P. Musters, Ultrasound and Microbubble-Induced Intra- and Intercellular Bioeffects in Primary Endothelial Cells, Ultrasound in Medicine & Biology, 35 (2009) 1917-1927.

[48] N. Rapoport, Z. G. Gao, and A. Kennedy, Multifunctional nanoparticles for combining ultrasonic tumor imaging and targeted chemotherapy, Journal of the National Cancer Institute, 99 (2007) 1095-1106.

[49] R. Gramiak and P. M. Shah, Echocardiography of the aortic root, Invest Radiol., 3 (1968) 356-366.

[50] F. W. Kremkau, R. Gramiak, E. L. Carstens, P. M. Shah, and D. H. Kramer, Ultrasonic Detection of Cavitation at Catheter Tips, American Journal of Roentgenology Radium Therapy and Nuclear Medicine, 110 (1970) 177-&.

[51] S. B. Feinstein, F. J. Tencate, W. Zwehl, K. Ong, G. Maurer, C. Tei, P. M. Shah, S. Meerbaum, and E. Corday, Two-Dimensional Contrast Echocardiography .1. Invitro Development and Quantitative-Analysis of Echo Contrast Agents, J Am Coll Cardiol, 3 (1984) 14-20.

[52] R. S. Meltzer, O. E. H. Sartorius, C. T. Lancee, P. W. Serruys, P. D. Verdouw, C. E. Essed, and J. Roelandt, Transmission of Ultrasonic Contrast Through the Lungs, Ultrasound in Medicine and Biology, 7 (1981) 377-384.

[53] F. E. Fox and K. F. Herzfeld, Gas Bubbles with Organic Skin as Cavitation Nuclei, The Journal of the Acoustical Society of America, 26 (1954) 984-989.

[54] E. Quaia, Classification and Safety of Microbubble-Based Contrast Agents, in: E. Quaia (Ed.), Contrast Media in Ultrasonography, Springer Berlin Heidelberg, 2005, pp. 3-14.

[55] F. E. Fox and K. F. Herzfeld, Gas Bubbles with Organic Skin As Cavitation Nuclei, Journal of the Acoustical Society of America, 26 (1954) 984-989.

[56] Becher, H and Burns, P. Handbook of Contrast Echocardiography. 2000. New York and Frankfurt, Springer Verlag.

[57] C. Christiansen, H. Kryvi, P. Sontum, and T. Skotland, Physical and biochemical characterization of Albunex, a new ultrasound contrast agent consisting of air-filled albumin microspheres suspended in a solution of human albumin, Biotechnology and Applied Biochemistry, 19 (1994) 307-320.

[58] A. Killam and H. Dittrich, Cardiac applications of Albunex and FS069, in: B. Goldberg (Ed.), Ultrasound contrast agents, Dunitz, 1997, pp. 43-55.

[59] J. L. Cohen, J. Cheirif, D. S. Segar, L. D. Gillam, J. S. Gottdiener, E. Hausnerova, and D. E. Bruns, Improved left ventricular endocardial border delineation and opacification with OPTISON (FS069), a new echocardiographic contrast agent : Results of a phase III multicenter trial, J Am Coll Cardiol, 32 (1998) 746-752.

[60] Schlief, R. First steps in ultrasound contrast media. Felix, R. Contrast Media From The Past to the Future , 179. 1987.

[61] A. R. Williams, G. Kubowicz, E. Cramer, and R. Schlief, The Effects of the Microbubble Suspension SH U 454 (Echovist®) on Ultrasound-Induced Cell Lysis In a Rotating Tube Exposure System, Echocardiography, 8 (1991) 423-433.

[62] A. Mouaaouy, H. D. Becker, R. Schlief, C. Kuhlo, and C. Portas, Rat liver model for testing intraoperative echo contrast sonography, Surgical Endoscopy, 4 (1990) 114-117.

[63] M. D. Smith, O. L. Kwan, H. J. Reiser, and A. N. DeMaria, Superior intensity and reproducibility of SHU-454, a new right heart contrast agent, J Am Coll Cardiol, 3 (1984) 992-998.

[64] M. J. K. Blomley, T. Albrecht, D. O. Cosgrove, N. Patel, V. Jayaram, J. Butler-Barnes, R. J. Eckersley, A. Bauer, and R. Schlief, Improved Imaging of Liver Metastases with Stimulated Acoustic Emission in the Late Phase of Enhancement with the US Contrast Agent SH U 508A: Early Experience, Radiology, 210 (1999) 409-416.

[65] E. Quaia, F. Calliada, M. Bertolotto, S. Rossi, L. Garioni, L. Rosa, and R. Pozzi-Mucelli, Characterization of Focal Liver Lesions with Contrast-specific US Modes and a Sulfur Hexafluoride-filled Microbubble Contrast Agent: Diagnostic Performance and Confidence1, Radiology, 232 (2004) 420-430.

[66] T. K. Kim, J. K. Han, A. Y. Kim, and B. I. Choi, Limitations of characterization of hepatic hemangiomas using a sonographic contrast agent (Levovist) and power Doppler ultrasonography, Journal of Ultrasound in Medicine, 18 (1999) 737-743.

[67] J. M. Correas, L. Bridal, A. Lesavre, A. Mejean, M. Claudon, and O. Helenon, Ultrasound contrast agents: properties, principles of action, tolerance, and artifacts, European Radiology, 11 (2001) 1316-1328.

[68] D. R. Morel, I. Schwieger, L. Hohn, J. Terrettaz, J. B. Llull, Y. A. Cornioley, and M. Schneider, Human pharmacokinetics and safety evaluation of SonoVue™, a new contrast agent for ultrasound imaging, Investigative Radiology, 35 (2000) 80-85.

[69] M. Schneider, SonoVue, a new ultrasound contrast agent, European Radiology, 9 (1999) S347-S348.

[70] P. A. Dayton, K. E. Morgan, A. L. Klibanov, G. H. Brandenburger, and K. W. Ferrara, Optical and acoustical observations of the effects of ultrasound on contrast agents, Ieee Transactions on Ultrasonics Ferroelectrics and Frequency Control, 46 (1999) 220-232.

[71] A. L. Klibanov, Microbubble contrast agents - Targeted ultrasound imaging and ultrasound-assisted drug-delivery applications, Investigative Radiology, 41 (2006) 354-362.

[72] G. Maresca, V. Summaria, C. Colagrande, R. Manfredi, and F. Calliada, New prospects for ultrasound contrast agents, Eur J Radiol, 27 (1998) S171-S178.

[73] J. Kasprzak and F. Ten Cate, New ultrasound contrast agents for left ventricular and myocardial opacification, Herz, 23 (1998) 474-482.

[74] L. Hoff, P. C. Sontum, and B. Hoff, Acoustic properties of shell-encapsulated, gas-filled ultrasound contrast agents, Ultrasonics Symposium, 1996. Proceedings., 1996 IEEE, 1996, pp. 1441-1444.

[75] M. R. Bohmer, R. Schroeders, J. A. M. Steenbakkers, S. H. P. M. de Winter, P. A. Duineveld, J. Lub, W. P. M. Nijssen, J. A. Pikkemaat, and H. R. Stapert, Preparation of monodisperse polymer particles and capsules by ink-jet printing, Colloids and Surfaces A-Physicochemical and Engineering Aspects, 289 (2006) 96-104.

[76] H. Maruyama, S. Matsutani, H. Saisho, N. Kamiyama, H. Yuki, and K. Miyata, Grey-scale contrast enhancement in rabbit liver with DMP115 at different acoustic power levels, Ultrasound in Medicine & Biology, 26 (2000) 1429-1438.

[77] H. Maruyama, S. Matsutani, H. Saisho, Y. Mine, H. Yuki, and K. Miyata, Extra-Low Acoustic Power Harmonic Images of the Liver With Perflutren, Journal of Ultrasound in Medicine, 22 (2003) 931-938.

[78] J. R. Lindner, J. Song, F. Xu, A. L. Klibanov, K. Singbartl, K. Ley, and S. Kaul, Noninvasive ultrasound imaging of inflammation using microbubbles targeted to activated leukocytes, Circulation, 102 (2000) 2745-2750.

[79] R. F. Mattrey and T. J. Pelura, Perfluorocarbon-based ultrasound contrast agents, Ultrasound contrast agents, Martin Dunitz Ltd, London, 1997, pp. 83-99.

[80] J. M. Correas, P. N. Burns, X. M. Lai, and X. L. Qi, Infusion versus bolus of an ultrasound contrast agent - In vivo dose-response measurements of BR1, Investigative Radiology, 35 (2000) 72-79.

[81] H. Mulvana, E. Stride, J. V. Hajnal, and R. J. Eckersley, Temperature Dependent Behavior of Ultrasound Contrast Agents, Ultrasound in Medicine and Biology, 36 (2010) 925-934.

[82] M. Zhou, F. Cavalieri, and M. Ashokkumar, Tailoring the properties of ultrasonically synthesised microbubbles, Soft Matter, 7 (2011) 623-630.

[83] K. S. Suslick, Y. Didenko, M. M. Fang, T. Hyeon, K. J. Kolbeck, W. B. McNamara, M. M. Mdleleni, and M. Wong, Acoustic cavitation and its chemical consequences, Philosophical Transactions of the Royal Society of London. Series A: Mathematical, Physical and Engineering Sciences, 357 (1999) 335-353.

[84] E. Stride and M. Edirisinghe, Novel microbubble preparation technologies, Soft Matter, 4 (2008) 2350-2359.

[85] J. M. Correas and S. D. Quay, EchoGen™ emulsion: A new ultrasound contrast agent based on phase shift colloids, Clinical Radiology, 51 (1996) 11-14.

[86] O. D. Kripfgans, J. B. Fowlkes, D. L. Miller, O. P. Eldevik, and P. L. Carson, Acoustic droplet vaporization for therapeutic and diagnostic applications, Ultrasound in Medicine & Biology, 26 (2000) 1177-1189.

[87] M. Fabiilli, J. Lee, O. Kripfgans, P. Carson, and J. Fowlkes, Delivery of Water-Soluble Drugs Using Acoustically Triggered Perfluorocarbon Double Emulsions, Pharmaceutical Research, 27 (2010) 2753-2765.

[88] Apfel, R. E., Activatable infusable dispersions containing drops of a superheated liquid for methods of therapy and diagnosis. APFEL ENTERPRISES, INC. [US Patent No.5840276].

[89] K. Bjerknes, Air-filled polymeric microcapsules from emulsions containing different organic phases, Journal of Microencapsulation, 18 (2001) 159-171.

[90] M. Kukizaki and M. Goto, Spontaneous formation behavior of uniform-sized microbubbles from Shirasu porous glass (SPG) membranes in the absence of water-phase flow, Colloids and Surfaces A-Physicochemical and Engineering Aspects, 296 (2007) 174-181.

[91] J. A. Feshitan, C. C. Chen, J. J. Kwan, and M. A. Borden, Microbubble size isolation by differential centrifugation, Journal of Colloid and Interface Science, 329 (2009) 316-324.

[92] U. Farook, E. Stride, M. J. Edirisinghe, and R. Moaleji, Microbubbling by co-axial electrohydrodynamic atomization, Medical & Biological Engineering & Computing, 45 (2007) 781-789.

[93] U. Farook, E. Stride, and M. J. Edirisinghe, Preparation of suspensions of phospholipid-coated microbubbles by coaxial electrohydrodynamic atomization, Journal of the Royal Society Interface, 6 (2009) 271-277.

[94] M. W. Chang, E. Stride, and M. Edirisinghe, A novel process for drug encapsulation using a liquid to vapour phase change material, Soft Matter, 5 (2009) 5029-5036.

[95] E. Stride and M. Edirisinghe, Novel microbubble preparation technologies, Soft Matter, 4 (2008) 2350-2359.

[96] E. Talu, K. Hettiarachchi, H. Nguyen, A. P. Lee, R. L. Powell, M. L. Longo, and P. A. Dayton, Lipid-stabilized Monodisperse Microbubbles Produced by Flow Focusing for Use as Ultrasound Contrast Agents, 2006 Ieee Ultrasonics Symposium, Vols 1-5, Proceedings, (2006) 1568-1571.

[97] K. Pancholi, E. Stride, and M. Edirisinghe, Dynamics of bubble formation in highly viscous liquids, Langmuir, 24 (2008) 4388-4393.

[98] E. C. Unger, T. O. Matsunaga, T. McCreery, P. Schumann, R. Sweitzer, and R. Quigley, Therapeutic applications of microbubbles, Eur J Radiol, 42 (2002) 160-168.

[99] S. D. Tiukinhoy, A. A. Khan, S. L. Huang, M. E. Klegerman, R. C. MacDonald, and D. D. McPherson, Novel echogenic drug-immunoliposomes for drug delivery, Investigative Radiology, 39 (2004) 104-110.

[100] J. P. Christiansen, B. A. French, A. L. Klibanov, S. Kaul, and J. R. Lindner, Targeted tissue transfection with ultrasound destruction of plasmid-bearing cationic microbubbles, Ultrasound in Medicine and Biology, 29 (2003) 1759-1767.

[101] K. Ferrara, R. Pollard, and M. Borden, Ultrasound microbubble contrast agents: Fundamentals and application to gene and drug delivery, Annu. Rev. Biomed. Eng., 9 (2007) 415-447.

[102] A. F. H. Lum, M. A. Borden, P. A. Dayton, L. Peng, D. E. Kruse, S. I. Simon, K. S. Lam, and K. W. Ferrara, Ultrasound Radiation Force Enables Targeted Deposition of Molecularly Targeted Nanoparticles Loaded on Microbubbles Under Flow Conditions, 2006.

[103] A. H. Myrset, H. B. Fjerdingstad, R. Bendiksen, B. E. Arbo, R. M. Bjerke, J. H. Johansen, M. A. Kulseth, and R. Skurtveit, Design and Characterization of Targeted Ultrasound Microbubbles for Diagnostic Use, Ultrasound in Medicine and Biology, 37 (2011) 136-150.

[104] F. Calliada, R. Campani, O. Bottinelli, A. Bozzini, and M. G. Sommaruga, Ultrasound contrast agents: Basic principles, Eur J Radiol, 27 (1998) S157-S160.

[105] M. Postema and G. Schmitz, Ultrasonic bubbles in medicine: Influence of the shell, Ultrasonics Sonochemistry, 14 (2007) 438-444.

[106] Y. A. Çengel and M. A. Boles, Thermodynamics: An Engineering Approach, McGraw-Hill, 2002.

[107] W. Besant, A Treatise on Hydrostatics and Hydrodynamics, Deighton, Bell, and Co., Cambridge 1859.

[108] Rayleigh, Lord. On the pressure developed in a liquid during the collapse of a spherical cavity. Phil.Mag. 34, 94-98. 1917.

[109] M. S. Plesset, The Dynamics of Cavitation Bubbles, Journal of Applied Mechanics-Transactions of the Asme, 16 (1949) 277-282.

[110] Blake, F. G. Technical Memo No.12. 1949. Acoustic Research Laboratory, Harvard University.

[111] B. E. Noltingk and E. A. Neppiras, Cavitation Produced by Ultrasonics, Proceedings of the Physical Society of London Section B, 63 (1950) 674-685.

[112] H. Poritsky, The Collapse or Growth of a Spherical Bubble or Cavity in a Viscous Fluid, ASME, 1951, pp. 813-821.

[113] W. Lauterborn, Numerical Investigation of Nonlinear Oscillations of Gas-Bubbles in Liquids, Journal of the Acoustical Society of America, 59 (1976) 283-293.

[114] S. Popinet and S. Zaleski, Bubble collapse near a solid boundary: a numerical study of the influence of viscosity, Journal of Fluid Mechanics, 464 (2002) 137-163.

[115] Herring, C. Theory of the pulsations of the gas bubble produced by an underwater explosion. C4 sr20. 1941. NDCR Division 6.

[116] L. Trilling, The Collapse and Rebound of a Gas Bubble, Journal of Applied Physics, 23 (1952) 14-17.

[117] Gilmore, FR. Growth or collapse of a bubble in a compressible and viscous liquid. report 26-4. 1952. Hydrodynamics Laboratory, California Institute Technology, Pasadena.

[118] Y. Tomita and A. Shima, On the Behavior of a Spherical Bubble and the Impulse Pressure in a Viscous Compressible Liquid, Bulletin of the JSME, 20 (1977) 1453-1460.

[119] A. Shima and Y. Tomita, The behavior of a spherical bubble near a solid wall in a compressible liquid, Archive of Applied Mechanics, 51 (1981) 243-255.

[120] J. B. Keller and M. Miksis, Bubble oscillations of large amplitude, The Journal of the Acoustical Society of America, 68 (1980) 628-633.

[121] R. H. Cole, Underwater Explosions, Princeton University Press, 1948.

[122] Kirkwood, J. G. and Bethe, H. OSRD Rep. No. 588. 1942.

[123] H. S. Tsien, The Poincaré-Lighthill-Kuo Method, in: H. L. Dryden (Ed.), Advances in Applied Mechanics, Elsevier, 1956, pp. 281-349.

[124] W. Lauterborn and H. Bolle, Experimental Investigations of Cavitation-Bubble Collapse in Neighborhood of A Solid Boundary, Journal of Fluid Mechanics, 72 (1975) 391.

[125] K. Vokurka, Comparison of Rayleigh's, Herring's, and Gilmore's models of gas bubbles, Acustica, 59 (1986) 214-219.

[126] A. Prosperetti and A. Lezzi, Bubble Dynamics in A Compressible Liquid .1. 1St-Order Theory, Journal of Fluid Mechanics, 168 (1986) 457-478.

[127] D. Fuster, Liquid compressibility effects during the collapse of a single cavitating bubble, J. Acoust. Soc. Am., 129 (2011) 122.

[128] H. G. Flynn, Cavitation Dynamics .1. Mathematical Formulation, Journal of the Acoustical Society of America, 57 (1975) 1379-1396.

[129] G. J. Lastman and R. A. Wentzell, Cavitation of A Bubble in An Inviscid Compressible Liquid, with Comparisons to A Viscous Incompressible Liquid, Physics of Fluids, 22 (1979) 2259-2266.

[130] Moshaii, A, Sadighi, R, and Taeibi, M. A New Damping Mechanism in Non-linear Bubble Dynamics. http://arxiv.org/abs/physics/0309080v1 . 17-9-2003. (Last Accessed 15-9-2011).

[131] A. Prosperetti, L. A. Crum, and K. W. Commander, Nonlinear Bubble Dynamics, Journal of the Acoustical Society of America, 83 (1988) 502-514.

[132] N. de Jong, L. Hoff, T. Skotland, and N. Bom, Absorption and scatter of encapsulated gas filled microspheres: theoretical considerations and some measurements, Ultrasonics, 30 (1992) 95-103.

[133] N. de Jong and L. Hoff, Ultrasound scattering properties of Albunex microspheres, Ultrasonics, 31 (1993) 175-181.

[134] H. Medwin, Counting bubbles acoustically: a review, Ultrasonics, 15 (1977) 7-13.

[135] C. C. Church, The Effects of An Elastic Solid-Surface Layer on the Radial Pulsations of Gas-Bubbles, Journal of the Acoustical Society of America, 97 (1995) 1510-1521.

[136] A. Prosperetti, Thermal Effects and Damping Mechanisms in Forced Radial Oscillations of Gas-Bubbles in Liquids, Journal of the Acoustical Society of America, 61 (1977) 17-27.

[137] L. Hoff, P. C. Sontum, and J. M. Hovem, Oscillations of polymeric microbubbles: Effect of the encapsulating shell, Journal of the Acoustical Society of America, 107 (2000) 2272-2280.

[138] L. Hoff, P. C. Sontum, and J. M. Hovem, Oscillations of polymeric microbubbles: Effect of the encapsulating shell, Journal of the Acoustical Society of America, 107 (2000) 2272-2280.

[139] F. E. Fox and K. F. Herzfeld, Gas Bubbles with Organic Skin As Cavitation Nuclei, Journal of the Acoustical Society of America, 26 (1954) 984-989.

[140] R. E. Glazman, Damping of bubble oscillations induced by transport of surfactants between the adsorbed film and the bulk solution, The Journal of the Acoustical Society of America, 76 (1984) 890-896.

[141] R. E. Glazman, Effects of Adsorbed Films on Gas Bubble Radial Oscillations, Journal of the Acoustical Society of America, 74 (1983) 980-986.

[142] K. E. Morgan, J. S. Allen, P. A. Dayton, J. E. Chomas, A. L. Klibaov, and K. W. Ferrara, Experimental and theoretical evaluation of microbubble behavior: effect of transmitted phase and bubble size, Ultrasonics, Ferroelectrics and Frequency Control, IEEE Transactions on, 47 (2000) 1494-1509.

[143] K. Vokurka, Comparison of Rayleigh's, Herring's, and Gilmore's Models of Gas Bubbles, Acustica, 59 (1986) 214-219.

[144] P. Marmottant, S. van der Meer, M. Emmer, M. Versluis, N. de Jong, S. Hilgenfeldt, and D. Lohse, A model for large amplitude oscillations of coated bubbles accounting for buckling and rupture, Journal of the Acoustical Society of America, 118 (2005) 3499-3505.

[145] S. M. van der Meer, B. Dollet, M. M. Voormolen, C. T. Chin, A. Bouakaz, N. de Jong, M. Versluis, and D. Lohse, Microbubble spectroscopy of ultrasound contrast agents, Journal of the Acoustical Society of America, 121 (2007) 648-656.

[146] N. de Jong, M. Emmer, C. T. Chin, A. Bouakaz, F. Mastik, D. Lohse, and M. Versluis, "Compression-only" behavior of phospholipid-coated contrast bubbles, Ultrasound Med. Biol., 33 (2007) 653-656.

[147] E. Stride, The influence of surface adsorption on microbubble dynamics, Philos. Transact. A Math. Phys. Eng Sci., 366 (2008) 2103-2115.

[148] J. N. Israelachvili, Intermolecular and surface forces, Academic Press, 3rd ed. (2011).

[149] M. Sacchetti, H. Yu, and G. Zografi, In-plane steady shear viscosity of monolayers at the air/water interface and its dependence on free area, Langmuir, 9 (1993) 2168-2171.

[150] J. P. O'Brien, N. Ovenden, and E. Stride, Accounting for the stability of microbubbles to multi-pulse excitation using a lipid-shedding model, The Journal of the Acoustical Society of America, 130 (2011) 180-185.

[151] K. Vokurka, Amplitudes of free bubble oscillations in liquids, Journal of Sound and Vibration, 141 (1990) 259-275.

[152] V. Sboros, C. A. MacDonald, S. D. Pye, C. M. Moran, J. Gomatam, and W. N. McDicken, The dependence of ultrasound contrast agents backscatter on acoustic pressure: theory versus experiment, Ultrasonics, 40 (2002) 579-583.

[153] M. X. Tang and R. J. Eckersley, Frequency and pressure dependent attenuation and scattering by microbubbles, Ultrasound in Medicine & Biology, 33 (2007) 164-168.

[154] W. Lauterborn, Numerical Investigation of Nonlinear Oscillations of Gas-Bubbles in Liquids, Journal of the Acoustical Society of America, 59 (1976) 283-293.

[155] P. N. Burns, J. E. Powers, D. H. Simpson, A. Brezina, A. Kolin, C. T. Chin, V. Uhlendorf, and T. Fritzsch, Harmonic power mode Doppler using microbubble contrast agents: an improved method for small vessel flow imaging, Ultrasonics Symposium, 1994. Proceedings., 1994 IEEE, 1994, pp. 1547-1550.

[156] F. Forsberg, W. T. Shi, and B. B. Goldberg, Subharmonic imaging of contrast agents, Ultrasonics, 38 (2000) 93-98.

[157] T. G. Leighton, F. Fedele, A. J. Coleman, C. McCarthy, S. Ryves, A. M. Hurrell, A. De Stefano, and P. R. White, A Passive Acoustic Device for Real-Time Monitoring of the Efficacy of Shockwave Lithotripsy Treatment, Ultrasound in Medicine and Biology, 34 (2008) 1651-1665.

[158] W. Lauterborn and T. Kurz, Physics of bubble oscillations, Reports on Progress in Physics, 73 (2010).

[159] C. C. Church and E. L. Carstensen, "Stable" inertial cavitation, Ultrasound in Medicine and Biology, 27 (2001) 1435-1437.

[160] H. G. Flynn, Cavitation dynamics: II. Free pulsations and models for cavitation bubbles, The Journal of the Acoustical Society of America, 58 (1975) 1160-1170.

[161] D. W. Readey and A. R. Cooper, Molecular Diffusion with A Moving Boundary and Spherical Symmetry, Chemical Engineering Science, 21 (1966) 917-&.

[162] M. C. Weinberg, Surface-Tension Effects in Gas Bubble Dissolution and Growth, Chemical Engineering Science, 36 (1981) 137-141.

[163] P. B. Duncan and D. Needham, Test of the Epstein-Plesset model for gas microparticle dissolution in aqueous media: Effect of surface tension and gas undersaturation in solution, Langmuir, 20 (2004) 2567-2578.

[164] F. G. Blake, Gas Bubbles As Cavitation Nuclei, Phys. Rev., 75 (1949) 1313.

[165] Crum, L. A. Air Bubble Growth by Rectified Diffusion. 15-4-1980. University of Mississippi.

[166] M. M. Fyrillas and A. J. Szeri, Dissolution Or Growth of Soluble Spherical Oscillating Bubbles, Journal of Fluid Mechanics, 277 (1994) 381-407.

[167] C. C. Church, Prediction of rectified diffusion during nonlinear bubble pulsations at biomedical frequencies, The Journal of the Acoustical Society of America, 83 (1988) 2210-2217.

[168] E. P. Stride and C. C. Coussios, Cavitation and contrast: the use of bubbles in ultrasound imaging and therapy, Proc. Inst. Mech. Eng H, 224 (2010) 171-191.

[169] J. J. Kwan and M. A. Borden, Microbubble Dissolution in a Multigas Environment, Langmuir, 26 (2010) 6542-6548.

[170] P. Marmottant, S. van der Meer, M. Emmer, M. Versluis, N. de Jong, S. Hilgenfeldt, and D. Lohse, A model for large amplitude oscillations of coated bubbles accounting for buckling and rupture, Journal of the Acoustical Society of America, 118 (2005) 3499-3505.

[171] M. A. Borden and M. L. Longo, Dissolution behavior of lipid monolayer-coated, air-filled microbubbles: Effect of lipid hydrophobic chain length, Langmuir, 18 (2002) 9225-9233.

[172] K. Sarkar, A. Katiyar, and P. Jain, Growth and Dissolution of An Encapsulated Contrast Microbubble: Effects of Encapsulation Permeability, Ultrasound in Medicine and Biology, 35 (2009) 1385-1396.

[173] M. M. Fyrillas and A. J. Szeri, Dissolution Or Growth of Soluble Spherical Oscillating Bubbles - the Effect of Surfactants, Journal of Fluid Mechanics, 289 (1995) 295-314.

[174] F. Guidi, H. J. Vos, R. Mori, N. de Jong, and P. Tortoli, Microbubble Characterization Through Acoustically Induced Deflation, Ieee Transactions on Ultrasonics Ferroelectrics and Frequency Control, 57 (2010) 193-202.

[175] M. A. Borden, D. E. Kruse, C. F. Caskey, S. Zhao, P. A. Dayton, and K. W. Ferrara, Influence of lipid shell physicochemical properties on ultrasound-induced microbubble destruction, IEEE Trans Ultrason Ferroelectr Freq Control, 52 (2005) 1992-2002.

[176] J. O'Brien, N. Ovenden, and E. P. Stride, Accounting for the stability of microbubbles to multi-pulse excitation using a lipid-shedding model, J. Acoust. Soc. Am., 130 (2011) EL180.

[177] J. Morris, E. P. Ingenito, L. Mark, R. D. Kamm, and M. Johnson, Dynamic Behavior of Lung Surfactant, Journal of Biomechanical Engineering, 123 (2001) 106-113.

[178] N. de Jong, A. Bouakaz, and F. J. Ten Cate, Contrast harmonic imaging, Ultrasonics, 40 (2002) 567-573.

[179] C. C. Church, Spontaneous homogeneous nucleation, inertial cavitation and the safety of diagnostic ultrasound, Ultrasound in Medicine & Biology, 28 (2002) 1349-1364.

[180] A. Bala Subramaniam, M. Abkarian, L. Mahadevan, and H. A. Stone, Colloid science: Non-spherical bubbles, Nature, 438 (2005) 930.

[181] M. Abkarian, A. B. Subramaniam, S. H. Kim, R. J. Larsen, S. M. Yang, and H. A. Stone, Dissolution arrest and stability of particle-covered bubbles, Phys. Rev. Lett., 99 (2007) 188301.

[182] C. C. Church, The Effects of An Elastic Solid-Surface Layer on the Radial Pulsations of Gas-Bubbles, Journal of the Acoustical Society of America, 97 (1995) 1510-1521.

[183] R. E. Glazman, Effects of Adsorbed Films on Gas Bubble Radial Oscillations, Journal of the Acoustical Society of America, 74 (1983) 980-986.

[184] H. Reismann and P. S. Pawlik, Elasticity, theory and applications, Wiley, New York 1980.

[185] C. Truesdell, W. Noll, and S. Antman, The Non-Linear Field Theories of Mechanics, Springer, 2004.

[186] L. D. Landau and E. M. Lifshitz, Theory of Elasticity, Butterworth-Heinemann, Oxford 1970.

[187] L. D. Landau and E. M. Lifshit-ís, Fluid mechanics, Butterworth-Heinemann, 1987.

[188] A. A. Doinikov and P. A. Dayton, Spatio-temporal dynamics of an encapsulated gas bubble in an ultrasound field, The Journal of the Acoustical Society of America, 120 (2006) 661-669.

[189] L. N. Liebermann, The Second Viscosity of Liquids, Phys. Rev., 75 (1949) 1415-1422.

[190] S. Schürch, H. Bachofen, J. Goerke, and F. Green, Surface properties of rat pulmonary surfactant studied with the captive bubble method: adsorption, hysteresis, stability, Biochimica et Biophysica Acta (BBA) - Biomembranes, 1103 (1992) 127-136.

[191] S. Baoukina, L. Monticelli, H. J. Risselada, S. J. Marrink, and D. P. Tieleman, The molecular mechanism of lipid monolayer collapse, Proceedings of the National Academy of Sciences, 105 (2008) 10803-10808.

[192] A. Einstein, Eine neue Bestimmung der Moleküldimensionen, Ann. Phys., 324 (1906) 289-306.

[193] G. K. Batchelor and J. T. Green, The determination of the bulk stress in a suspension of spherical particles to order c2, Journal of Fluid Mechanics, 56 (1972) 401-427.

[194] D. Bedeaux, R. Kapral, and P. Mazur, The effective shear viscosity of a uniform suspension of spheres, Physica A: Statistical Mechanics and its Applications, 88 (1977) 88-121.

[195] K. F. Freed and M. Muthukumar, Cluster theory for concentration dependence of shear viscosity for suspensions of interacting spheres. I, The Journal of Chemical Physics, 76 (1982) 6186-6194.

[196] C. W. J. Beenakker and P. Mazur, Diffusion of spheres in a concentrated suspension II, Physica A: Statistical Mechanics and its Applications, 126 (1984) 349-370.

[197] E. G. D. Cohen, R. Verberg, and I. M. de Schepper, Newtonian viscosity and visco-elastic behavior of concentrated neutral hard-sphere colloidal suspensions, International Journal of Multiphase Flow, 23 (1997) 797-807.

[198] J. C. van der Werff and C. G. de Kruif, Hard-sphere Colloidal Dispersions: The Scaling of Rheological Properties with Particle Size, Volume Fraction, and Shear Rate, Journal of Rheology, 33 (1989) 421-454.

[199] S. V. Lishchuk and I. Halliday, Effective surface viscosities of a particle-laden fluid interface, Phys. Rev. E, 80 (2009) 016306.

[200] E. Stride, The influence of surface adsorption on microbubble dynamics, Philos. Transact. A Math. Phys. Eng Sci., 366 (2008) 2103-2115.

[201] N. Hosny, G. Mohamedi, P. Rademeyer, J. Owen, Y. Wu, M. X. Tang, R. J. Eckersley, E. Stride, and M. K. Kuimova, Mapping microbubble viscosity using fluorescence lifetime imaging of molecular rotors, Proceedings of the National Academy of Sciences of the United States of America, 110 (2013) 9225-9230.

[202] O'Brien, J., Ovenden, N., and Stride, E. Accounting for the stability of microbubbles to multi-pulse excitation using a lipid-shedding model. Journal of the Acoustical Society of America, 130(4) (2011), EL180-EL185.

[203] H. S. Carslaw, Introduction to the mathematical theory of the conduction of heat in solids, 2d. ed (1921).

[204] P. S. Epstein and M. S. Plesset, On the Stability of Gas Bubbles in Liquid-Gas Solutions, Journal of Chemical Physics, 18 (1950) 1505-1509.

[205] M. C. Weinberg, Surface-Tension Effects in Gas Bubble Dissolution and Growth, Chemical Engineering Science, 36 (1981) 137-141.

[206] J. M. Crane and S. B. Hall, Rapid compression transforms interfacial monolayers of pulmonary surfactant, Biophys J, 80 (2001) 1863-1872.

[207] E. P. Ingenito, L. Mark, J. Morris, F. F. Espinosa, R. D. Kamm, and M. Johnson, Biophysical characterization and modeling of lung surfactant components, Journal of Applied Physiology, 86 (1999) 1702-1714.

[208] D. R. Otis, E. P. Ingenito, R. D. Kamm, and M. Johnson, Dynamic surface tension of surfactant TA: experiments and theory, Journal of Applied Physiology, 77 (1994) 2681-2688.

[209] M. Nedyalkov, R. Krustev, D. Kashchiev, D. Platikanov, and D. Exerowa, Permeability of Newtonian black foam films to gas, Colloid & Polymer Sci, 266 (1988) 291-296.

[210] S. I. Kam and W. R. Rossen, Anomalous capillary pressure, stress, and stability of solids-coated bubbles, Journal of Colloid and Interface Science, 213 (1999) 329-339.

[211] Y. F. Cheng, S. J. Guo, and H. Y. Lai, Dynamic simulation of random packing of spherical particles, Powder Technology, 107 (2000) 123-130.

[212] J. Schmelzer and F. Schweitzer, Ostwald Ripening of Bubbles in Liquid-Gas Solutions, Journal of Non-Equilibrium Thermodynamics, 12 (1987) 255-270.

[213] L. Ratke and P. W. Voorhees, Growth and coarsening: Ostwald ripening in material processing, Springer, 2002.

[214] W. Wang, C. C. Moser, and M. A. Wheatley, Langmuir Trough Study of Surfactant Mixtures Used in the Production of a New Ultrasound Contrast Agent Consisting of Stabilized Microbubbles, The Journal of Physical Chemistry, 100 (1996) 13815-13821.

[215] H. Mulvana, E. Stride, J. V. Hajnal, and R. J. Eckersley, Temperature Dependent Behavior of Ultrasound Contrast Agents, Ultrasound in Medicine & Biology, 36 (2010) 925-934.

[216] M. Parhizkar, M. Edirisinghe, and E. Stride, Effect of operating conditions and liquid physical properties on the size of monodisperse microbubbles produced in a capillary embedded T-junction device, Microfluid Nanofluid, 14 (2013) 797-808.

[217] B. A. Shannak, Frictional pressure drop of gas liquid two-phase flow in pipes, Nuclear Engineering and Design, 238 (2008) 3277-3284.

[218] P. Wu and W. A. Little, Measurement of the heat transfer characteristics of gas flow in fine channel heat exchangers used for microminiature refrigerators, Cryogenics, 24 (1984) 415-420.

[219] X. F. Peng, G. P. Peterson, and B. X. Wang, Frictional flow characteristics of water flowing through rectangular microchannels, Experimental Heat Transfer, 7 (1994) 249-264.

[220] X. F. Peng and G. P. Peterson, The effect of thermofluid and geometrical parameters on convection of liquids through rectangular microchannels, International Journal of Heat and Mass Transfer, 38 (1995) 755-758.

[221] N. T. Obot, Determination of Incompressible Flow Friction in Smooth Circular and Noncircular Passages: A Generalized Approach Including Validation of the Nearly Century Old Hydraulic Diameter Concept, Journal of Fluids Engineering, 110 (1988) 431-440.

[222] C. Cramer, P. Fischer, and E. J. Windhab, Drop formation in a co-flowing ambient fluid, Chemical Engineering Science, 59 (2004) 3045-3058.

[223] G. F. Scheele and B. J. Meister, Drop formation at low velocities in liquid-liquid systems: Part I. Prediction of drop volume, AIChE J., 14 (1968) 9-15.

[224] A. S. Utada, A. Fernandez-Nieves, H. A. Stone, and D. A. Weitz, Dripping to Jetting Transitions in Coflowing Liquid Streams, Phys. Rev. Lett., 99 (2007) 094502.

[225] T. Thorsen, R. W. Roberts, F. H. Arnold, and S. R. Quake, Dynamic pattern formation in a vesicle-generating microfluidic device, Phys. Rev. Lett., 86 (2001) 4163.

[226] A. M. Gañán-Calvo and J. M. Gordillo, Perfectly Monodisperse Microbubbling by Capillary Flow Focusing, Phys. Rev. Lett., 87 (2001) 274501.

[227] S. L. Anna, N. Bontoux, and H. A. Stone, Formation of dispersions using ``flow focusing'' in microchannels, Appl. Phys. Lett., 82 (2003) 364-366.

[228] R. Dreyfus, P. Tabeling, and H. Willaime, Ordered and Disordered Patterns in Two-Phase Flows in Microchannels, Phys. Rev. Lett., 90 (2003) 144505.

[229] P. Garstecki, H. A. Stone, and G. M. Whitesides, Mechanism for Flow-Rate Controlled Breakup in Confined Geometries: A Route to Monodisperse Emulsions, Phys. Rev. Lett., 94 (2005) 164501.

[230] B. Dollet, W. van Hoeve, J. P. Raven, P. Marmottant, and M. Versluis, Role of the Channel Geometry on the Bubble Pinch-Off in Flow-Focusing Devices, Phys. Rev. Lett., 100 (2008) 034504.

[231] C. W. Hirt and B. D. Nichols, Volume of fluid (VOF) method for the dynamics of free boundaries, Journal of Computational Physics, 39 (1981) 201-225.

[232] R. Courant, K. Friedrichs, and H. Lewy, On the partial difference equations of mathematical physics, IBM journal of Research and Development, 11 (1967) 215-234.

[233] R. M. Santos and M. Kawaji, Numerical modeling and experimental investigation of gas/liquid slug formation in a microchannel T-junction, International Journal of Multiphase Flow, 36 (2010) 314-323.

[234] P. Garstecki, M. J. Fuerstman, H. A. Stone, and G. M. Whitesides, Formation of droplets and bubbles in a microfluidic T-junction-scaling and mechanism of break-up, Lab Chip, 6 (2006) 437-446.

[235] K. Pancholi, E. Stride, and M. Edirisinghe, Generation of microbubbles for diagnostic and therapeutic applications using a novel device, Journal of Drug Targeting, 16 (2008) 494-501.

[236] T. D. Dang, Y. H. Kim, H. G. Kim, and G. M. Kim, Preparation of monodisperse PEG hydrogel microparticles using a microfluidic flow-focusing device, Journal of Industrial and Engineering Chemistry, 18 (2012) 1308-1313.

[237] G. F. Christopher, N. N. Noharuddin, J. A. Taylor, and S. L. Anna, Experimental observations of the squeezing-to-dripping transition in T-shaped microfluidic junctions, Phys. Rev. E, 78 (2008) 036317.

[238] J. Tu, J. Guan, Y. Qiu, and T. J. Matula, Estimating the shell parameters of SonoVue® microbubbles using light scattering, The Journal of the Acoustical Society of America, 126 (2009) 2954-2962.

[239] T. Ward, M. Faivre, M. Abkarian, and H. A. Stone, Microfluidic flow focusing: Drop size and scaling in pressure versus flow-rate-driven pumping, Electrophoresis, 26 (2005) 3716-3724.

[240] P. S. Epstein and M. S. Plesset, On the Stability of Gas Bubbles in Liquid-Gas Solutions, Journal of Chemical Physics, 18 (1950) 1505-1509.

[241] T. Schneider, D. R. Burnham, J. VanOrden, and D. T. Chiu, Systematic investigation of droplet generation at T-junctions, Lab Chip, 11 (2011) 2055-2059.

[242] D. E. Goertz, N. de Jong, and A. F. W. van der Steen, Attenuation and Size Distribution Measurements of Definity and Manipulated Definity™ Populations, Ultrasound in Medicine & Biology, 33 (2007) 1376-1388.

[243] P. J. Kitson, M. H. Rosnes, V. Sans, V. Dragone, and L. Cronin, Configurable 3D-Printed millifluidic and microfluidic 'lab on a chip' reactionware devices, Lab Chip, 12 (2012) 3267-3271.

[244] K. B. Anderson, S. Y. Lockwood, R. S. Martin, and D. M. Spence, A 3D Printed Fluidic Device that Enables Integrated Features, Anal. Chem., 85 (2013) 5622-5626.

Appendix

A. Acoustic Response Experiments

Bubble Preperation

The basic bubble formulation is as follows. A lipid film of 0.13 vol% DSPC and 0.025vol% Na+ salt, prepared via solvent evaporation, was added to an aqueous solution containing 0.05 vol% PEG40S, purchased from Sigma-Aldrich Co. Nitrogen was used as the gas in all cases. Bubbles were also prepared using a Capillary T-junction device consisting of three polyether ether ketone (PEEK) capillaries with an internal diameter of 75 μm embedded in a rigid acrylic Perspex block. The capillaries were held in place using standard high-pressure liquid chromatography (HPLC) connectors and ferrules. All tubing and ferrules were purchased from Gilson Scientific Ltd., Luton, UK. The upper capillary was connected to a nitrogen cylinder, which supplied the gas at a constant pressure of 43.5 MPa, as measured by a digital manometer. The middle capillary was connected to a digital Aladdin syringe pump, which allowed for measurable non-pulsatile constant fluid flow. The third capillary was used to collect the microbubbles after formation. The three capillaries were separated in the centre of the device by a distance of approximately 70 μm.

Acoustic response

The non-linear behaviour of the microbubbles was tested using a specially designed rig immersed in DI water at ambient temperature (Figure A.0.1). Microbubbles were hydrodynamically isolated and streamed using a pair of co-axially aligned needles into the focal region of a pair of transducers. The microbubbles were interrogated by exciting the transmitting transducer (3.5 MHz focussed, Panametrics-NDT) with a 2MHz Gaussian-windowed 5 cycle pulse train generated by an arbitrary function generator (33220A, Agilent). The signal was then amplified (50dB) by an RF power amplifier (325LA, Electric and Innovation) at a pulse repetition rate of 100 Hz. The input voltage was varied to produce peak negative pressures ranging from 50 to 600 kPa. The scattered pressure was detected at 90 degrees using a 3.5 MHz focussed transducer (V382, Panametrics-NDT) where the signal was

amplified (35dB) using a pulser/receiver (DPR300, JSR Ultrasonics) and digitised with an oscilloscope (600 MHz, Xi64-A, Waverunner, LeCroy). The data were saved to disk and the captured signals were processed in MATLAB using purpose-written code whereby each signal is analysed in the frequency domain, obtained via Fast Fourier Transform (MATLAB function, 'fft.m').

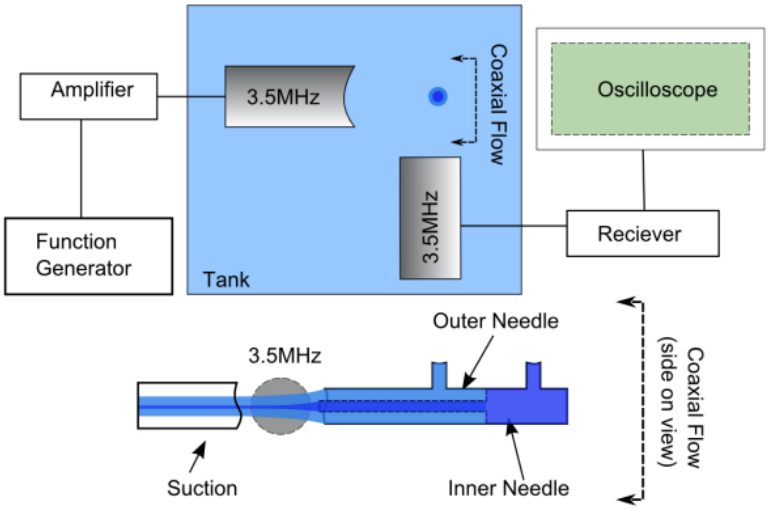

Figure A.0.1 Schematic representation of Acoustic testing set-up